Optimizing Nonlinear Dynamics in Energy System Planning and Control

Wai Keung Terrence Mak

A thesis submitted for the degree of
Doctor of Philosophy of
The Australian National University

May 2018

Except where otherwise indicated, this thesis is my own original work.

Wai Keung Terrence Mak
8 May 2018

Dedicated to my family, and all computer scientists endlessly pushing the boundaries to improve the world.

Acknowledgments

$\mathscr{P}$ hD thesis, is an important milestone in one's life. It records someone's time, in a foreign country with kangaroos. It marks the progress of a research journey. It discloses many excitements and joys of a research program. In the end, it declares the birth of an academic researcher.

The long journey as a research student started as early as in 2009, when he was pursuing his M.Phil degree in Chinese University of Hong Kong. With the support from his former supervisor, he took the courage and flied himself to Australia in 2013 to start his PhD study in University of Melbourne and worked in the NICTA Victoria laboratory. In Melbourne, he met his supervisor and later transferred with him to the Australian National University in 2014, while working in the NICTA Canberra laboratory. Throughout the journey, there are many people, directly or indirectly, supporting his life and studies.

I would like to thank my PhD and post-doc supervisor Prof. Pascal Van Hentenryck for his endless support and supervision. He is always optimistic in research, and an exciting professor to work with. I would also like to thank my other academic advisors: Prof. Sylvie Thiebaux, Prof. Peter Stuckey, Dr. Hassan Hijazi, and Dr. Carleton Coffrin, and our collaborators: Prof. David Hill, Prof. Ian Hiskens, Prof. Yunhe Hou, Prof. Tao Liu, Dr. Anatoly Zlotnik, and Dr. Russeull Bent for their constructive ideas and helpful guidance. They help me a lot to strengthen my academic knowledge. They also assist me in exploring new research areas and directions. I would also like to thank all of my colleagues, lab-mates, and friends for supporting my research and life. They include, but are not limited to: Prof. Lexing Xie, Prof. Phil Kilby, Dr. Alban Grastien, Dr. Patrik Haslum, Dr. Tommaso Urli, Dr. Victor Pillac, Dr. Andreas Schutt, Dr. Feydy Thibaut, Dr. Caron Chen, Dr. Yury Kryvasheyeu, Dr. Harsha Nagarajan, Dr. Paul Scott, Dr. Andres Abeliuk, Felipe Maldonado Caro, Alvaro Flores, Rodrigo Gumucio, Edward Lam, Boon Ping Lim, Jing Cui, Fazlul Hasan Siddiqui, Alan Lee, Cody Christopher, Ksenija Bestuzheva, Frank Su, Arthur Maheo, Swapnil Mishra, Franc Ivankovic, Carlo Lim, and many more! I would also like to thank my former supervisor Prof. Jimmy Lee for his continuous career guidance, and his son Jasper Lee for discussing ongoing research in constraint programming and algorithmic theory. I also like to thank Justin Yip, a former PhD student of Pascal and a former research visitor of Jimmy, for introducing me to Pascal and guiding/co-authoring with me on my first conference paper in my life. I would also like to thank my current colleagues and students in University of Michigan for spending their time in reading and commenting on the thesis draft. Finally, to all students and researchers, I sincerely wish this thesis would be useful to your research and ongoing studies.

Abstract

Understanding the physical dynamics underlying energy systems is essential in achieving stable operations, and reasoning about restoration and expansion planning. The mathematics governing energy system dynamics are often described by high-order differential equations. Optimizing over these equations can be a computationally challenging exercise. To overcome these challenges, early studies focused on reduced / linearized models failing to capture system dynamics accurately. This thesis considers generalizing and improving existing optimization methods in energy systems to accurately represent these dynamics. We revisit three applications in power transmission and gas pipeline systems.

Our first application focuses on power system restoration planning. We examine transient effects in power restoration and generalize the Restoration Ordering Problem formulation with standing phase angle and voltage difference constraints to enhance transient stability. Our new proposal can reduce rotor swings of synchronous generators by over 50% and have negligible impacts on the blackout size, which is optimized holistically.

Our second application focuses on transmission line switching in power system operations. We propose an automatic routine actively considering transient stability during optimization. Our main contribution is a nonlinear optimization model using trapezoidal discretization over the 2-axis generator model with an automatic voltage regulator (AVR). We show that congestion can lead to rotor instability, and variables controlling set-points of automatic voltage regulators are critical to ensure oscillation stability. Our results were validated against POWERWORLD simulations and exhibit an average error in the order of 10^{-3} degrees for rotor angles.

Our third contribution focuses on natural gas compressor optimization in natural gas pipeline systems. We consider the Dynamic Optimal Gas Flow problem, which generalizes the Optimal Gas Flow Problem to capture natural gas dynamics in a pipeline network. Our main contribution is a computationally efficient method to minimize gas compression costs under dynamic conditions where deliveries to customers are described by time-dependent mass flows. The scheme yields solutions that are feasible for the continuous problem and practical from an operational standpoint. Scalability of the scheme is demonstrated using realistic benchmark data.

Contents

List of Figures

List of Tables

Introduction

1.1   An Overview on Energy Systems

Energy transportation systems are critical for transferring and supplying energy resources to support daily activities in our modern societies. These systems allow us to collect energy resources from generation points and transport them to customers. Electricity transmitted by power grids, natural gas flowing in gas pipelines, and water supply traveling through water systems are common types of energy resources and corresponding transportation systems. Energy sources are usually not geographically co-located with consumers. Apart from distributed generation such as photovoltaic (PV) systems, most customers still ***solely*** rely on energy transportation systems for satisfying their needs. A breakdown of such systems not only affects customers, but could also lead to disastrous events. For instance, on July 30, 2004, a gas pipeline was ruptured and later exploded in Belgium, killing 24 people and injuring over 120 [8]. On August 14-15, 2003, a major power outage occurred in the north-eastern coast of the U.S. and Canada. This event led to a situation where 50 million people were left without power [9].

The question on how to maintain an efficient, stable, and reliable transportation system is thus a critical question. Maintaining the systems in stable operating conditions is a mandatory requirement. In the U.S., the Federal Energy Regulatory Commission (FERC) regulates the power grid and issues new regulations/orders [10] to improve and enhance gird stability and efficiency. This translates to different optimization and control problems. For instance, in power (resp., natural gas) systems, the optimal power (resp., gas) flow problem is frequently solved by engineers to find the least cost generation (resp., natural gas) dispatch satisfying customer demands. To further account for stability and reliability, these energy systems will be routinely checked to ensure a stable control profile exists (e.g., frequency/voltage controls in power systems), bringing the system back to stable conditions when contingencies and faults occur. If no feasible control profile exists, a control problem will then be formulated to find the optimal/feasible control settings. Expansion planning problems are also useful in assisting power/natural gas utilities to understand how to expand and improve their systems. To reduce the computational complexity in solving these optimization and control problems, one popular practice is to ignore the transient dynamics during the optimization phase and consider only steady-state operations. The ignored dynamics will then be later checked via simulation software to ensure that the solutions are acceptable.

1.2   Computational Challenges with System Dynamics

Managing energy systems to meet stability and operational conditions requires modeling the physics underlying energy flows and constraints associated with transportation networks. In power systems, the Alternating-Current (AC) power flow equations [5] accurately describe power flows under steady state operations. To model transient dynamics, the classical generator "Swing" model [5] includes 2nd-order differential equations coupled with the non-convex AC power flow equations. The overall formulation can become intractable for optimization. In practice, higher-order differential models are needed to reason on detailed generator behaviours, resulting in higher-order differential equations for optimization. Similarly, for natural gas, the Euler equations describing the flow of natural gas along pipes are also nonlinear and differential in nature [11].

   To avoid computational intractability, early studies have resorted to using simplified models. In power systems, restoration planning tools usually adopt linearized power flow equations (e.g., the DC power flow equations) with simplified network models and only consider steady-state operations [12, 13, 14]. Detailed network behaviour and transient-states analysis is then conducted by engineers using simulation tools [15, 16, 17]. This approach can lead to sub-optimal plans since multiple iterations between optimization and simulation is needed before converging to a transient-stable solution. Previous research tried to address these issues, e.g., reducing the standing phase angles [18, 19, 20] and directly reasoning on rotor shafts [21]. In early research on transient dynamics, swing equations are modeled using a simplified generator model [5, 1, 22, 23]. Unfortunately, such models fail to capture modern equipments such as automatic voltage and frequency controllers.

1.3   Our Contributions

The primary goal of this thesis is to study optimization and planning problems featuring differential equations describing transient dynamics in energy systems. Three applications are considered in this work. In each case, we demonstrate the issues related to ignoring system dynamics, before embedding them into novel routines and models enhancing existing approaches. All formulations were validated using well-established simulators, and experimental evaluations were performed on various well-known benchmarks.

1.3.1   Restoration planning for power systems

Our first application focuses on power system restoration planning. We consider the Restoration Ordering Problem (ROP) [24] that jointly considers generator dispatch, load pickups, and restoration prioritization to minimize the size of the blackout while satisfying the network operational constraints. Prior work on the ROP restricts attention to determining an optimal sequence of AC-feasible steady-states, and does not consider transition stability from one steady-state to the others. We examine transient effects in power restoration and generalize the ROP formulation with standing phase angle and voltage difference constraints to enhance rotor angle stabilities. We show: 1) the DC power flow approximation is not appropriate, 2) both the standing phase angle and voltage difference constraints can reduce rotor swings of

synchronous generators by over 50%, and 3) by jointly considering both constraints with load pickups and generation dispaches, improvements in rotor swings have negligible impacts on the blackout size. Instead of using repair-based/local-search methods to find stable solutions based on the result from the original optimization routine [24], our model focuses on optimizing all the decisions globally (i.e. holistic optimization).

1.3.2   Transmission line switching for power systems

Our second application focuses on transmission line switching in power system operations. We consider the Optimal Transmission Switching (OTS) [25] problem that searches for the best sequence of lines to switch off in order to minimize generation costs. The formulation produces an optimal sequence of steady states without guaranteeing transient stability. Our simulation experiments on the IEEE-39 test case indicate the more congested the network is, the more difficult it becomes to ensure transient stability. We propose an automatic routine which actively considers transient stability during optimization. Our key contribution is a nonlinear optimization model for Transient-Stable Line Switching (TSLS), using trapezoidal discretization over a 4th-order 2-axis generator model with an automatic voltage regulator (AVR) consisting of an exciter and a stabilizer. The model features two types of control variables: generation dispaches and stabilizer parameters, and its objective function minimizes the rotor angle accelerations weighted by time in order to damp and stabilize the system. The key findings are highlighted as follows: 1) the more congested the system is, the more difficult it is to ensure rotor stability, 2) due to the lack of excitation controls in classical swing models, the classical model cannot maintain rotor stability for congested scenarios, 3) the variables controlling the set-points of the exciter and the stabilizer are critical to ensure rotor stability, in particular to maintain (small-signal) oscillation stability, and 4) the TSLS optimization results were validated against POWERWORLD simulations, and exhibit an average error in the order of 10^{-3} degree for rotor angles.

1.3.3   Optimal compression controls for natural gas pipeline systems

Our third contribution focuses on natural gas compressor optimization in natural gas pipeline systems. We consider the Dynamic Optimal Gas Flow (DOGF) problem, which generalizes the Optimal Gas Flow problem to capture the natural gas dynamics of a gas pipeline network. Early studies [26, 27, 28] focused on optimizing steady-state gas flows, for which the state equations are algebraic relations. However, it is no longer appropriate to restrict attention to steady-state approximations, which cannot adequately describe the physics of high volume gas flows that may fluctuate significantly throughout the day according to gas-fired generator dispatch and commitment schedules [29, 30]. Our main contribution is a computationally efficient method to minimize gas compression costs under dynamic conditions where deliveries to customers are described by time-dependent mass flows. Our optimization method uses a simplified representation of gas flow physics, provides a choice of discretization schemes in time and space, and exploits a two-stage approach to minimize energy costs and ensure smooth and physically meaningful solutions. The proposed scheme is validated using an adaptive time-stepping differential equation solver, and cross-compared with a different optimal

control scheme. The validation process indicates that our optimization scheme produces solutions with minimal pressure constraint violations and with physically meaningful mass flow and pressure trajectories that match well with the corresponding simulations. Our method provides a highly accurate solution to a 24-pipe gas benchmark in less than 30 seconds, and demonstrates scalability to three pipeline networks.

1.4   Thesis outline

The rest of the chapters are organized as follows. Chapter 2 presents the background material for this thesis, where fundamental equations, concepts, and notations are introduced. Chapter 3 presents our first application on power system restoration planning. Chapter 4 illustrates our second application on power system line switching. Chapter 5 presents our third application on natural gas compression optimization. We then conclude our thesis and discuss our future work in Chapter 6.

1.5   Publication

Parts of this thesis were published in various journals/venues. Our work on power system restoration planning was published in:

- [31] Terrence W.K. Mak, Carleton Coffrin, Pascal Van Hentenryck, Ian A. Hiskens, David Hill: Power system restoration planning with standing phase angle and voltage difference constraints. In: Proceedings of the 18th Power Systems Computation Conference (PSCC'14). Wroclaw, Poland (2014)

- [32] Hassan Hijazi, Terrence W. K. Mak, Pascal Van Hentenryck: Power system restoration with transient stability.In: Proceedings of the Twenty-Ninth AAAI Conference on Artificial Intelligence (AAAI'15). Austin, Texas (2015)

Our work on power system line switching was published in:

- [33] Terrence W.K. Mak, Pascal Van Hentenryck, and Ian A. Hiskens: A Nonlinear Optimization Model for Transient Stable Line Switching. In: Proceedings of the 2017 American Control Conference (ACC'17). Seattle, USA (2017)

Our work on natural gas compression optimization was published in:

- [34] Terrence W.K. Mak, Pascal Van Hentenryck, Anatoly Zlotnik, Hassan Hijazi, Russell Bent: Efficient dynamic compressor optimization in natural gas transmission systems. In: Proceedings of The 2016 American Control Conference (ACC'16). Boston, USA (2016)

The extended journal version was published in :

- [35] Terrence W.K. Mak, Pascal Van Hentenryck, Anatoly Zlotnik, Russell Bent: Dynamic Compressor Optimization in Natural Gas Pipeline Systems. In: INFORMS Journal on Computing. (IJOC'2018). Runner-up for the 2016 INFORMS Computing Society Student Paper Prize

1.6   Government funding acknowledgement

Background and Related Work

This chapter provides necessary background material for the rest of the thesis. In the first section, we will introduce notations and terminologies for electrical power systems. Power flow equations and the Load/Power Flow Problem will be introduced. We will present the fundamental Optimal Power Flow Problem (OPF), with discussion on two important variants: the original AC-OPF problem, and the simplified DC-OPF problem. We will then describe two important applications: power systems restoration and transmission line switching. Several types of stabilities will be introduced. In particular, we will consider small-signal stability and transient stability. In the second section, we will introduce notations and terminology for describing the natural gas transmission systems. The gas flow equations and the steady-state gas flow problem will then be discussed.

2.1 Electrical Power Systems

A traditional electrical power system [5] (also commonly called power grid) consists of three main components: a) generation sources for power *generation*, b) power lines and/or transformers for power *transmission*, and c) loads for power *consumption*.

Example 2.1.1. Figure 2.1 shows a small example of a power system. The example has two generators for power generation, three transmission lines for power transmission, three buses for power aggregation, and two loads for power consumption, which are commonly drawn as circles, connecting lines, line bars, and arrows respectively. Transmission lines can transmit electric power in any direction. We indicate them as dotted lines if they are opened (i.e., not in service). In this example, if generator 1 is the only operating generator, then power will flow in an anti-clockwise direction (i.e., from Bus 1 to Bus 3, and then from Bus 3 to Bus 2). If generator 2 is the only generator in service, power will flow in a clock-wise direction (i.e., from Bus 2 to Bus 3).
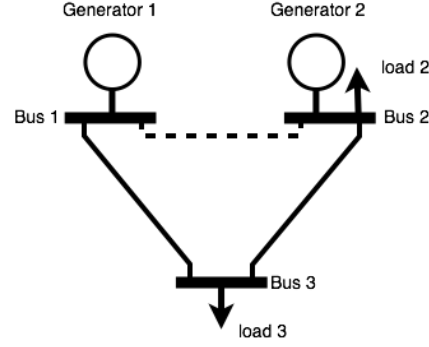
Figure 2.1: 3-bus power transmission system: 2 generators, 3 transmission lines, 3 buses, and 2 loads

Table 2.1: Nomenclature for power systems networks

Nomenclature for power network $\mathscr{P} = \langle N, L, G, O \rangle$	
N	Set of buses in the power network
$N(n) \subseteq N$	Subset of neighbouring buses which connect to bus n
L	Set of transmission lines in the power network
G	Set of generator machines
$G(n)$	Generators connecting to bus n
O	Set of demands/loads
$O(n) \subseteq O$	Subset of demands connected to bus n
$\widehat{S}, \widehat{V}$	MVA and voltage base for the per unit (p.u.) normalization
$\widehat{I}, \widehat{Z}, \widehat{Y}$	Current, impedance, and admittance base for the per unit (p.u.) normalization
p^n, q^n	(Net) Active and reactive power of bus n (p.u.)
$\widetilde{S}^n = p^n + iq^n$	(Net) Complex power of bus n (p.u.)
p^{nm}	Active power flow from bus n to m (p.u.)
q^{nm}	Reactive power flow from bus n to m (p.u.)
$\widetilde{S}^{nm} = p^{nm} + iq^{nm}$	AC/Complex power flow from bus n to m (p.u.)
r^{nm}, x^{nm}	Resistance and reactance of power line (n,m) (p.u.)
$z^{nm} = r^{nm} + ix^{nm}$	Impedance of power line (n,m) (p.u.)
g^{nm}, b^{nm}	Conductance and susceptance of power line (n,m) (p.u.)
$y^{nm} = 1/z^{nm} = g^{nm} + ib^{nm}$	Admittance of power line (n,m) (p.u.)
g_s^n	Conductance of bus shunts at bus n (p.u.)
b_s^n	Susceptance of bus shunts at bus n (p.u.)
l_c^{nm}	Line charge of line (n,m) (p.u.)
$\widetilde{V}^n, \widetilde{I}^n$	Complex voltage and complex (net) current of bus n (p.u.)
$\widetilde{V}^n = V^n \angle \theta^n$	Voltage magnitude & phase angle at bus n (p.u.)
Tr^{nm}	Transformer off-nominal turns ratio (p.u.) from bus n to m
ϕ^{nm}	Transformer phase shift from bus n to m
p_l^n, q_l^n	Active and reactive power loads at bus n (p.u.)
p_g^n, q_g^n	Active and reactive generation power at bus n (p.u.)
z^{nm}	On-off line switching variable/parameter
Θ^{nm}	Total phase difference for line (n,m)
$\overline{v}, \underline{v}$	Upper limits and lower limits of a real/complex quantity/variable v
v^*	Complex conjugate of a complex quantity/variable v
Δ	Discretization time constant (sec)

In practice, power systems split into three main classes: transmission, sub-transmission, and distribution. A *transmission system* [5] connects generators to the sub-transmission level.
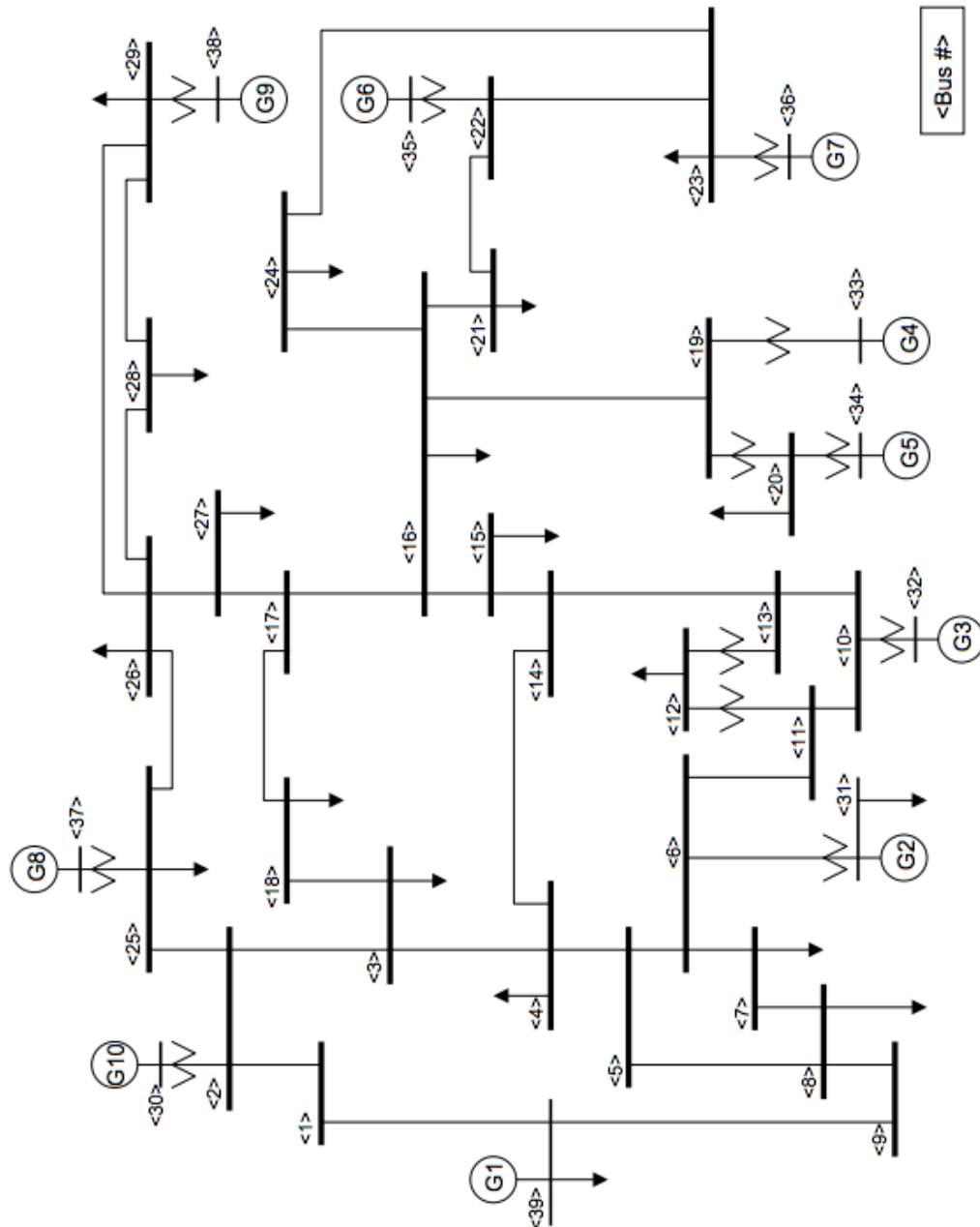
Figure 2.2: The classical IEEE-39 bus transmission system [1, 2] (©1979 IEEE). The improved figure (©2015 IEEE) is copied from the IEEE-PES technical report PES-TR18 (Figure 4.4) [3], which was first appeared from the 39 bus system MATLAB report [4].

It usually forms the backbone of the overall system and operates at high voltage levels (e.g. 230 kV or above). The *sub-transmission system* [5] transmits power received from generators and delivers to distribution systems. Large industrial customers are commonly supplied directly at the sub-transmission level. In some networks, the sub-transmission level is merged with the transmission system. The *distribution system* [5] transmits power to individual customers, and operates at low voltage levels. The primary distribution feeders supply small industrial customers at voltage levels of 4 kV to 35kV, and the secondary distribution feeders connects residential/home customers at common voltages of 100V to 240V. Power systems usually operate at a frequency of 50Hz or 60Hz. In terms of topology, distribution systems are mostly radial, with a limited number of cycles in exceptional cases. Transmission systems, e.g., the 10-generator 39-bus IEEE benchmark system [1, 2, 4] shown in Figure 2.2, are commonly found to be more meshed than distribution networks. A meshed network allows the system to be more robust towards faults and loss of equipments, e.g., $N-1$ contingency.

2.1.1 Terminologies and notations

In this thesis, we define a power system network $\mathscr{P}$ consists of at least the following four sets of equipments: a) a set of buses N, b) a set of transmission lines and transformers L, c) a set of generators G, and d) a set of loads O. In power systems, symbols are often abused to represent a quantity in different forms. For example, V may be used to represent complex voltage of an equipment at a particular time point, the complex magnitude of an equipment, or a voltage function of an equipment over a series of time points. To avoid confusion between a variable/quantity at a particular time point and its function series, we append '()' to all variables/quantities to represent its function series. In addition, to avoid confusion between complex variables n from its complex magnitude $|n|$, we add a '~' to the top of n when variable n **must** be represented in its complex form. We use S, p, and q to denote complex, active, and reactive power respectively. Voltage and current are represented by V and I respectively. We use z, r, and x to represent impedance, resistance, and reactance, and y, g, and b to represent admittance, conductance, and susceptance respectively. Table 2.1 presents a detailed list of notations for each equipment.

We assume power systems parameters and variables are normalized into the per-unit system (p.u.) [5]. In particular, we assume voltages are normalized by the voltage base $\widehat{V}$, and active, reactive, complex power are all normalized by the MVA power base $\widehat{S}$. The impedance base $\widehat{Z}$, admittance base $\widehat{Y}$, and current base $\widehat{I}$ are defined by the following formula:

$$\widehat{Z} = \frac{\widehat{V}^2}{\widehat{S}}, \quad \widehat{Y} = \frac{\widehat{S}}{\widehat{V}^2}, \quad \widehat{I} = \frac{\widehat{S}}{\widehat{V}}$$

For simplicity, we assume there is only one generator per bus. Therefore, $G \subseteq N$ and $G(n) = \{n\}$ if bus n has a generator, or otherwise, $G(n)$ is an empty set. This is generally valid for our work as: 1) we do not aim to study dynamics within generators of a power plant (e.g. intra-plant dynamic performance), and 2) our techniques for modeling and optimizing generator dynamics can easily extend to the general case. For ease of notation, we assume there is at most one power transmission line per pair of buses. We represent the transmission line connecting bus n to bus m by a pair $(n,m) \in L : L \subseteq N \times N$. If $(n,m) \in L$, then the

reverse line $(m, n) \in L$ (vice versa). If there are more than one transmission line (i.e., parallel lines) between a pair of buses, we will use reduction/approximation techniques to compute an equivalent line to replace the originals. We will keep the parallel lines when reducing to one transmission line gives significant differences/errors (e.g., significantly different operational requirements between the parallel lines). To differentiate these parallel lines, we add an extra circuit index number c to the pair (n, m). Let c_N be the maximum number of parallel lines in the corresponding power systems. Transmission lines will be represented by a tuple $(n, m, c) \in L : L \subseteq N \times N \times \{1, 2, \ldots, c_N\}$. Variables and parameters p^{nm}, q^{nm}, S^{nm}, r^{nm}, x^{nm}, Z^{nm}, g^{nm}, b^{nm}, Y^{nm}, l_c^{nm}, Tr^{nm}, ϕ^{nm}, z^{nm}, and Θ^{nm} will be generalized by replacing nm to nmc accordingly.

2.1.2 Power Flow Problem (PF)

One of the most important and fundamental problems in power systems research is the Power Flow problem, also known as the Load Flow Problem. The *Power Flow Problem* (PF problem) [5] in the literature involves the calculation of network power flows (e.g. p^{nm} and q^{nm} of transmission lines) and votages (V^n and θ^n of buses) of a transmission network subject to specific terminal/bus conditions or generator configurations. In this problem, all buses will have four variables: the net active power (P), the net reactive power (Q) flowing through the bus, voltage magnitude (V), and voltage angle (θ). Buses will be classified into one of four different types: voltage-controlled bus (PV bus), load bus (PQ bus), device bus, or the slack/swing ($V\theta$) bus. PV buses are typically used to model equipments like generators, synchronous condensers, and static var compensators, where the active power (P) and voltages (V) are both specified as input. PQ buses are typically used to model loads, where the active withdrawal (P) and reactive withdrawal (Q) are specified. Device buses are typically used to model buses with devices imposing special boundary conditions/configurations. Power losses in the system are usually not known a priori before solving the PF problem. If we fix all the generators to be PV buses and all the loads to be PQ buses, the system power flow cannot be balanced. In the literature, one classic solution is to set one of the buses with generators to be the slack bus, also known as the swing bus or the reference bus, to automatically balance the power flow. The voltage magnitude (V) and phase angle (θ) of this bus are fixed, and the active (P) and reactive power (Q) are free. This allows the active and reactive power to automatically balance the power flow during the search process to compensate for the unknown power losses. In the literature, the phase angle of the slack bus is usually set to 0. Three methods are typically used to solve the Power Flow problem [5]: 1) Gauss-Seidel Method, 2) Newton-Raphson method, and 3) fast decoupled load flow method. These methods generally solve a set of node equations [5] modeling the law of power flows.

Let $|N|$ to be the number of buses in the system. The *current flow node equation* for solving

the power flow problem is:

$$
\begin{bmatrix} \widetilde{I}^1 \\ \widetilde{I}^2 \\ \dots \\ \widetilde{I}^k \end{bmatrix} = \begin{bmatrix} Y^{11} & Y^{12} & \dots & Y^{1k} \\ Y^{21} & Y^{22} & \dots & Y^{2k} \\ & & \dots & \\ Y^{k1} & Y^{k2} & \dots & Y^{kk} \end{bmatrix} \begin{bmatrix} \widetilde{V}^1 \\ \widetilde{V}^2 \\ \dots \\ \widetilde{V}^k \end{bmatrix} \quad \text{(I)}
$$

$$
\text{where } Y^{nm} = \begin{cases} 0 & \text{if } n \neq m, (n,m) \notin L \\ -y^{nm} & \text{if } n \neq m, (n,m) \in L \\ \displaystyle\sum_{l \in N:(n,l) \in L} y^{nl} & \text{if } n = m \end{cases}
$$

$\widetilde{I}^n$ represents the complex current of bus $n \in N$ and $\widetilde{V}^n$ is the complex voltage.

This node equation implements the current law in matrix form. Each row n describes the current flow balance of bus n:

$$
\widetilde{I}^n = \sum_{l=1}^{k} Y^{nl}\widetilde{V}^l = Y^{n1}\widetilde{V}^1 + Y^{n2}\widetilde{V}^2 + \dots + Y^{nk}\widetilde{V}^k = \sum_{l \in N:(n,l) \in L} [y^{nl}(\widetilde{V}^n - \widetilde{V}^l)]
$$

The complex matrix Y is called the admittance matrix and is extensively used in power systems analysis [5]. Data is usually given in the form of real and reactive power. The current-based equation (I) requires transforming power data/variables to current data/variables. Therefore, the power-based formulation is a preferred alternative. To introduce the power-based formulation, we start by introducing the general AC power law:

$$
\widetilde{S}^n = p^n + iq^n = \widetilde{V}^n\widetilde{I}^{*n}
$$

After substituting with the current-based equations, we have:

$$
p^n + iq^n = \widetilde{V}^n[\sum_{l=1}^{k} Y^{nl}\widetilde{V}^l]^*
$$

Let G and B be the real and imaginary parts of the admittance matrix Y (i.e. $Y = G + iB$).

$$
p^n + iq^n = \widetilde{V}^n[\sum_{l=1}^{k}(G^{nl}\widetilde{V}^l + iB^{nl}\widetilde{V}^l)]^* = \widetilde{V}^n\sum_{l=1}^{k}([G^{nl}\widetilde{V}^l]^* + [iB^{nl}\widetilde{V}^l]^*)
$$

$$
= \widetilde{V}^n\sum_{l=1}^{k}(G^{nl}\widetilde{V}^{*l} - iB^{nl}\widetilde{V}^{*l}) = \widetilde{V}^n\sum_{l=1}^{k}(G^{nl} - iB^{nl})\widetilde{V}^{*l}
$$

We further expand the complex voltage into the polar form.

$$p^n + iq^n = V^n e^{i\theta^n} \sum_{l=1}^{k} (G^{nl} - iB^{nl}) V^l e^{-i\theta^l}$$

$$= \sum_{l=1}^{k} (V^n V^l e^{i(\theta^n - \theta^l)} G^{nl} - iV^n V^l e^{i(\theta^n - \theta^l)} B^{nl})$$

$$= \sum_{l=1}^{k} V^n V^l ([\cos(\theta^n - \theta^l) + i\sin(\theta^n - \theta^l)]G^{nl} - i[\cos(\theta^n - \theta^l) + i\sin(\theta^n - \theta^l)]B^{nl})$$

$$= \sum_{l=1}^{k} V^n V^l (G^{nl}\cos(\theta^n - \theta^l) + B^{nl}\sin(\theta^n - \theta^l) + i[G^{nl}\sin(\theta^n - \theta^l) - B^{nl}\cos(\theta^n - \theta^l)])$$

We further separate the equations into real and imaginary parts.

$$p^n = \sum_{l=1}^{k} V^n V^l (G^{nl}\cos(\theta^n - \theta^l) + B^{nl}\sin(\theta^n - \theta^l)), \text{ and}$$

$$q^n = \sum_{l=1}^{k} V^n V^l (G^{nl}\sin(\theta^n - \theta^l) - B^{nl}\cos(\theta^n - \theta^l))$$

for all $n \in N$. The above two equations are generally called the *AC power flow equations* [5]. We further expand the above two equations on a per-line basis $(n,m) \in L$. By further expanding the admittance matrix $Y = G + iB$, we obtain [36]:

$$p^n = \sum_{m \in N:(n,m)\in L} p^{nm}, \text{ where}$$

$$p^{nm} = g^{nm}[V^n]^2 - V^n V^m [g^{nm}\cos(\theta^n - \theta^m) + b^{nm}\sin(\theta^n - \theta^m)], \text{ and}$$

$$q^n = \sum_{m \in N:(n,m)\in L} q^{nm}, \text{ where}$$

$$q^{nm} = -b^{nm}[V^n]^2 - V^n V^m [g^{nm}\sin(\theta^n - \theta^m) - b^{nm}\cos(\theta^n - \theta^m)]$$

The above equations do not model transformers and line charges. To further implement these equipments, we replace the line equation for p^{nm} and q^{nm} [36, 37]:

$$p^{nm} = \frac{g^{nm}[V^n]^2}{Tl^{nm}} - \frac{V^n V^m}{Tr^{nm}}[g^{nm}\cos(\theta^n - \theta^m + \phi^{nm}) + b^{nm}\sin(\theta^n - \theta^m + \phi^{nm})], \text{ and}$$

$$q^{nm} = -\frac{b^{nm} + l_c^{nm}/2}{Tl^{nm}}[V^n]^2 - \frac{V^n V^m}{Tr^{nm}}[g^{nm}\sin(\theta^n - \theta^m + \phi^{nm}) - b^{nm}\cos(\theta^n - \theta^m + \phi^{nm})]$$

where ϕ^{nm} denotes the constant phase shifting angle from bus n to bus m if transmission line (n,m) has a phase shifting transformer/device. If there are no phase shifting transformers, then $\phi^{nm} = \phi^{mn} = 0$. Phase shifting is directional and $\phi^{nm} = -\phi^{mn}$. Tr^{nm} denotes the off-nominal turns ratio of a transformer installed on line (n,m), with $Tr^{nm} = Tr^{mn}$. It is set to 1 if no transformer exists. Tl^{nm} is a modeling parameter set to $[Tr^{nm}]^2$ if bus n connects to the *"from end"* of the transformer and bus m connects to the *"to end"* of the transformer; and set to 1 otherwise. Finally, we use the following two equations to link the net active/reactive power

flow to generation power, loads, and bus shunts:

$$p^n = p_g^n - p_l^n - [V^n]^2 g_s^n$$
$$q^n = q_g^n - q_l^n + [V^n]^2 b_s^n$$

Solving the Power Flow problem allows us to quickly obtain the steady-state [5] of the network, including power flow on transmission lines, voltage magnitudes and phase angles on buses, with respect to the current generator dispatch and load demands.

2.1.3   Optimal Power Flow Problem (OPF)

In power systems, the cost of generator operations depends on a number of factors, e.g., fuel types and generator scale, and varies from generator to generator. It would be natural for operational engineers to seek for an optimal generation dispatch minimizes generation costs while still satisfying the operational and safety constraints. The Optimal Power Flow Problem (OPF) [38, 39, 40] (or sometimes called Economic Dispatch Problem (ED)) was formulated to achieve this goal. Let p_g^n and q_g^n be the active power dispatch and reactive power dispatch of generator n, and $c(n, p_n^g)$ be the cost function evaluating the cost of generator n at active power p_n^g. The AC Optimal Power Flow Problem (ACOPF), based on the AC power flow equations, can be formulated as in Model 1. The goal of the problem is to search for a steady state, including voltage solutions V^n, θ^n, generator dispatch set-points p_g^n, q_g^n, and power flows p^{nm}, q^{nm}, such that the AC power flow equations are satisfied. We also incorporate the line thermal/power limit constraints as it is a common operational requirement. Since the AC power flow equations are nonlinear and non-convex, the problem is computationally challenging [41].

In the literature, many works [42, 25, 43, 44, 45, 24] use the linearized *DC power flow equation* [46], simplifying the AC power flow equation by: 1) ignoring the reactive power flow, 2) assuming voltages to be equal to 1 p.u., 3) ignoring resistance in the network, and 4) assuming the phase angle difference is small [36]. Ignoring reactive power flow allows to remove reactive power flows and the corresponding balance equations. By further assuming voltages equal to 1 p.u., we get:

$$p^{nm} = g^{nm} - [g^{nm} \cos(\theta^n - \theta^m + \phi^{nm}) + b^{nm} \sin(\theta^n - \theta^m + \phi^{nm})]$$

By further ignoring resistance assuming $g << b$, we obtain a more simplified equation.

$$p^{nm} = -[b^{nm} \sin(\theta^n - \theta^m + \phi^{nm})]$$

Finally, by assuming phase angles are usually small, we can ignore the sine function and all phase shifting actions by transformers / phase shifter.

$$p^{nm} = -b^{nm}(\theta^n - \theta^m)$$

Model 2 shows the linearized DC Optimal Power Flow problem. If the cost function $c(n, p_n^g)$ is linear, the problem will be reduced to a linear program and can be solved by efficient linear solvers. Many other DC power flow variants exist in the literature [47, 48, 49, 50].

Model 1 AC Optimal Power Flow

Inputs:

  $\mathscr{P} = \langle N, L, G, O \rangle$ Power network input

Variables:

  $V^n \in [\underline{V^n}, \overline{V^n}], \forall n \in N$ Voltage magnitude
  $\theta^n \in (-\pi, \pi), \forall n \in N$ Voltage phase angle
  $p_g^n \in [\underline{p_g^n}, \overline{p_g^n}], \forall n \in G$ Active power dispatch
  $q_g^n \in [\underline{q_g^n}, \overline{q_g^n}], \forall n \in G$ Reactive power dispatch
  $p^{nm} \in [\underline{p^{nm}}, \overline{p^{nm}}], \forall (n,m) \in L$ Active power flow
  $q^{nm} \in [\underline{q^{nm}}, \overline{q^{nm}}], \forall (n,m) \in L$ Reactive power flow

Minimize

  $\displaystyle \sum_{n \in G} c(n, p_g^n)$

Subject to:

$$\sum_{m \in G(n)} p_g^m - \sum_{m \in O(n)} p_l^m - [V^n]^2 g_s^n = \sum_{m \in N(n):(n,m) \in L} p^{nm} \qquad \forall n \in N$$

$$\sum_{m \in G(n)} q_g^m - \sum_{m \in O(n)} q_l^m + [V^n]^2 b_s^n = \sum_{m \in N(n):(n,m) \in L} q^{nm} \qquad \forall n \in N$$

$$p^{nm} = \frac{g^{nm}[V^n]^2}{Tl^{nm}} - \frac{V^n V^m}{Tr^{nm}} [g^{nm} \cos(\theta^n - \theta^m + \phi^{nm}) + b^{nm} \sin(\theta^n - \theta^m + \phi^{nm})] \qquad \forall (n,m) \in L$$

$$q^{nm} = -\frac{b^{hm} + l_c^{nm}/2}{Tl^{nm}} [V^n]^2 - \frac{V^n V^m}{Tr^{nm}} [g^{nm} \sin(\theta^n - \theta^m + \phi^{nm}) - b^{nm} \cos(\theta^n - \theta^m + \phi^{nm})] \qquad \forall (n,m) \in L$$

$$[p^{nm}]^2 + [q^{nm}]^2 \leq |\widetilde{S^{nm}}|^2 \qquad \forall (n,m) \in L$$

Model 2 DC Optimal Power Flow

Inputs:

  $\mathscr{P} = \langle N, L, G, O \rangle$ Power network input

Variables:

  $\theta^n \in (-\pi, \pi), \forall n \in N$ Voltage phase angle
  $p_g^n \in [\underline{p_g^n}, \overline{p_g^n}], \forall n \in G$ Active power dispatch
  $p^{nm} \in [\underline{p^{nm}}, \overline{p^{nm}}], \forall (n,m) \in L$ Active power flow

Minimize

  $\displaystyle \sum_{n \in G} c(n, p_g^n)$

Subject to:

$$\sum_{m \in G(n)} p_g^m - \sum_{m \in O(n)} p_l^m = \sum_{m \in N(n):(n,m) \in L} p^{nm} \qquad \forall n \in N$$

$$p^{nm} = -b^{nm}(\theta^n - \theta^m) \qquad \forall (n,m) \in L$$

$$p^{nm} \leq \overline{p^{nm}}, p^{nm} \geq -\overline{p^{nm}} \qquad \forall (n,m) \in L$$

Since the DC model does not capture reactive power, it cannot be applied to problems requiring reactive power to be modeled explicitly, e.g., capacitor placement problem [51] and voltage stability analysis [5]. Moreover, the accuracy of the model is also an open point of discussion [42, 46, 52, 53, 54, 55]. The question on how to bridge the gap between linearized DC power flow model and non-linear AC power flow models is also an opened path to study, leading to several interesting recent work: LPAC model [36], QC model [37], and SDP model [56].

2.1.4   Applications based on Optimal Power Flow (OPF)

This section further introduces two power systems applications based on the Power Flow and the Optimal Power Flow problem.

2.1.4.1   Power systems restoration

Power outage may occur when equipments of a power network, e.g., electric buses, transmission lines, transformers, or generators, are faulty / damaged. Users of the faulty power network will usually face phenomena, ranging from a complete blackout, unstable electricity supply, to a short-period power outage. Once power engineers discover that the network is faulty, the restoration process starts immediately. For a severe power system breakdown (e.g., a large electricity blackout), the processes are coarsely divided into three phases [16]:

1. Planning Phase: Devise plans to restart and reintegrate the power supply in the transmission network.

2. Degradation Phase: Perform actions to retain and restore critical sources of power.

3. Restoration Phase: After the system has been stabilized at the degraded state, restore the system to its nominal state.

To successfully complete the above restoration phases, power engineers will usually need to perform four generic tasks (based on Adibi and Fink's restoration paradigm [15]) as shown in Figure 2.3.
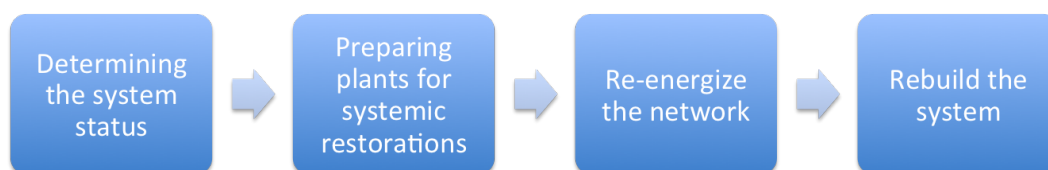
Figure 2.3: The four restoration steps

The first and second task aim to determine the system status and prepare power plants / network for systematic restoration. The third task re-energizes the network, and the fourth task rebuilds the system. Our contribution lies in globally optimizing a restoration plan to assist in rebuilding the system (i.e., the fourth task).

During the system rebuilding process, engineers may prefer to split the power network into multiple parts/sections, with multiple islands, to speed up the restoration processes [15, 17]. A good restoration plan should be computed to guide the engineers to restore and maintain stability of the system. For example, when we close a line breaker within a partially restored network, we have to make sure the difference between the phase angles across the breaker is small [15, 16]. If the angle is too large and the breaker is closed, stability problems may be observed causing system damage during restorations. In addition, generator stability is also an important topic during load restorations. Coordinating the restorations of the loads to ensure stability is required, and the loading behaviour of generators are necessary to be observed [15, 16]. Connecting a load without enough generation capability will lead to generators tripping off, causing delays to the whole restoration. Coordination between power plants and field operators is required. These two issues were addressed by the first part of our thesis during the optimization of the restoration plans.

Power systems restoration: written plans   Devising a plan to efficiently restore a power system is complex. The combinations of possible restoration actions are usually intractable and finding the optimal restoration sequence is computationally hard. Traditionally, power engineers use written restoration plans and procedures as a guidance to perform power systems recovery. These plans and procedures are usually prepared and made based on postulated conditions to give the most effective ways to restore a power system. However, since these written plans are static in nature, they cannot immediately be changed if the actual real-world conditions differ from the postulated conditions. In general, real-world constraints and limiting conditions are hard to predict and it is usually infeasible to enumerate written plans for all possible combinations of conditions. Once power engineers are unable to apply the plan, they are forced to recover the system based on intuition and experience. One main disadvantage of written restoration plans is they are usually written in text. Textual information is intended to be read sequentially. It is hard for power engineers to understand all of the text immediately and perform restorations, particularly under stress and tight time-constraint [17]. Another disadvantage of written plans is that they may not be updated efficiently when the system is changed or upgraded. In a review of 48 major disturbances list, reviewers showed that outdated written plans was the second leading cause of restoration problems [17].

Power systems restoration planner: knowledge-based systems   To overcome these disadvantages, knowledge-based expert systems are developed, e.g., Restoration Assistant [57]. These systems usually have the capability to compute and give real-time restoration plans based on actual limitations and conditions. Updating knowledge-based systems to reflect changes in the power system is easier than updating written plans. Once the software is checked and updated, downloading the software to the expert system machines requires far less time than printing written plans.

Power systems restoration planner: optimization approach   Apart from knowledge-based expert systems, systems using mathematical programming approaches are also popular to assist power engineers in performing power systems recovery, in particular, to obtain global optimal plans minimizing restoration time. Traditionally, approaches finding global optimal

---

Model 3 DC Restoration Model

Inputs:

$\mathscr{P} = \langle N, L, G, O \rangle$	- Power network input
$A = N \cup L \cup G \cup O$	- The global set of equipments in power systems
$\mathscr{D}$	- Set of damaged items
$\mathscr{R} \subseteq \mathscr{D}$	- Set of damaged items considered by this algorithm

Variables: (Step r, $0 \leq r \leq |\mathscr{R}|$)

$h^n(r) \in \{0,1\}, \forall n \in A$	- Item n is going to be repaired (or not) at step r
$k^n(r) \in \{0,1\}, \forall n \in A$	- Item n is working/functioning (or not) at step r
$\theta^n(r) \in (-\pi, \pi), \forall n \in N$	- Bus phase angle of bus n at step r
$p_g^n(r) \in [0, \overline{p_g^n(r)}], \forall n \in G$	- Active power by generator n at step r
$p^{nm}(r) \in [\underline{p^{nm}(r)}, \overline{p^{nm}(r)}], \forall (n,m) \in L$	- Power flow on line (n,m) at step r
$p_l^n(r) \in [0, \overline{p_l^n(r)}], \forall n \in O$	- Power consumed by load n at time-step r

Maximize

$$\sum_{n \in O} \sum_{r=0}^{|\mathscr{R}|} p_l^n(r) \tag{O1}$$

Subject to: ($0 \leq r \leq |\mathscr{R}|$)

$$h^n(r) = 1, \qquad\qquad\qquad\qquad \forall n \in A \backslash \mathscr{D} \tag{C2.1}$$

$$h^n(r) = 0, \qquad\qquad\qquad\qquad \forall n \in \mathscr{D} \backslash \mathscr{R} \tag{C2.2}$$

$$\sum_{n \in \mathscr{D}} h^n(r) = r, \tag{C2.3}$$

$$h^n(r-1) \leq h^n(r), \qquad\qquad\qquad \forall n \in \mathscr{D}, 1 \leq r \leq |R| \tag{C2.4}$$

$$k^n(r) = h^n(r), \qquad\qquad\qquad\qquad \forall n \in N \tag{C3.1}$$

$$k^m(r) = h^m(r) \wedge h^n(r), \qquad\qquad \forall n \in N, \forall m \in G(n) \cup O(n) \tag{C3.2}$$

$$k^l(r) = h^l(r) \wedge h^n(r) \wedge h^m(r), \qquad \forall (l:n,m) \in L \tag{C3.3}$$

$$\sum_{m \in G(n)} p_g^m(r) - \sum_{m \in O(n)} p_l^m(r) = \sum_{m \in N(n):(n,m) \in L} p^{nm}(r) \;\; \forall n \in N \tag{C4.1}$$

$$\neg k^n(r) \rightarrow p_g^n(r) = 0, \qquad\qquad\qquad \forall n \in G \tag{C4.2}$$

$$\neg k^n(r) \rightarrow p_l^n(r) = 0, \qquad\qquad\qquad \forall n \in O \tag{C4.3}$$

$$\neg k^l(r) \rightarrow p^{nm}(r) = 0, \qquad\qquad\qquad \forall (l:n,m) \in L \tag{C4.4}$$

$$k^l(r) \rightarrow p^{nm}(r) = -b^{nm}(\theta^n - \theta^m), \qquad \forall (l:n,m) \in L \tag{C4.5}$$

---

plans are often criticized due to poor computational efficiency [57, 14]. With advances in hardware performance and optimization algorithms, global approaches are gaining more popularity.

This thesis is based on the work of Coffrin et. al. [13], which uses the simplified DC power flow equations to compute the power flow. We will briefly show and describe their optimization model. Model 3 shows the restoration model [13] tackling the restoration ordering problem for restoring a power network. The goal of the problem is to find a restoration sequence such that loads could be restored as soon as possible. In addition to finding the restoration sequence, Model 3 also computes the required generation dispatch, load pickups, and the amount of power flowing through each transmission line at each restoration step. The problem is a mixed-integer linear program. The number of binary variables increases with the number of equipments to be restored, leading to an exponential increase in the combinations of possible restoration sequences (in $O(2^{|\mathscr{R}|})$).

We now explain the variables and constraints in Model 3. The model reasons on $|\mathscr{R}| + 1$ steady states with DC power flow approximations, and aims to find the best sequence of steady-states restoring the maximum amount of loads by Objective O1. The model introduces two new types of binary variables $h^n(r)$ and $k^n(r)$ (with $|\mathscr{R}| + 1$ copies) to indicate the status of the equipments in the network. Variable $h^n(r)$ is set to 1 (resp. 0) if and only if item n in step r is repaired (resp. is not repaired), and variable $k^n(r)$ is set to 1 (resp. 0) if and only if item n in step r is functioning (resp. not functioning). We define A to be the union of all buses, loads, and generators. For clarity reasons, we use $(l : n,m)$. In C2.1, we assume all undamaged items to be classified as repaired. In C2.2, we assume all damaged items that are not going to be restored to be classified as not repaired. Constraint C2.3 ensures only one item is being repaired per restoration step. Constraint C2.4 ensures an item being repaired at a particular time-step will be set as repaired in all later time-steps. Constraint C3.1 enforces all repaired buses are functioning immediately. Generators, transmission lines, and loads, all have to be connected to functioning buses. C3.2 and C3.3 restrict these items to be functioning if and only if the associated buses are restored. Constraint C4.1 implements the power flow balance equation. Constraints C4.2, C4.3, and C4.4 ensure that no power is flowing through non-functioning items. The last constraint C4.5 implements the DC power flow equation for functioning lines. Some constraints in Model 3 are logic constraints, and we can linearize them during implementation using the big-M approach [58].

2.1.4.2 Transmission line switching

Transmission line switching is an important control action in electrical power systems, and has generated increasing attention in recent years. Opening and closing transmission lines change the topology of the grid. It is a useful tool to redistribute power flows and change the operational state of the system. Changing the topology could potentially save 10%, or even up to 25% of the economic cost [59, 60, 25]. It also provides opportunities to eliminate congestion and avoid violating operational constraints [61]. Line switching is also an important tool in power systems restoration.

Significant research has been devoted to designing algorithms for Optimal Transmission Switching (OTS) [25]. The goal in OTS is to find the best subset of lines to switch off in order to minimize generation costs. This line of research almost exclusively focuses on analyzing power flow under steady-state before and after the switching. From a mathematical standpoint, the OTS problem is a non-convex Mixed-Integer Non-Linear Program (non-convex MINLP), which is computationally challenging. For this reason, most OTS studies replace the non-convex AC power flow equations by the linear DC power flow equations [25, 62, 63, 64, 65]. This reduces the computational complexity, as the DC-OTS problem can be modeled as a Mixed-Integer Linear Program (MILP). The optimal solution, with integer variables fixed to the optimal values, can be used as a starting solution point and fed into an ACOPF solver to convert into an AC feasible solution. Unfortunately, there is no guarantee that the resulting solution can be transformed into an AC-feasible solution [66, 67]. To overcome this limitation, recent work has advocated the use of AC formulations (AC-OTS), or focusing on tighter approximations and relaxations [59, 60, 68].

Example 2.1.2. Figure 2.4 shows a 3-bus example [59] to illustrate the concepts of line switch-

ing. Without loss of generality, we assume the system is a transmission system with $\widehat{S}$ base = 100 MVA and $\widehat{V}$ = 230kV. In this example, we have three buses, three transmission lines, and only one load at bus 3 drawing 1 p.u. of active power (i.e. 100MW) and 0 p.u. reactive power. The buses are assumed to be operating within the range of [0.9, 1.1] p.u. voltage magnitude. Line (1,2) and line (2,3) both have negligible resistance and 0.05 p.u. reactance (i.e. $z^{23} = z^{12}$ = 0 + i 0.05). Line (1,3) has a larger resistance and reactance of both 0.10 p.u. (i.e. z^{13} = 0.10 + i 0.10). For simplicity, we neglect line charge l_c^{nm} and bus shunts g_s^n and b_s^n. There are two generators in the system: one cheap distant generator at bus 1 and one expensive generator at bus 3 located directly on the bus with the load. The cheapest solution is to deliver as much power as possible from generator 1 to avoid using generator 3. For simplicity, we assume the cost function of both generator are linear: $c(1, p_g^1) = p_g^1$ and $c(3, p_g^3) = 10p_g^3$. We first ignore voltage bounds and line thermal/power limiting constraints. Closing line (2,3) will result in cheaper generation costs of \$101 comparing to opening line (2,3) with a cost of \$110. Costs in both cases are higher than \$100 due to line losses. Adding lines to the network decreases the aggregate network resistance, and therefore resulting in a cheaper generation costs to supply the load. We now consider two congestion cases: 1) imposing a tight thermal/power limit of $\widetilde{S^{nm}}$ = 1 p.u. (MVA) on line (2,3), and 2) reducing the voltage range to [0.98, 1.02] p.u.. Table 2.2 reports the OPF solution with various power flow equations [59]. With the original AC power flow equations, opening line (2,3) reduces the generation costs by more than 80% for case 1, and increases the generation costs for case 2. The results are further matched by two relaxation techniques: SDP relaxation and QC relaxation (with 5 deg phase bounds). Since the linearized DC power flow model are a coarse approximation omitting reactive power and voltages, the model is not capable to handle voltage congestions in case 2 with significant errors.

Table 2.2: OPF solution: Two different congestion settings on four power flow models

Power Flow Model	Con. case 1		Con. case 2	
	Line open	Line close	Line open	Line close
AC-OPF	110	985	655	102
SDP-OPF	110	972	655	102
QC-OPF (5 deg)	110	772	655	102
DC-OPF	100	986	100	100
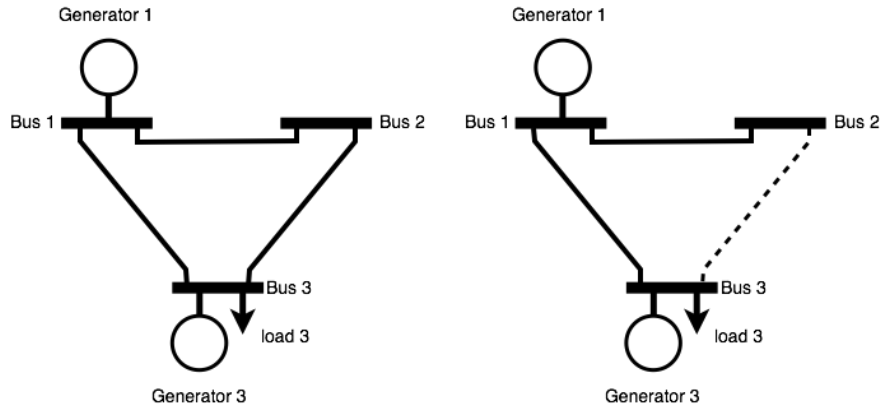
Figure 2.4: 3-bus power transmission system: Line switching example

Transmission Line Switching Model   Let L_s be the subset of transmission lines $(n,m) \in L$ where $n < m$, and L_r be the subset of transmission lines in L where $n > m$. We now show the general line-switching model in Model 4 for switching-off k transmission lines based on a previous formulation [59]. The model introduces extra binary variables z^{nm} for every transmission line $(n,m) \in L_s$ to indicate whether it should be switched-off ($z^{nm} = 0$) or not ($z^{nm} = 1$). The objective (O1) and power flow balance constraints (C2.x) are the same as in Model 1. Major modifications are on the AC power flow equations and thermal limit bounds (C3.2 - C3.7). We add z^{nm} to these equations to enforce: case 1) no power flow if the line is switched-off (i.e., $z^{nm} = 0$), or case 2) AC power flow within feasible bounds if the line is not going to be switched-off (i.e., $z^{nm} = 1$). We avoid re-defining an extra set of line switching variables z^{nm} for the reverse lines in L_r, by linking their power flows to the line switching variables of their counterparts in (C3.5 - C3.7). C3.1 restricts the model to search for solutions switching only k lines. We can remove C3.1 if we aim for solutions switching any number of lines.

Model 4 AC Optimal Transmission Switching Model

Inputs:

$\mathscr{P} = \langle N, L, G, O \rangle$ Power network input

k Number of lines to be switched off

Variables:

$V^n \in [\underline{V^n}, \overline{V^n}], \forall n \in N$ Voltage magnitude

$\theta^n \in (-\pi, \pi), \forall n \in N$ Voltage phase angle

$p_g^n \in [\underline{p_g^n}, \overline{p_g^n}], \forall n \in G$ Active power dispatch

$q_g^n \in [\underline{q_g^n}, \overline{q_g^n}], \forall n \in G$ Reactive power dispatch

$p^{nm} \in [\underline{p^{nm}}, \overline{p^{nm}}], \forall (n,m) \in L$ Active power flow

$q^{nm} \in [\underline{q^{nm}}, \overline{q^{nm}}], \forall (n,m) \in L$ Reactive power flow

$z^{nm} \in \{0,1\}, \forall (n,m) \in L_s$ Line switching variable

Minimize

$$\sum_{n \in G} c(n, p_g^n) \tag{O1}$$

Subject to:

$$\sum_{m \in G(n)} p_g^m - \sum_{m \in O(n)} p_l^m - [V^n]^2 g_s^n = \sum_{m \in N(n):(n,m) \in L} p^{nm} \qquad \forall n \in N \tag{C2.1}$$

$$\sum_{m \in G(n)} q_g^m - \sum_{m \in O(n)} q_l^m + [V^n]^2 b_s^n = \sum_{m \in N(n):(n,m) \in L} q^{nm} \qquad \forall n \in N \tag{C2.2}$$

$$\sum_{(n,m) \in L_s} z^{nm} = |L_s| - k \tag{C3.1}$$

$\forall (n,m) \in L_s:$

$$p^{nm} = z^{nm} \times \left\{ \frac{g^{nm}[V^n]^2}{Tl^{nm}} - \frac{V^n V^m}{Tr^{nm}} [g^{nm}\cos(\theta^n - \theta^m + \phi^{nm}) + b^{nm}\sin(\theta^n - \theta^m + \phi^{nm})] \right\} \tag{C3.2}$$

$$q^{nm} = z^{nm} \times \left\{ -\frac{b^{nm} + l_c^{nm}/2}{Tl^{nm}}[V^n]^2 - \frac{V^n V^m}{Tr^{nm}}[g^{nm}\sin(\theta^n - \theta^m + \phi^{nm}) - b^{nm}\cos(\theta^n - \theta^m + \phi^{nm})] \right\} \tag{C3.3}$$

$$[p^{nm}]^2 + [q^{nm}]^2 \leq \overline{|\widetilde{S^{nm}}|}^2 \times z^{nm} \tag{C3.4}$$

$\forall (n,m) \in L_r:$

$$p^{nm} = z^{mn} \times \left\{ \frac{g^{nm}[V^n]^2}{Tl^{nm}} - \frac{V^n V^m}{Tr^{nm}}[g^{nm}\cos(\theta^n - \theta^m + \phi^{nm}) + b^{nm}\sin(\theta^n - \theta^m + \phi^{nm})] \right\} \tag{C3.5}$$

$$q^{nm} = z^{mn} \times \left\{ -\frac{b^{nm} + l_c^{nm}/2}{Tl^{nm}}[V^n]^2 - \frac{V^n V^m}{Tr^{nm}}[g^{nm}\sin(\theta^n - \theta^m + \phi^{nm}) - b^{nm}\cos(\theta^n - \theta^m + \phi^{nm})] \right\} \tag{C3.6}$$

$$[p^{nm}]^2 + [q^{nm}]^2 \leq \overline{|\widetilde{S^{nm}}|}^2 \times z^{mn} \tag{C3.7}$$

2.1.5 Power systems stability: Types and characteristics

Power System Stability is a term broadly defined as a property of a power system enabling it to remain in a state of operating equilibrium under normal operating conditions, and to regain an acceptable state of equilibrium after being subject to disturbances [5]. When disturbance occurs (e.g., contingency situations), a stable system will reach an acceptable equilibrium, possibly a degraded or non-optimal equilibrium state. To study power systems stability, it is necessary to understand how a power system becomes unstable. In the literature, several different classification systems are used to classify power systems stability. The thesis mainly follows the classification of stability by their types [5]:

1. Rotor angle stability, with a further sub-classification into:

   - Transient stability or large disturbance angle stability and
   - Small-signal stability;

2. Voltage stability, with a further sub-classification into:

   - Large disturbance voltage stability and
   - Small disturbance voltage stability.

In some cases, it is better to classify stability study based on time-range [5, 69]:

1. Short-term stability: seconds scale,

2. Mid-term stability: minutes scale,

3. Long-term stability: hours scale.

In addition, we can also classify stability by their respective control dynamics and processes [69]:

1. Electrical machine and system dynamics,

2. System governing and generation control, and

3. Prime-mover energy supply dynamics and control.

Since our contribution mainly lies on the area of rotor angle stability, we will introduce rotor angle stability, including the two sub-classes: transient stability and small-signal stability, in below subsections.

2.1.5.1   Rotor Angle Stability

Rotor angle stability study (sometimes called rotor angle study/rotor study) involves the investigation of electromechanical oscillations in power systems, primarily due to the rotor oscillations in synchronous generator machines [5]. These oscillations affect the ability of interconnected synchronous machines to synchronize [5] with each other, and may lead to generator being tripped, and in the worst case a major power system outage/blackout. Rotor angle study are usually divided into small-signal stability and transient stability.

Small-signal Stability   *Small-signal stability* [5] is the ability of the power systems to stabilize when small disturbances occur. Typical small disturbances include small variations in loads and generations during operations. Linearized system equations/analysis [5] are usually sufficient for studying the system behaviour. How the system responds to these small disturbances depends on a wide variety of factors, including the initial operating conditions, the reliability of the transmission system, and the control equipments. Traditionally, if a generator without an automatic voltage regulators (AVR) is connected to a power system, instabilities are often caused by a lack of sufficient synchronizing torque [5]. With automatic voltage regulators pre-installed providing synchronizing torque support, small-signal instability are often caused by insufficient damping torque. Oscillation instability can be further sub-classified into four sub-types [5]: local/machine-system modes, interarea modes, control modes, and torsional modes.

Transient Stability   *Transient Stability* (TS) [5] is the ability of a power system to stabilize subjected to severe disturbances, for example transmission equipment faults, a loss of a generator unit, or a loss of a substation. When such disturbances occur, the steady-state of a power system usually changes even if the system manages to stabilize. The system will be operating in a degradation state, and may not be necessarily close to any of the previous states. Analyses and simulations to test the transient stability of the system are important, especially to cope with natural disasters capable to damage system equipments. Since large disturbances involve large rotor angle swings, linearized equations are no longer accurate and nonlinear relationships have to be considered.

Even if the system manages to reach a new steady state after the fault is cleared, ensuring small-signal stability in the new steady state is also important. Otherwise, the system will soon become unstable when small changes (e.g., load variations) occur. Equipments being tuned for the nominal operational state may not guarantee to stabilize the system in a new steady state. Finding a robust setting on machines and equipments for all possible contingency situations to ensure stability is a challenging problem [22, 23, 70]. Some typical contingency cases are one phase-to-ground faults, three-phase to ground faults, and transformer faults. Similar to small-signal stability, instability can be caused by insufficient synchronizing torque, insufficient damping torque, or both at the same time.

In the literature [71, 72, 73, 74, 75, 76], *first-swing stability* is widely studied. Instabilities of this sub-type are caused by rotor angles of generators increasing/decreasing steadily, due to insufficient synchronizing torque. Rotor swings can hardly be observed in this type of studies as the system quickly becomes unstable before the first/second swing is formed. In the literature, various synchronous machine models are proposed for studying transient stability problems, ranging from the 6th order Sauer-Pai model [69] / Anderson-Fouad model [77], the 4th order Two-Axis model [69], the 3rd order One-Axis Flux-Decay model [69], to the classic 2nd order "Swing" model [69, 5].

Our thesis investigate transient stability on two challenging optimization problems. We first study stability issues, in particular first-swing stability, when we perform optimization in power system restoration planning. We then focus on small-signal stability when we tackle the Optimal Transmission Switching Problem (OTS). The classical 2nd order "Swing" model is used in our first study, and we use the 4th order Two-Axis model in our second study. The detailed equations for both models will be introduced in later chapters.

Synchronous machine mechanics   To explain why rotor oscillations would lead to instabilities, it is useful to introduce the common architecture and mechanics of a three-phase synchronous generator. Figure 2.5 shows an abstract schematic diagram for a three phase generator machine [5]. The machine contains two different kinds of windings: field windings on the rotor (in the middle of Figure 2.5) driven by the prime mover/turbine, and armature windings on the stator connected to the power transmission systems. The field windings are usually excited by direct current, which is controllable through Automatic Voltage Regulators (AVR). When the prime mover/turbine drives the rotor to rotate, the rotating magnetic field from the field windings will induce alternating voltages in the armature windings, delivering electrical energy to the power systems. With proper physical arrangement in a generator, the rotating magnetic field in the stator rotates at the same speed as the rotor, and interacts with the mag-
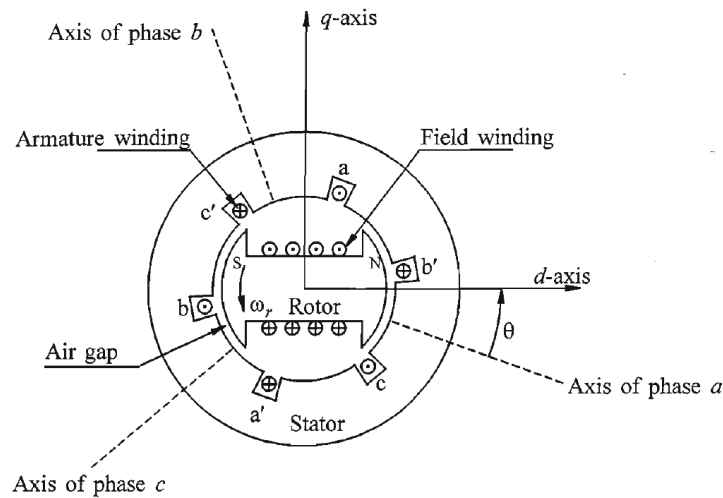
Figure 2.5: Schematic diagram of a synchronous generator from P. Kundur, Power System Stability and Control [5] (©McGraw-Hill Education).

netic field in the rotor. This will produce an electromagnetic torque opposing the rotation of the rotor. The force is balanced and energy is conserved in the machine. As a result, kinetic energy from the prime movers/turbines will be converted to magnetic energy, and finally to electrical energy for the power grid.

Based on this design, the frequency of the system hence depends on the speed of the rotor, and keeping the speed of the rotor constant (via controlling the mechanical torque and its energy sources) is important to maintain stability. If the mechanical torque and the electrical torque are perfectly balanced, the rotor will be rotating at a constant speed. If the mechanical torque is slightly higher (or lower) than the electrical torque, the rotor will be rotating slightly faster (or slower), resulting in an rotor advance (or retard) to a new position relative to the revolving stator magnetic field. This movement is usually measured in terms of angles in degrees/radians and it is vital to keep the rotor angle stability. In practice, the electrical torque/power are varied constantly from time to time, and advanced control methods are used to control and stabilize the systems.

Synchronizing multiple generators   In a power grid, we have more than one generator. Coordinating and maintaining the frequency of all the machines are necessary to maintain stability. If one machine temporarily supplies a surplus of mechanical torque, the angular position of its rotor relative to the other machines will advance, resulting in new angular differences between the other generators. This action usually implies transferring parts of the load from other machines to the current machine. If there is a large enough counter-force to reduce the speed difference and angular separation, the system would be able to stabilize and continue to be operational. On the other hand, if the counter-force cannot stabilize the system (e.g., caused by a huge disturbance), we will have a machine running at a different frequency. This process is called losing synchronism. Generators falling out of step with other generators (also

called pole-slipped) are no longer useful. In practice, these machines will be automatically tripped-off to avoid causing further damages.

In power systems, the rate of change in electrical torque ΔT_e of a synchronous machine following a perturbation can be coarsely split into two components [5]:

$$\Delta T_e = T_s \Delta \delta + T_D \Delta \omega$$

where the first term on the right-hand side denotes the *synchronizing torque* component and the second term denotes the *damping torque* component. T_s, $\Delta \delta$, T_D, and $\Delta \omega$ are the synchronizing torque coefficient, rotor angle perturbation, damping torque coefficient, and rotor speed deviation respectively. Synchronizing torque prevents a steady increase/decrease in rotor angles over time from the original position, while damping torque prevents rotor oscillations of increasing amplitude.

Example scenario: Load variations   In general, a disturbance in power system could potentially lead to multiple stability issues, if not handled properly by the equipments/devices in the power system. We now briefly discuss a load pickup example to illustrate the complexity. Suppose now an industrial customer decides to start-up his/her industrial equipments and draws a significant amount of electricity from the power grid. An increase in load consumption leads to an increase in the electrical power drawn from generators, resulting in a larger electrical torque generated in all of the generators. Apart from the rotor angle stability issues discussed in previous paragraphs, if the mechanical torque driven by the prime movers/turbines cannot match the electrical torque in a sufficiently small amount of time, the imbalance in force will slow down the rotors of all generators, resulting in a decrease in frequency even if the rotor angles manage to stay close to each other. A change in frequency may affect customers, in particular to applications (e.g. consumer electronic, computer hardwares, and motor drives) which are sensitive to frequency. With automatic control equipments mostly installed in today's network and generators, e.g. frequency sensors and droop control devices, frequency will be maintained automatically via dynamically controlling the mechanical torque in a timely fashion.

An increase in load consumption also leads to an increase in voltage difference in the network. If the voltage controlling devices (e.g. synchronous generators/condensors) do not adjust the voltage set-points and reactive power in time, certain areas in the grid may fall below the minimum required voltage and creating a voltage stability problem. In the worse case if the voltage difference is too large, a voltage collapse [5] may occur resulting in a blackout and loss of loads. With excitation equipments mostly installed in today's generators and proper management of reactive generation reserves, voltages are maintained automatically in nowaday's power system network.

Suppose that the mechanical torque driven by the prime movers/turbines are now adjusted to match the increased electrical torque to restore the speed of the rotors. A steam turbine-generator rotor has a complex mechanical structure consisting of several predominant masses connected by shafts of finite stiffness [5]. When a rotor rotates, torsional oscillations may occur in between these different masses. These oscillations oscillate in the subsynchronous range [5] and may affect the power transmission system, e.g. affecting the excitation control equipments

and resulting in undesired subsynchronous resonance with transmission lines. Proper damping of torsional oscillations are required to avoid this type of instability.

In practice, many types of disturbances are expected to occur other than picking up industrial loads. These disturbances range from load/demand variations from the domestic/distribution grid, generator shutting down due to maintenance schedule, or dispatch changes driven by the energy market. These disturbances can usually be forecasted and known before the event occurs. In addition, power systems are also required to be reliable when unforeseeable events occur. In general, we expect a system remains stable when one of the transmission equipments is lost due to unforeseeable damage ($N-1$ contingency). Power system utilities will perform simulations for many of these scenarios to ensure the system is capable to handle the disturbances and remains stable.

2.2 Natural Gas Transmission System

This section introduces the natural gas transmission system. Similar to power transmission systems, we will introduce the terminologies and notations, and show the fundamental optimal gas flow problem.

2.2.1 Terminologies and notations

Similar to power transmission systems, a natural gas transmission system consists of three main parts: a) Natural gas sources/wells for natural gas supply, b) gas pipes and control components (e.g. gas compressors / gas valves) for natural gas transmission and control, and c) natural gas demands/loads for natural gas extraction.

To simplify our notations, we represent the natural gas transmission system as a directed graph $\mathscr{G} = (\mathscr{J}, \mathscr{P})$, where $\mathscr{J}$ is a set of nodes representing gas junction points $J_i \in \mathscr{J}$, and $\mathscr{P}$ is a set of gas pipes P_{ij} connecting gas junction points $i \in \mathscr{J}$ and $j \in \mathscr{J}$. To further simplify our notations, we implicitly model gas supplies, demands, and transporting hubs both as junction points/nodes in the network with positive, negative, and zero (net) gas flow respectively. The length of pipe P_{ij} is denoted by L_{ij}, its diameter by D_{ij}, and its cross-sectional area by A_{ij}. The dynamic state on the pipe P_{ij} at a location $x_{ij} \in [0, L_{ij}]$ and time $t \in [0, T]$ is given by pressure $p_{ij}(t,x)$ and mass flow $q_{ij}(t,x)$ functions. Table 2.3 lists the notations we use in this thesis for a natural gas network.

Example 2.2.1. Figure 2.6 shows the 24-pipe benchmark gas network system used by Zlotnik et. al [6]. The benchmark network consists of 24 gas pipes and 25 junctions, with 1 source, 16 transportation nodes, and 8 demand points. There are 5 compressors installed in the network, (marked as triangles) to boost the pressure of the system. Nodes, edges, and compressors are numbered and colorized with blue, black, and red colors respectively. Sources, transportation, and demand/consumer nodes are colored in red, blue, and green respectively. There are only two types of pipes in this network: 36 inch pipes and 25 inch pipes, which are represented as thick and thin lines. Since the benchmark is a tree network, gas naturally will be flowing from the only source node to the demand nodes, hence the flow direction of the pipe is determined.

Table 2.3: Nomenclature for natural gas system networks

Nomenclature for natural gas network $\mathcal{G} = (\mathcal{J}, \mathcal{P})$	
$\mathcal{J}$	Set of junctions in the gas network
$\mathcal{P}$	Set of gas pipes in the gas network
$\mathcal{C} \subseteq \mathcal{P}$	Subset of pipes in the network with compressors installed
J_i	Natural gas junction of node i
P_{ij}	Natural gas pipe of edge (i,j) connecting junction i and j
D_{ij}, A_{ij}, L_{ij}	Diameter (m), cross-section area (m^2), and length (m) of pipe P_{ij}
γ, η	Isentropic coefficient of gas and compressor efficiency factor
a, λ	Sound speed (ms^{-1}) and gas friction factor
p_i	Pressure variable (Pa) for junction J_i
p_{ij}	Pressure variable (Pa) for pipe P_{ij}
q_i	(Net) Mass flux variable (kg/s) for junction J_i
q_{ij}	Mass flux variable (kg/s) for pipe P_{ij}
p_N, q_N	Pressure and flux dimensionless scaling constants for dimensionless normalization
R_{ij}, c_{ij}	Compressor ratio and compressor location of pipe P_{ij}
d_i	Mass flux (kg/s) injections/consumptions at junction point J_i
s_i	Boundary pressure (Pa) at junction point J_i
S_{ij}	Cost of the compressor at $P_{ij} \in \mathcal{C}$
T	Total time horizon (sec) considered in the problem
$\overline{p_{ij}}, \underline{p_{ij}}$	Maximum/Minimum pressure limit (Pa)
$\overline{R_{ij}}, \underline{R_{ij}}$	Maximum/Minimum compression limit
$x_{ij} \in [0..L_{ij}]$	Space segment (in m or km) of pipe P_{ij}
$t \in [0..T]$	Time segment within the considered time horizon T
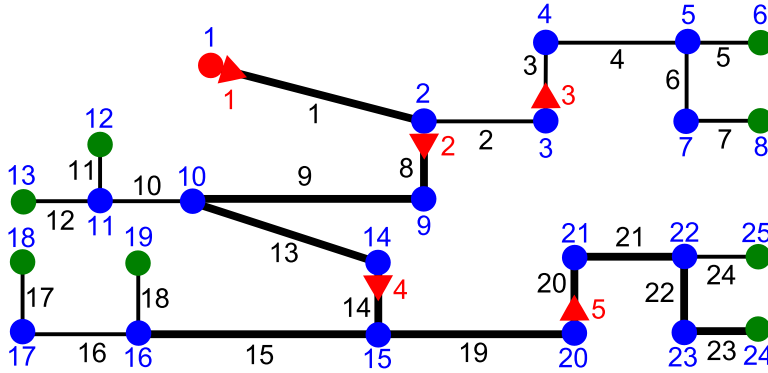
Figure 2.6: 24-pipe gas system test network used by Zlotnik et. al [6].

2.2.2 Isothermal gas flow equation

We are interested in the subsonic and isothermal regime where transients are sufficiently slow so as not to excite shocks or waves, i.e., where the flow velocity through a pipe is less than the speed of sound a in the gas, and temperature is assumed to be fairly constant.

We note that gas compression can be a major factor in changing the gas temperature in practice. Since nowadays gas pipes are buried underground, gas temperature will eventually be returned to the ground temperature within several kilometers after gas compression [78]. In

addition, the ground temperature variations are usually small (in the order of a few percents) and modern compressor stations may be further equipped with gas coolers. Therefore, we assume no large temperature differences occur.

We adopt the modeling assumptions outlined in the work of Osiadacz [79], which was validated and widely used by other studies on modeling gas pipeline networks for dynamic optimization [80, 11, 34]. Throughout the network, we omit higher order inertial terms, assume gas pipes are horizontal and ignore gravity effects, assume gas compositions and temperatures are uniform, and assume gas is compressible with a unique nominal gas compressibility factor. These assumptions will imply a uniform and constant speed of sound a throughout the system. Our primary focus is on the development and validation of dynamic optimization methodology instead of researching on new detailed physical models. Therefore, we focus to capture only the key physical phenomena of large-scale gas pipeline flows. We leave as future work for generalizations of our results to cases where temperature and gas composition are inhomogeneous, or an equation of state is required to determine gas compressibility.

In the literature, various forms of equations [81, 82, 6, 11] exist to describe the flow of natural gas within this regime. Most of these equations eventually are re-formulations/variants with various degrees of simplifications on the the homogenous compressible flow equations [81] considering the conservation of mass, linear momentum, and energy. In this thesis, we choose to use the isothermal flow equation from Herty et. al [11] to describe the flow dynamics on a single pipe P_{ij} in this regime as:

$$\frac{\partial p_{ij}}{\partial t} + \frac{a^2}{A_{ij}}\frac{\partial q_{ij}}{\partial x} = 0$$

$$\frac{1}{A_{ij}}p_{ij}\frac{\partial q_{ij}}{\partial t} + p_{ij}\frac{\partial p_{ij}}{\partial x} = -\frac{\lambda a^2}{2D_{ij}A_{ij}^2}q_{ij}|q_{ij}|,$$

Herty et. al further proposed to simplify the equations by approximating $\frac{\partial q_{ij}}{\partial t} \approx 0$ [11]. This gives the following partial differential equations (PDE) [11]:

$$\frac{\partial p_{ij}}{\partial t} + \frac{a^2}{A_{ij}}\frac{\partial q_{ij}}{\partial x} = 0 \tag{2.1}$$

$$2p_{ij}\frac{\partial p_{ij}}{\partial x} + \frac{\lambda a^2}{D_{ij}A_{ij}^2}q_{ij}|q_{ij}| = 0 \tag{2.2}$$

The second term in (2.2) approximates friction effects, which constitute the major phenomenon that dissipates momentum of the gas flow [79].

The gas dynamics on a pipeline segment are represented using (2.1)-(2.2) and possess a unique solution [11] when any two of the boundary conditions $p_{ij}(t,0)$, $q_{ij}(t,0)$, $p_{ij}(t,L_{ij})$, or $q_{ij}(t,L_{ij})$ are specified. For both computational and notational purposes, we apply a transformation to dimensionless variables [11] given by

$$\tilde{p}_{ij} = \frac{p_{ij}}{p_N}, \qquad \tilde{q}_{ij} = \frac{q_{ij}}{q_N}, \qquad \tilde{x}_{ij} = x\frac{\lambda a^2 q_N^2}{D_{ij}A_{ij}^2 p_N^2}, \qquad \tilde{t}_{ij} = t\frac{\lambda a^4 q_N^3}{D_{ij}A_{ij}^3 p_N^3}, \tag{2.3}$$

where p_N and q_N are scaling constants. This results in the dimensionless equations [11]

$$\frac{\partial \tilde{p}_{ij}}{\partial \tilde{t}_{ij}} + \frac{\partial \tilde{q}_{ij}}{\partial \tilde{x}_{ij}} = 0, \tag{2.4}$$

$$2\tilde{p}_{ij}\frac{\partial \tilde{p}_{ij}}{\partial \tilde{x}_{ij}} + \tilde{q}_{ij}|\tilde{q}_{ij}| = 0, \tag{2.5}$$

Note that the space and time variables $\tilde{x}_{ij}$ and $\tilde{t}_{ij}$ are now pipe-dependent.

2.2.3 Compressor mechanics

Due to momentum dissipation (friction term) in (2.2), the transport of natural gas comes with pressure loss, proportional to the distance separating between the source and the destination. To meet security requirements in large transmission systems, compressors must be used to boost the pressure at some of the pipes/junctions. In this thesis, we assume the action of compressors is modeled as a conservation of flow and an increase in pressure at a point $c_{ij} \in [0, L_{ij}]$ by a multiplicative ratio $R_{ij}(\tilde{t}_{ij}) \geq 1$ [6]. We have the following assumptions:

$$\lim_{\tilde{x}_{ij} \searrow c_{ij}} \tilde{p}_{ij}(\tilde{t}_{ij}, \tilde{x}_{ij}) = R_{ij}(\tilde{t}_{ij}) \lim_{\tilde{x}_{ij} \nearrow c_{ij}} \tilde{p}_{ij}(\tilde{t}_{ij}, \tilde{x}_{ij}),$$

$$\lim_{\tilde{x}_{ij} \searrow c_{ij}} \tilde{q}_{ij}(\tilde{t}_{ij}, \tilde{x}_{ij}) = \lim_{\tilde{x}_{ij} \nearrow c_{ij}} \tilde{q}_{ij}(\tilde{t}_{ij}, \tilde{x}_{ij}).$$

The cost of compression S_{ij} is proportional to the required power [83], and is approximated by

$$S_{ij}(\tilde{t}_{ij}) = \eta^{-1}|\tilde{q}_{ij}(\tilde{t}_{ij}, c_{ij})|(\max\{R_{ij}(\tilde{t}_{ij}), 1\}^{2K} - 1)$$

over time $\tilde{t}_{ij}$ at spatial point c_{ij}, with $0 < K = (\gamma - 1)/\gamma < 1$, where γ is the heat capacity ratio and η is a compressor efficiency factor.

Modeling discussion A compression ratio with a value greater than 1, i.e., $R_{ij}(\tilde{t}_{ij}) \geq 1$, corresponds to a compressor applying power in its defined working direction. A value of $R_{ij}(\tilde{t}_{ij}) = 1$ denotes a compressor that is bypassed by the flow, in either the working or the reverse direction. For modeling flows in large-scale systems, we use theoretical compressors that represent entire compressor stations as single objects. For transmission pipelines, flow to all machinery in the station is accepted and discharged through common headers. The detailed control mechanisms of individual compressors are abstracted, and individual compressors are coordinated by the control system of the station to maintain operating setpoints corresponding to the common headers. This abstract representation of actuators that boost pressure can also be used to model pressure regulators that decrease the pressure where needed. However, large-scale transmission pipelines typically include few such elements, because regulation is often performed to lower pressure at city gates or large customers after custody is transferred from the pipeline.

  This study does not model regulators and imposes certain assumptions on the structure of the system and the pressure bounds. We assume that the pipeline system was built in order to admit feasible solutions in its usual operations. Specifically, since pressure cannot be actively

decreased in our model (in accordance with the typical construction of transmission pipelines), we assume that the maximum pressure bound throughout the network is uniform. While this may appear to be a strong assumption, it is reasonable in practice as: 1) the intra-day operation of high-pressure, large-scale transmission systems is separated from operation of lower pressure distribution systems, and 2) transmission systems rarely experience changes in large-scale flow directions.

This assumption guarantees that R_{ij} must be assigned to 1 (set to bypass mode) in the optimal solution if gas is delivered in the reverse direction (from j to i) on a pipe P_{ij} with compressor C_{ij}. Assume that R_{ij} is larger than 1 (i.e., set to regulator mode in the reverse flow direction) in an optimal solution. Since the maximum pressure bound is uniform across the network, it is possible to remove the decompression and obtain a feasible solution with a lower cost based on our objective function, contradicting the optimality assumption.

Proof. We show the sketch of the proof by a contradicting example. Suppose the optimal solution assigns any values larger than 1 to R_{ij} (i.e., set to regulator mode in the reverse flow direction). In this situation, the compressor energy objective function S_{ij} for that compressor will be larger than 0 (for a certain period of time $\tilde{t}_{ij}$). This implies the compressor is actively decreasing pressure in the direction of flow (a reverse flow in this situation). If using the compressor C_{ij} to decrease pressure in the reverse direction is a feasible solution, a solution not using the compressor to decrease pressure (e.g. set to bypass with R_{ij} assigned to zero) is also feasible, if our assumption that the maximum pressure bound is uniform throughout the pipe/system holds. Assigning R_{ij} to zero will give a smaller objective value than $R_{ij} > 0$. This contradicts the hypothesis of optimality for $R_{ij} > 0$.   □

The investigation of appropriate models and optimal control problems for systems with more complex structure, such as multi-pressure systems that require intra-day control of regulators, is a topic for future research.

2.2.4 Steady-state Gas Flow Equations (Steady GFP)

The dynamic gas equations ((2.4) - (2.5)) are partial differential equations, which are difficult to directly incorporate into optimization problems. In the literature, a steady state equivalent is common [26, 27, 84, 85, 82, 86, 87]. We will now introduce the steady state equations based on Herty et.al [11]. For a system to be steady, we require the pressure at every spatial location in the pipe remains constant over time for all spatial point $\tilde{x}_{ij}$:

$$\frac{\partial \tilde{p}_{ij}}{\partial \tilde{t}_{ij}} = 0$$

(2.4) will be reduced to:

$$\frac{\partial \tilde{q}_{ij}}{\partial \tilde{x}_{ij}} = 0$$

Given an arbitrary time step $\tilde{t}_{ij}$, the reduced equation implies the mass flux at every spatial location within a single pipe should be the same. Therefore at every time step $\tilde{t}_{ij}$, (2.5) can be

simplified as:

$$2\tilde{p}_{ij}\frac{\partial \tilde{p}_{ij}}{\partial \tilde{x}_{ij}} = \mathbb{K}$$

where $\mathbb{K}$ can be viewed as a function of $\tilde{q}_{ij}$. By viewing $\tilde{p}_{ij}$ as a function of time $\tilde{t}_{ij}$ and space $\tilde{x}_{ij}$ and using the chain rule, we can obtain:

$$2\tilde{p}_{ij}\frac{\partial \tilde{p}_{ij}}{\partial \tilde{x}_{ij}} = \frac{\partial(\tilde{p}_{ij}^2)}{\partial \tilde{x}_{ij}} = \mathbb{K} = -\tilde{q}_{ij}|\tilde{q}_{ij}| \quad \text{(dimensionless form)}$$

and similarly for the original equation:

$$2p_{ij}\frac{\partial p_{ij}}{\partial x} = \frac{\partial(p_{ij}^2)}{\partial x} = \mathbb{K} = -\frac{\lambda a^2}{D_{ij}A_{ij}^2}q_{ij}|q_{ij}| \quad \text{(original form)}$$

This implies the square of the pressure in the pipe changes uniformly across space subject to a function of the flux $\tilde{q}_{ij}$. For a steady system, if the flux is known, $\mathbb{K}$ can be determined. If the boundary pressure of the pipe is given, we can then determine and compute the pressure values for all the other spatial points. Suppose we now integrate the equation w.r.t. space x from junction point i to point j:

$$\int_0^{\tilde{L}_{ij}} \frac{\partial(\tilde{p}_{ij}^2)}{\partial \tilde{x}_{ij}}d\tilde{x}_{ij} = \int_0^{\tilde{L}_{ij}} \mathbb{K}\,d\tilde{x}_{ij}$$

We will obtain the steady-state gas flow equation for the dimensionless form:

$$\tilde{p}_i^2 - \tilde{p}_j^2 = \tilde{L}_{ij}\tilde{q}_{ij}|\tilde{q}_{ij}| \tag{2.6}$$

and similarly the following for the original form:

$$p_i^2 - p_j^2 = L_{ij}\frac{\lambda a^2}{D_{ij}A_{ij}^2}q_{ij}|q_{ij}| \tag{2.7}$$

where $p_i/\tilde{p}_i$ and $p_j/\tilde{p}_j$ are the pressure/dimensionless pressure at junction point i and j respectively. The above equations eventually link the pressure (squared) difference at the two ends of a pipe to the steady-state gas/flux flow as well as the pipe and gas characteristics. In steady states, we can even further simplify and assume the compressor is installed in one end of the pipe. Suppose the compressor is installed at node i, we will then have the following generalized steady-state gas flow equation in original form:

$$R_{ij}^2 p_i^2 - p_j^2 = L_{ij}\frac{\lambda a^2}{D_{ij}A_{ij}^2}q_{ij}|q_{ij}| \tag{2.8}$$

with the following simplified cost function

$$S_{ij} = \eta^{-1}|q_{ij}|(\max\{R_{ij},1\}^{2K} - 1) \tag{2.9}$$

Model 5 shows the Optimal Gas Flow Problem (OGFP) by using the steady-state equations (original form). Our goal is to optimize the compression costs S_{ij}, while still satisfying the gas demands and the pressure/flux operational ranges. This model will find pressure values p_i at every pipe junctions, gas flows q_{ij} for every pipes, gas dispatches $q_i, J_i \in \mathscr{J}^S$ for gas suppliers, compression ratios R_{ij} for compressors, and the optimized compression cost S_{ij} to operate the network. Objective (O1) models the steady state compression cost function. The flow balance equation is implemented by (C2.1). Constraint (C2.2) ensures the net flow is zero for transportation nodes. Constraint (C2.3) ensures the net flow is the same as the demand for demand nodes. The steady-state gas flow equations are implemented in (C3.1)-(C3.2). Finally, (C4.1) implements the cost functions.

Model 5 Optimal Gas Flow Problem: Compressor Optimization

Inputs:

$\mathscr{G} = (\mathscr{J}, \mathscr{P})$	Natural gas transmission system
$\mathscr{J}^T, \mathscr{J}^D, \mathscr{J}^S$	Subset of transport, demand, and supply nodes/junctions
$\mathscr{C}$	Subset of pipes with compressors

Variables:

$p_i \in (\underline{p_i}, \overline{p_i}), \forall J_i \in \mathscr{J}$	Pressure variables for J_i
$q_i \in (\underline{q_i}, \overline{q_i}), \forall J_i \in \mathscr{J}$	(Net) flux variables for J_i
$q_{ij} \in (\underline{q_{ij}}, \overline{q_{ij}}), \forall P_{ij} \in \mathscr{P}$	Flux variables for P_{ij}
$S_{ij}, \forall P_{ij} \in \mathscr{C}$	Cost variables representing compression costs
$R_{ij}, \forall P_{ij} \in \mathscr{C}$	Compression ratio for the compressor at P_{ij}

Minimize

$$\sum_{P_{ij} \in \mathscr{C}} S_{ij} \tag{O1}$$

Subject to:

$$\sum_{j \in \mathscr{J} : J_{ij} \in \mathscr{P}} q_{ij} - \sum_{j \in \mathscr{J} : J_{ji} \in \mathscr{P}} q_{ji} = q_i \qquad \forall i \in \mathscr{J} \tag{C2.1}$$

$$q_i = 0 \qquad \forall J_i \in \mathscr{J}^T \tag{C2.2}$$

$$q_i = d_i \qquad \forall J_i \in \mathscr{J}^D \tag{C2.3}$$

$$R_{ij}^2 p_i^2 - p_j^2 = L_{ij} \frac{\lambda a^2}{D_{ij} A_{ij}^2} q_{ij} |q_{ij}| \qquad \forall P_{ij} \in \mathscr{C} \tag{C3.1}$$

$$p_i^2 - p_j^2 = L_{ij} \frac{\lambda a^2}{D_{ij} A_{ij}^2} q_{ij} |q_{ij}| \qquad \forall P_{ij} \in \mathscr{P} - \mathscr{C} \tag{C3.2}$$

$$S_{ij} = \eta^{-1} |q_{ij}| (\max\{R_{ij}, 1\}^{2K} - 1) \qquad \forall P_{ij} \in \mathscr{C} \tag{C4.1}$$

An Indirect Stability Approach on Power Systems Restoration

This chapter introduces our first contribution in maintaining system stability. In this chapter, we consider the restoration of a power transmission system after a significant disruption such as a natural disaster. The problem at hand is Restoration Ordering Problem (ROP) that jointly considers generator dispatch, load pickups, and restoration prioritization to minimize the size of the blackout while satisfying the network operational constraints. We examine transient effects in power restoration and generalize the ROP formulation with standing phase angle and voltage difference constraints. These constraints are generally classified as indirect approaches to enhance rotor angle stabilities. We perform experiments on various benchmarks to show the novel ROP-SPASVD formulation reduces rotor swings of synchronous generators by over 50%, while having a negligible impact in restoration delay, in terms of blackout size in less than 1.5% increases, which is still optimized holistically.

3.1 Overview

Restoring a transmission system after a significant disruption, e.g., a cascading voltage collapse or a natural disaster, is an important task with consequences on both human and economic welfare. However, restoration plans are very challenging to design: Planners aim at minimizing the blackout period but also must prioritize repairs (i.e., determine the order in which to energize lines), load pickups, and generator dispatch without violating static network constraints (e.g., line thermal limits) and creating significant transient effects (e.g., large rotor swings).

This chapter is part of a long-term research project [88, 45, 24, 89] to develop holistic power restoration algorithms for responding to significant network disruptions, such as those stemming from natural disasters. Past research has isolated a key sub-problem in power systems restoration, the Restoration Ordering Problem (ROP) [24], which formalizes the process of prioritizing network repairs, re-dispatching generations, and picking up new loads to minimize the blackout period. The ROP determines the best sequence of steady states, each state associated with a restoration action. It raises significant computational challenges: Since no *typical* operating point is known for the damaged network, even determining a sequence of steady states that satisfy the AC power flow equations is a non-trivial endeavor and the popular DC power flow approximation cannot be used in this context [89]. To remedy this limita-
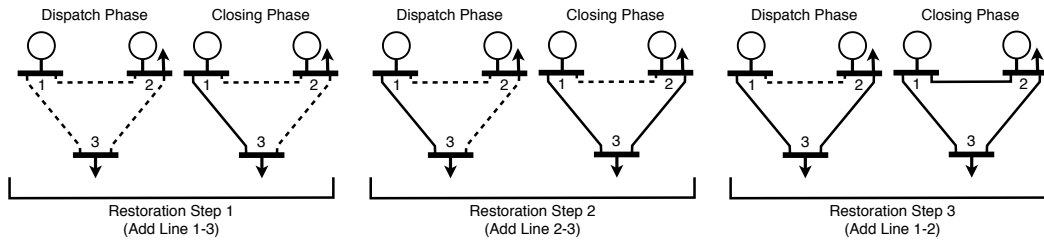
Figure 3.1: The Two Phases of the Restoration Ordering Algorithm.

tion, prior and existing work introduced and use the LPAC model to obtain a more accurate approximation to the AC power flow equations [90, 89].

3.2   Our Main Contribution

Prior work on the ROP problem restricts attention to determining an optimal sequence of AC-feasible steady-states: It did not consider whether the power systems can transition from each steady-state to the next. This is an important issue since, in a restoration context, the power network is operating far from its original design specification and many topology changes are occurring. This work is a first step in addressing transient effects during the computation of high-quality restoration plans for the ROP problem. Inspired by field practices [16, 15, 20, 19, 18], it proposes an enhanced formulation of the ROP to mitigate dynamic rotor swings (one of many possible transient effects to consider) ***by imposing standing phase angle (SPA) and voltage difference (SVD) constraints***. The formulation splits each restoration action into two steps as illustrated in Figure 3.1: *A dispatch step* where the generation dispatch and load pickups are adjusted to meet the SPA and SVD constraints and *a closing step* where the repaired component is energized. The resulting formulation is called the ROP-SPASVD formulation. The benefits of the ROP-SPASVD formulation are evaluated using the commercial transient simulator Power World [7, 91] and five MatPower test systems [92]. The key findings can be summarized as follows: (1) The DC power flow approximation is not appropriate for solving the ROP-SPASVD, while the LPAC model has the required accuracy. (2) SPA and SVD constraints can reduce rotor swings of synchronous generators by over 50%. (3) By jointly considering SPA and SVD constraints with load pickups and generation dispaches, improvements in rotor swings have negligible impacts on the blackout size (i.e., $\leq 1.5\%$ increase), which is optimized holistically.

Section 3.3 introduces our prior and related work on this problem. Section 3.4 shows the dynamic models and configurations we used for simulations on the commercial PowerWorld simulator. Section 3.5 introduces the 3-bus case study which illustrates the benefits of the SPA and SVD constraints. Section 3.6 shows our novel ROP-SPASVD model. Section 3.7 gives experimental evaluations on 5 MatPower benchmark systems.

3.3   Prior and Related Work

SPA constraints have been proposed before to improve rotor stability. Most of the work on SPA constraints [20, 19, 18] focuses on methods and algorithms to minimize the standing

phase angle for restoring one selected transmission line only. Ye and Liu [18] allow unserved load to be picked up during the restoration as a control strategy to minimize the SPA, which is natural in power restoration [24]. They also use the AC non-linear power flow equations. In contrast, this research considers the restoration prioritization globally and imposes SPA constraints for the damaged lines over the course of the restoration. The rotor swings are analyzed globally over the entire restoration process. This research also uses the LPAC model [90] to approximate the power flow equations, which allows the entire restoration process to be expressed as a mixed-integer linear program, which is more tractable than a mixed integer non-linear program. We also show that SPA constraints may not be sufficient in reducing rotor swings for certain benchmarks, and further consider SVD constraints to remedy this limitation.

3.4 Transient Modeling on PowerWorld simulator

This work adopts the classical model of generator dynamics combined with the following Swing equation [5] for evaluating the experimental results of our work:

$$\frac{2H}{\omega^0}\frac{d^2\delta}{dt^2} = p_m - p_e - D\omega$$

where H, δ, D, ω, and ω^0 are the inertia constant, the rotor angle, the damping coefficient, the current angular velocity, and the nominal angular velocity of a synchronous machine. On the right hand side, p_m and p_e are the mechanical and electrical power acting on the rotor of the generator. The circuit of the classical model of a generator is shown in Figure 3.2. E_{fd}
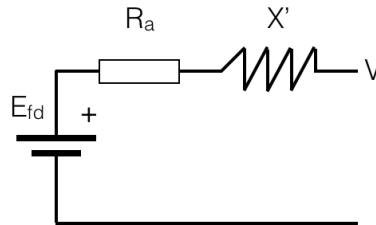
Figure 3.2: Circuit diagram of classical generator model

represents the constant (field) voltage supplied by the generator, and V represents the terminal voltage of generator (i.e., the voltage of the terminal bus). R_a and $X^{'}$ are the armature resistance and the transient reactance of the generator. By using V, E_{fd}, R_a, and $X^{'}$ following the circuit diagram, we could compute p_e. The paper also uses the PTI IEEE dynamic load model [93] when performing simulations. The load model changes the active and reactive power of the load depending on the voltage and frequencies shown in the following equation:

$$p'_l = p_l[a_1(\frac{V_l}{V_0})^{n_1} + a_2(\frac{V_l}{V_0})^{n_2} + a_3(\frac{V_l}{V_0})^{n_3}][1 + a_7\Delta f]$$

$$q'_l = q_l[a_4(\frac{V_l}{V_0})^{n_4} + a_5(\frac{V_l}{V_0})^{n_5} + a_6(\frac{V_l}{V_0})^{n_6}][1 + a_8\Delta f]$$
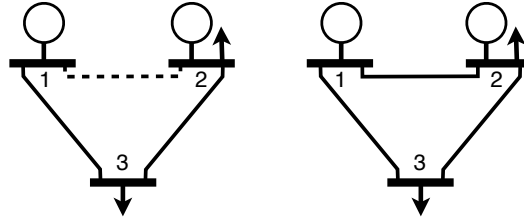
Figure 3.3: Topology Change Example: Open State (left), Closed State (right).

Table 3.1: Line, Load, and Generator Model Parameters

Line	r (p.u.)	x (p.u.)	b (p.u.)
1 to 2	0.01938	0.05917	0.00000
1 to 3	0.05403	0.22304	0.00000
2 to 3	0.05695	0.17388	0.00000

Load	p_l (MW)	q_l (MVar)
Bus 2	100.00	0.00
Bus 3	100.00	0.00

Generator	H (MW/MVA · sec)	D (p.u.)	R_a (p.u.)	X' (p.u.)
Gen 1	30.00	5.00	0.02	0.20
Gen 2	30.00	5.00	0.02	0.20

where p_l and q_l are the amount of active and reactive power served at steady state and p'_l and q'_l are the resulting active and reactive power demand. V_l and V_0 are the voltage of the bus the load is currently connected to and the nominal voltage of the system. Δf is the change in frequency of the power network. All variables a_i ($i \in \{1..8\}$) and n_j ($j \in \{1..6\}$) are configurable constants.

3.5 Topology Changes and Rotor Swings

To build the intuition behind the ROP-SPASVD model, consider the 3-bus network in Figure 3.3 and its parameters in Tables 3.1. This 3-bus example is in fact a sub-graph of the IEEE 14 standard test case. This section conducts two studies on this network: (1) a restoration topology change (i.e., adding line 1–2); and (2) a congestion removing topology change (i.e., removing line 1–2). The effects of the topology change are evaluated on five scenarios, each of which corresponds to a different generator dispatch that meets the load.

Table 3.2: Restoration Case: Settings

Case	Bus 1 Volt.(kV)	Bus 2 Volt.(kV)	Bus 1 Ang.(deg)	Bus 2 Ang.(deg)	Gen 1 Pow. (MW/MVar)	Gen 2 Pow. (MW/MVar)	1st Swing (deg)
1	146.28	97.24	0.00	-47.58	221.12/143.46	20.00/18.00	44.229
2	146.28	146.28	0.00	-35.33	207.42/28.05	20.00/78.32	31.249
3	146.28	141.725	0.00	-12.14	102.59/10.66	102.59/10.66	10.385
4	146.28	123.84	0.00	0.00	61.05/48.08	143.85/-30.00	0.619
5	146.28	146.28	0.00	0.00	45.37/6.10	157.31/3.16	0.002

Table 3.3: Removal Case: Settings

Case	Bus 1 Volt.(kV)	Bus 2 Volt.(kV)	Bus 1 Ang.(deg)	Bus 2 Ang.(deg)	Gen 1 Power (MW/MVar)	Gen 2 Power (MW/MVar)	1st Swing (deg)
1	146.28	142.36	0.00	-4.23	206.27/20.88	0.00/0.63	>90(unstable)
2	146.28	146.28	0.00	-4.62	206.48/-36.62	0.00/58.70	>90(unstable)
3	146.28	145.22	0.00	-1.50	101.53/5.40	101.53/5.40	10.276
4	146.28	143.01	0.00	0.00	60.06/50.59	143.00/-40.00	0.137
5	146.28	146.28	0.00	0.00	45.28/6.13	157.40/3.13	0.016

Scenario 5 is a dispatch that produces the same bus phase angles and voltage magnitudes for the generator buses. Scenario 2 (resp. 4) is a dispatch where the voltage magnitudes (resp. the bus phase angles) are the same for the generator buses. Scenario 3 has the same dispatch for both generator. Scenario 1 is a dispatch with no specific constraint. In this study, a swing of more than 90 degrees is unacceptable and should lead to self-protection measures [5].
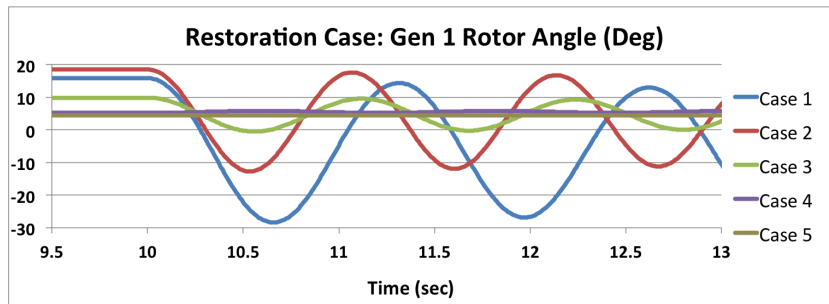
Figure 3.4: Restoration Case: Generator 1 Rotor Angle (deg)
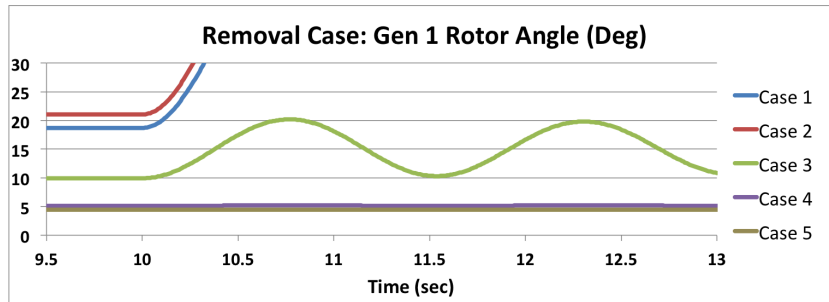
Figure 3.5: Removal Case: Generator 1 Rotor Angle (deg)

In restoration, the network starts in the open state (Figure 3.3 - left) and, after 10 seconds, the line breaker is closed (Figure 3.3 - right). The last column of Table 3.2 reports the magnitude/amplitude of the first rotor swing of generator 1 for each of the five scenario. The results show that, as standing phase angle differences increase, so do the swings. Figure 3.4 depicts the rotor angles of generator 1 for the scenarios. The figure clearly shows that the swing increases drastically with large phase angle differences. Hence, it is obviously desirable to select

generator dispatch with small angle differences in power restoration. In line switching/opening scenarios, the network starts in the closed state (Figure 3.3 - right) and, after 10 seconds, the line breaker is opened. Table 3.3 and Figure 3.5 present the results. The results are similar to the restoration case but more extreme. In particular, the first two scenarios lead to instabilities in the network, while smaller SPAs and SVDs reduce the rotor swing and achieve stability.

3.6   Power Restoration Ordering Problem with Standing Phase Angle Constraints

Section 3.5 confirmed standard field practices [16, 15, 20, 19, 18], and suggests to enhance the ROP formulation in [24] with SPA and SVD constraints in order to mitigate rotor swings. The ROP-SPASVD includes two extensions. First, we extend the model to incorporate AC power flow equations, primarily for accuracy reasons and the capability to handle reactive power and voltage accurately (see also the reasons stated in [89]). Second, to incorporate the effects of SPA constraints, each restoration step must be broken into two phases: A *dispatch* phase *d* and a *closing* phase *c*. The goal of the dispatch phase is to re-dispatch the generators to satisfy the SPA and SVD constraints for the repaired line. The closing phase adds the repaired line to the network and ensures that all operational constraints are satisfied. The closing phase enforces the generator dispatch selected in the dispatch phase.

   A complete model for the AC-ROP-SPASVD is presented in Model 6. The model assumes the components of the network will be energized one at a time and will remain energized for the remainder of the restoration process. The restoration is modeled as $2|\mathscr{R}|$ steady states, with one dispatch phase and one closing phase for each of the $|\mathscr{R}|$ restoration actions. Note that each measure (e.g., real power on a line (n,m)) is associated with $2|\mathscr{R}|$ variables, one for each restoration step r and phase p. As the input data and variables of the AC-ROP-SPA are described in Model 6 in detail, only the constraints are discussed. The objective (O.1) strives to reducing the size of the blackout and thus to serve as much active power as possible through the restoration process. Constraints (C.1.x) are concerned with the operational state of the components in the network. Constraint (C.1.1) ensures all non-damaged components are active, while Constraint (C.1.2) ensures components not selected for repair remain inactive. Constraint (C.1.3) activates one component in each time step, and Constraint (C.1.4) ensures components remain active in future time steps. Constraints (C.1.5)–(C.1.7) capture the operational state of the components. A component is only operational after it and all of its dependent parts are active. Constraints (C.2.x) model the AC power flow equations and link them with the operational state of the network. Constraint (C.2.1) selects a slack bus. Constraints (C.2.2)–(C.2.3) model Kirchhoff's Current Law and Constraints (C.2.4)–(C.2.5) capture the flow of power by Ohm's Law. Constraint (C.2.6) captures the line thermal limits. Constraints (C.2.7)–(C.2.9) link the operational state of the generators and loads to the power flow variables. Finally, Constraints (C.3.x) model the constraints between simulation phases. Constraints (C.3.1)–(C.3.2) fix the generator dispatch between the phases. Constrain (C.SPA) implements a standing phase angle constraint of less then θ^Δ when a line is closed in step r, while Constraint (C.SVD) implements a similar voltage difference constraint. The AC-ROP-SPASVD jointly considers generator dispatch, load pickups, topology changes, restoration pri-

---

Model 6 The ROP with SPA and SVD Constraints

Inputs:

$\mathscr{P} = \langle N, L, G, O \rangle$ -Power network

$A = N \cup L \cup G \cup O$ -The global set of equipments

$\mathscr{D}, \mathscr{R} \subseteq \mathscr{D}$ -Damaged items, and items considered to be restored

$s \in N$ -Slack bus

Variables: (Step (r,p): $0 \le r \le |\mathscr{R}|, p \in \{d,c\}$)

$h^n(r) \in \{0,1\}, \forall n \in A$ - Item n is going to be repaired (or not) at step r

$k^n(r) \in \{0,1\}, \forall n \in A$ - Item n is operational (or not) at step r

$\theta^n(r,p) \in (-\pi, \pi), \forall n \in N$ - Bus phase angle at step (r,p) for bus n

$V^n(r,p) \in (\underline{V}^n, \overline{V}^n), \forall n \in N$ - Bus voltage at step (r,p) for bus n

$l^n(r,p) \in (0,1), \forall n \in O$ - Load precent for load n at step (r,p)

$p_g^n(r,p) \in (0, \overline{p}_g^n), \forall n \in G$ - Active injection of generator n at step (r,p)

$q_g^n(r,p) \in (\underline{q}_g^n, \overline{q}_g^n), \forall n \in G$ - Reactive injection of generator n at step (r,p)

$p^{nm}(r,p) \in (-\overline{p^{nm}}, \overline{p^{nm}}), \forall (l:n,m) \in L$ - Active flow on line $l : (n,m)$

$q^{nm}(r,p) \in (-\overline{q^{nm}}, \overline{q^{nm}}), \forall (l:n,m) \in L$ - Reactive flow on line $l : (n,m)$

Maximize

$$\sum_{r=0}^{|\mathscr{R}|} \sum_{p \in \{d,c\}} \sum_{n \in O} \overline{p}_l^n l^n(r,p) \tag{O.1}$$

Subject to: (Step (r,p): $0 \le r \le |\mathscr{R}|, p \in \{d,c\}$)

$$h^n(r) = 1, \qquad\qquad \forall n \in A \backslash \mathscr{D} \tag{C.1.1}$$

$$h^n(r) = 0, \qquad\qquad \forall n \in \mathscr{D} \backslash \mathscr{R} \tag{C.1.2}$$

$$\sum_{n \in \mathscr{D}} h^n(r) = r, \tag{C.1.3}$$

$$h^n(r-1) \le h^n(r), \qquad\qquad \forall n \in \mathscr{D}, r \ne 0 \tag{C.1.4}$$

$$k^n(r) = h^n(r), \qquad\qquad \forall n \in N \tag{C.1.5}$$

$$k^m(r) = h^m(r) \wedge h^n(r), \qquad\qquad \forall n \in N, \forall m \in G(n) \cup D(n) \tag{C.1.6}$$

$$k^l(r) = h^l(r) \wedge h^n(r) \wedge h^m(r), \qquad\qquad \forall (l:n,m) \in L \tag{C.1.7}$$

$$\theta^s(r,p) = 0 \tag{C.2.1}$$

$\forall n \in N :$

$$\sum_{m \in G(n)} p_g^m(r,p) - \sum_{m \in O(n)} \overline{p_l^m} l^m(r,p) = \sum_{m \in N(n)} p^{nm}(r,p) \tag{C.2.2}$$

$$\sum_{m \in G(n)} q_g^m(r,p) - \sum_{m \in O(n)} \overline{q_l^m} l^m(r,p) = \sum_{m \in N(n)} q^{nm}(r,p) \tag{C.2.3}$$

$\forall (l:n,m) \in L :$

$$p^{nm}(r,p) = k^l(r)(g^{nm}[V^n(r,p)]^2 - V^n(r,p)V^m(r,p)$$
$$(g^{nm}\cos(\theta^n(r,p) - \theta^m(r,p)) - b^{nm}\sin(\theta^n(r,p) - \theta^m(r,p)))) \tag{C2.4}$$

$$q^{nm}(r,p) = k^l(r)(-b^{nm}[V^n(r,p)]^2 - V^n(r,p)V^m(r,p)$$
$$(g^{nm}\sin(\theta^n(r,p) - \theta^m(r,p)) - b^{nm}\cos(\theta^n(r,p) - \theta^m(r,p)))) \tag{C2.5}$$

$$[p^{nm}(r,p)]^2 + [q^{nm}(r,p)]^2 \le \overline{S}^l k^l(r) \tag{C.2.6}$$

$$\neg k^n(r) \rightarrow p_g^n(r,p) = 0, \qquad\qquad \forall n \in G \tag{C.2.7}$$

$$\neg k^n(r) \rightarrow q_g^n(r,p) = 0, \qquad\qquad \forall n \in G \tag{C.2.8}$$

$$\neg k^n(r) \rightarrow l^n(r,p) = 0, \qquad\qquad \forall n \in O \tag{C.2.9}$$

$$p_g^n(r,d) = p_g^n((r-1),c), \qquad\qquad \forall n \in G, r \ne 0 \tag{C.3.1}$$

$$q_g^n(r,d) = q_g^n((r-1),c), \qquad\qquad \forall n \in G, r \ne 0 \tag{C.3.2}$$

$$k^l(r) \wedge \neg k^l(r-1) \rightarrow |\theta^n(r,d) - \theta^m(r,d)| \le \theta^\Delta, \quad \forall (l:n,m) \in L, r \ne 0 \tag{C.SPA}$$

$$k^l(r) \wedge \neg k^l(r-1) \rightarrow |V^n(r,d) - V^m(r,d)| \le V^\Delta, \quad \forall \langle l:n,m \rangle \in L, r \ne 0 \tag{C.SVD}$$

Table 3.4: Blackout Size and Convergence Rate for the DC-ROP-SPA.

θ^Δ Deg	6 Bus (Complete Search)		14 Bus (2 hr Limited Search)	
	Blackout (%)	# Failed / Total	Blackout (%)	# Failed / Total
180	12.55	3 / 6	5.35	2 / 7
10	12.55	1 / 6	5.35	2 / 7
5	12.55	2 / 6	5.35	1 / 7
2.5	12.55	2 / 6	5.35	1 / 7
1.25	12.55	1 / 6	5.35	2 / 7

oritization and the network operation limits. It also uses SPA and SVD constraints to improve transient stability in generator dynamics model.

The AC-ROP-SPA is a challenging mixed-integer non-linear non-convex program (non-convex MINLP) which is outside the scope of modern global optimization tools. To address its computational challenges of solving the AC-ROP-SPA globally, a natural avenue is to approximate the power flow equations. For instance, the AC-ROP was approximated with the popular DC power flow model in [24], resulting in a mixed-integer program (MIP) formulation which exploits mature industrial tools. Unfortunately, a DC-ROP-SPA approximation of the AC-ROP-SPA produces restoration plans riddled with problems. First, the DC solutions to the power flow equations could not be converted to AC solutions, verified by Power World simulator. Second, even if the solution did converged to an AC solution in Power World, the SPA constraints did not reduce rotor swings. Third, DC power flow approximation eliminate voltages, and hence SVD constraints cannot be expressed in the DC model. These observations, which are consistent with prior work in power restoration [89, 18, 19], are illustrated in Table 3.4. The table gives the SPA limit, the size of the blackout in percentage, and the number of line closing during restorations a DC plan cannot be converted into an AC plan for the 6 bus and the 14 bus case studies. Observe that the backout area does not change as the SPA constraints become tighter, highlighting again that the DC model is not accurate enough to reason on the bus phase angles in a restoration context.

To remedy these issues, our work use the LPAC model [90] to model the power flow equation as suggested in [89]. The LPAC model approximates the AC power flow with a linear program, captures reactive and volatge magnitudes, and is derived from the following assumptions: (1) $\sin(\theta^n - \theta^m) \approx \theta^n - \theta^m$; (2) the voltage magnitude at each bus is expressed as a deviation from a nominal operating voltage, i.e., $|\widetilde{V}| = |\widetilde{V}^t| + \phi$; (3) the non-convex cosine function is replaced with a polyhedral relaxation denoted by $\widehat{\cos}^{nm}$; (4) the remaining non-linear terms are factored and approximated with a first-order Taylor expansion. The LPAC model (cold-start version) yield the following power flow equations:

$$p^{nm} = g^{nm} - g^{nm}\widehat{\cos}^{nm} - b^{nm}(\theta^n - \theta^m)$$
$$q^{nm} = -b^{nm} + b^{nm}\widehat{\cos}^{nm} - g^{nm}(\theta^n - \theta^m) - b^{nm}(\phi^n - \phi^m)$$

This work uses the warm-start LPAC model, a slightly more advanced formulation that exploits the target voltage magnitudes for more accuracy [90]. The resulting LPAC-ROP-SPA formulation is also a MIP model which remedies the limitations of the DC power flow and is

sufficiently accurate to study the AC-ROP-SPA. The LPAC-ROP-SPA formulation is still very challenging computationally even for small networks (e.g., with more than 40 lines), since it holistically sequences the repairs. Since the LPAC model is an approximation of the AC model, power flow simulations are still required to validate the feasibility of the flow in practice, to ensure the computed decisions will not violate any security/operational constraints.

A randomized adaptive decomposition (RAD) [94, 95] procedure was proposed in [96] for solving similarly challenging ROP problems. The algorithm begins with an arbitrary restoration prioritization as a starting point. It then inspects contiguous subsections of the restoration steps randomly and replaces them with improved subsections. This process is repeated several times until a fix-point is reached. This procedure lead to high quality restoration plans outside the scope of existing MIP technology [96] and is used in this work for scaling the LPAC-ROP-SPA to larger networks. The RAD method can be classified as a heuristic algorithm to quickly extract sub-optimal solutions. However, heuristic methods in general do not guarantee global optimality/infeasibility, and reaching the global optimal solution could be difficult.

3.7 Experimental Evaluation: Case Studies

This section evaluates restoration plans produce by the ROP-SPA algorithm using the commercial transient simulation software Power World. It considers five well-studied power networks: the 6-bus, 9-bus, 14-bus, 30-bus, and the 50-bus[1] networks from MatPower [92]. For simplicity, it is assumed that the entire network has been destroyed and must be reconstructed from scratch. The restoration plans are quite detailed: They include an ordered list of repairs each with generation dispatch and load pickups. Since our primary goal is to study transient stability/dynamics in restorations, many aspects of these plans in fact need not to be concerned and could be ignored. We make the following assumptions for our study: (1) standard procedures are used for connecting generators to the network; (2) large load pickups are brought up incrementally within the spinning reserve of existing generating units; (3) there is sufficient time to make significant re-dispatch of the generation units between topology changes (i.e. restoration time $>>$ re-dispatch time); (4) Connecting two isolated islands is accomplished with standard procedures for matching the bus phases, voltages, and frequencies. Given these assumptions, the key restoration step with respect to the dynamic simulation is the closing of a line within a connected network, which is precisely the case described in Section 3.5. Hence our dynamic simulation study focuses only on these restoration steps in the ROP plans and evaluate whether our model could enhance transient stability in these steps.

Given these assumptions, the experimental evaluation proceeds as follows. The ROP algorithm produces a restoration plan of $|\mathscr{R}|$ steps (as discussed in Section 3.6). These restoration steps are filtered to the subset $\mathscr{R}'$ of line closings within connected networks. Each restoration step $r \in \mathscr{R}'$ defines a dispatch and a closed steady-state power flow on a subnetwork. The dispatch state is encoded into the POWER WORLD transient simulator with an appropriate line closing event after 10 seconds. The system dynamics are simulated for 50 seconds and the rotor swings δ_t are observed for each time t in the 10–40 second time range. To summarize the rich simulation data, only the largest rotor swing $\max_t \delta_t$ of a generator is reported. For

---

[1]A reduced version of the 57-bus benchmark due to Power World Licensing restrictions.

simplicity, we further simplify our results to report the maximum/average swing values over all generators, i.e., $\max_{i \in G} \max_t \delta_t^i$, and $\frac{1}{|G|} \sum_{i \in G} \max_t \delta_t^i$. To be consistent with field practices, this section first focuses on the effects of SPA constraints and then considers SVD constraints.

3.7.1   Swing Reduction on Fixed Restoration Order

This section first considers the case where the order of component restoration is fixed. This simplifies the computational complexity significantly since the resulting optimization is a linear program. However, the resulting restoration algorithm still produces non-trivial restoration plans since it must choose generation dispatch and load pick-ups that satisfy the SPA constraints. The key findings are: (1) even with a fixed restoration order, SPA constraints can significantly reduce rotor swings; (2) The rotor swing benefits come with a relatively small increase to the size of the blackout period. Table 3.5 summarizes the results for increasingly stronger SPA constraints (i.e., $\theta^\Delta = 180, 10, 5, 2.5, 1.25, 0.625$, and 0.3125 deg.). The case with $\theta^\Delta = 180$ is a baseline with no binding phase angle constraints. The table reports three key metrics: (1) the runtime of the linear program; (2) the blackout period percentage defined as:

$$1 - \frac{\sum_{r=1}^{|\mathscr{R}|} \sum_{p \in \{d,c\}} \sum_{n \in O} \overline{p_l^n} l^n(r,p)}{2|\mathscr{R}| \sum_{n \in O} \overline{p_l^n}}$$

and (3) the relative blackout change, i.e., the changes in blackout percentage compared to initial value in the baseline. The runtimes are consistent for all SPA constraints. In absolute terms, the SPA constraints produce very small increases in the size of the blackout (less than 1.5%) in all cases. Even in relative terms (Δ), the increases tend to be less than 2%, except for the 14-bus case. Figure 3.6 shows the maximum rotor swing of each generator for the restoration plans of outlined in Table 3.5. The various generators in each scenario may have significantly different swing sizes. However, as the SPA constraints become tighter, the swing sizes for all generators decrease consistently by at least 50%.

3.7.2   Swing Reduction on Flexible Restoration Order

This section considers the full ROP program that jointly optimize the prioritization of restoration, generator dispatch, and load pickups. It starts with the small networks that can be solved optimally and then move to the larger networks that are solved using randomized adaptive decomposition.

Complete Search on the 6-Bus and 9-Bus Cases: Table 3.6 and Figure 3.7 present the for the LPAC-ROP-SPA. Table 3.6, when compared to Table 3.5, highlights the benefits of co-optimizing the restoration prioritization, as the blackout percentage is reduced by 3% and 12% in the 6-Bus and 9-Bus networks. Figure 3.7 shows also consistent monotonic reductions in rotor swings. Note that, although Figures 3.7 and 3.6 show similar trends, their values cannot be compared directly because the underlying restoration plans differ.

RAD on the 14-Bus, 30-Bus, and 50-Bus Cases: Consider now the larger benchmarks which are solved with randomized adaptive decomposition. Since this algorithm is randomized, it typically produces different results on each execution and provide no quality guarantees. This section reports only one run of the LPAC-ROP-SPA algorithm and hence these results must be

Table 3.5: Runtime & Blackout on a Fixed Restoration Order for Decreasing SPA Values

	6 Bus			9 Bus		
θ^Δ Deg	Runtime (sec)	Blackout (%)	Δ (%)	Runtime (sec)	Blackout (%)	Δ (%)
180	0.65	32.9574	0.0000	0.42	75.4754	0.0000
10	0.40	32.9574	0.0000	0.35	75.4754	0.0000
5	0.40	32.9574	0.0000	0.36	75.4754	0.0000
2.5	0.40	32.9984	0.1244	0.34	75.4754	0.0000
1.25	0.39	33.2189	0.7935	0.35	75.6439	0.2232
0.625	0.39	33.3974	1.3351	0.34	75.8203	0.4569
0.3125	0.39	33.5618	1.8338	0.35	75.9084	0.5738
	14 Bus			30 Bus		
θ^Δ Deg	Runtime (sec)	Blackout (%)	Δ (%)	Runtime (sec)	Blackout (%)	Δ (%)
180	1.40	7.0319	0.0000	7.71	21.6491	0.0000
10	1.41	7.0319	0.0000	7.84	21.6491	0.0000
5	1.42	7.3180	4.0683	7.13	21.6542	0.0234
2.5	1.52	7.8373	11.4537	6.94	21.7393	0.4165
1.25	1.38	8.1258	15.5559	6.90	21.8318	0.8438
0.625	1.79	8.2787	17.7307	7.84	21.8817	1.0745
0.3125	1.63	8.3573	18.8483	8.83	21.9124	1.2162
	50 Bus					
θ^Δ Deg	Runtime (sec)	Blackout (%)	Δ (%)			
180	29.43	15.2453	0.0000			
10	29.69	15.2454	0.0000			
5	29.94	15.2556	0.0675			
2.5	29.35	15.2679	0.1481			
1.25	30.26	15.2765	0.2041			
0.625	30.00	15.2828	0.2457			
0.3125	29.69	15.2866	0.2704			

Table 3.6: Runtime & Blackout on Optimal Restoration Orderings for Decreasing SPA Values

	6 Bus			9 Bus		
θ^Δ Deg	Runtime (sec)	Blackout (%)	Δ (%)	Runtime (sec)	Blackout (%)	Δ (%)
180	1456.62	29.1442	0.0000	558.88	62.8310	0.0000
10	1233.94	29.1442	0.0000	565.12	62.8310	0.0000
5	1414.19	29.1442	0.0000	493.25	62.8310	0.0000
2.5	608.19	30.2073	3.6478	557.07	62.8310	0.0000
1.25	1206.01	30.2668	3.8518	631.55	62.8310	0.0000
0.625	1129.35	30.3040	3.9795	615.68	63.0012	0.2709
0.3125	1675.22	30.4274	4.4028	753.10	63.1087	0.4420

seen as general trends on not precise values. Table 3.7 summarizes both the restoration plans and the rotor swings for the following step sizes: $\theta^\Delta = 180, 5, 0.625$. The results show the same trend as the smaller benchmarks: As the SPA constraints are tightened, the maximum rotor swings become smaller. However, the results also indicate that the SPA-constraints help in producing smaller blackout sizes. This result is due to the limits on computation times and
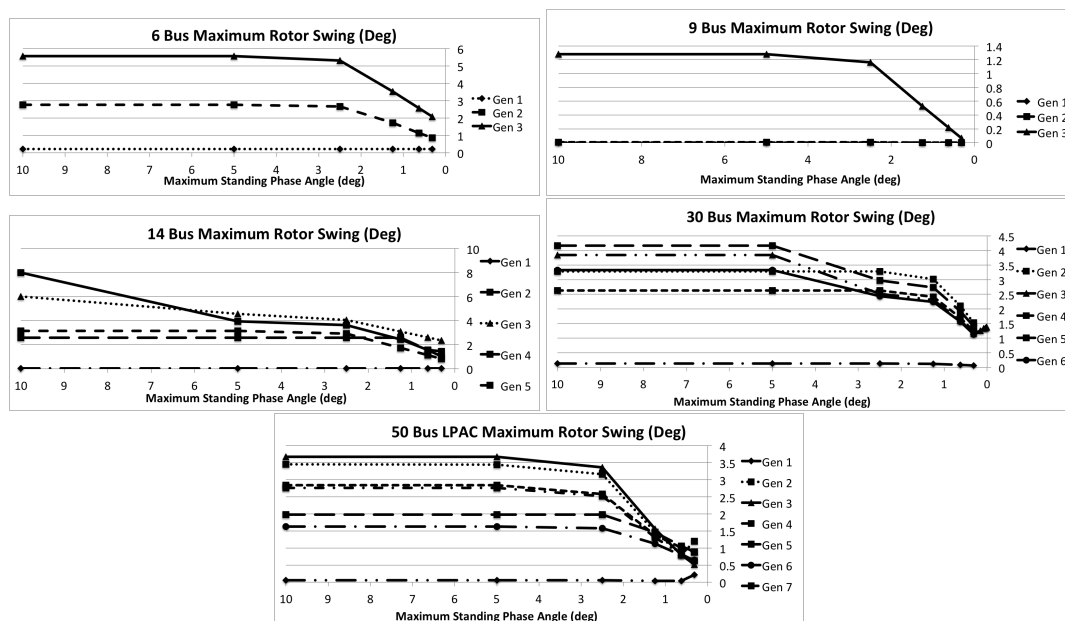
Figure 3.6: Maximum Rotor Swing on a Fixed Restoration Order
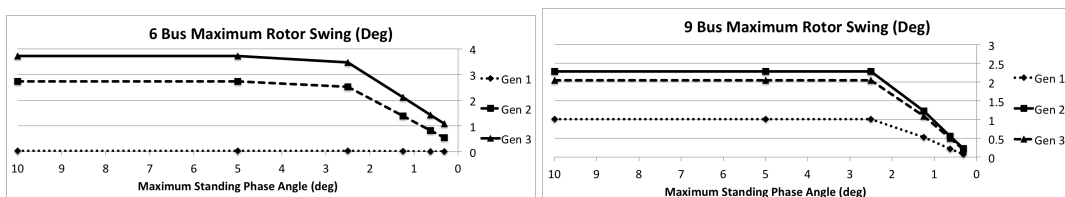
Figure 3.7: Maximum Rotor Swing with Optimal Restoration Orderings

highlights that SPA-constraints can in fact drive the search towards high-quality restoration plans early, while the unconstrained algorithm may explore regions of the search space that may prove infeasible in later steps. Additional experiments are needed to confirm these observations generally but it is important to emphasize that LPAC-ROP-SPA has produced the best restoration plans on these case studies.

3.7.3 The Impact of SVD Constraints

This section considers SVD constraints motivated by the 39-Bus network which is unique for several reasons. First, it has 10 generators, significantly more than other benchmarks. Voltage bounds must be tightened from ± 0.06 V p.u. to ± 0.03 V p.u. to ensure convergence of LPAC-ROP-SPA plans to AC-feasible power flows. Finally, even with tight SPA constraints, the restoration plans produce significant rotor swings. After a detailed investigation, it appears that these swings are caused by significant differences between the voltages on the buses. This was the key motivation in introducing the LPAC-ROP-SPASVD formulation. Table 3.8 and Figure 3.8 present the restoration plan results for a fixed ordering on the 39-bus case with and without a standing voltage difference of $V^\Delta = 0.005$ p.u.. In other words, the restoration

Table 3.7: Runtime, Blackout, & Rotor Swings on RAD for Decreasing SPA Values

14 Bus (Limit: 2 hours)							
θ^Δ Deg	Runtime(sec)	Blackout(%)	Gen 1	Gen 2	Gen 3	Gen 4	Gen 5
180	5427.43	7.0319	0.0326	2.5931	6.0216	7.9865	3.1483
5	7200.06	6.9732	0.0662	4.9771	3.6925	3.2947	4.5103
0.625	7200.18	6.7901	0.0167	1.1987	0.9181	0.8384	1.0966

30 Bus (Limit: 2 hours)								
θ^Δ Deg	Runtime(sec)	Blackout(%)	Gen 1	Gen 2	Gen 3	Gen 4	Gen 5	Gen 6
180	7204.10	21.6491	0.1246	3.1934	3.8476	2.5767	4.1693	3.3256
5	7205.79	19.7539	0.2405	6.3994	3.9005	4.4040	4.2817	3.6690
0.625	7214.51	18.0415	0.2221	0.1504	1.5442	1.4733	0.6440	0.8368

50 Bus (Limit: 4 hours)									
θ^Δ Deg	Runtime(sec)	Blackout(%)	Gen 1	Gen 2	Gen 3	Gen 4	Gen 5	Gen 6	Gen 7
180	14478.96	14.6031	0.0434	0.6521	3.8454	4.6441	5.7794	6.2289	7.6763
5	14403.39	12.8734	0.0288	0.2012	0.6263	1.9467	2.9263	2.9146	3.3718
0.625	14439.81	11.9223	0.0429	0.8242	2.4939	1.9590	1.8267	1.4765	1.6270

plans are evaluated with just SPA constraints (replicating the experiment from Section 3.7.1) and with both the SPA and SVD constraint. We only show four representative generators with significant swings in Figure 3.8.

With SPA constraints only, generators 6 and 7 behave just like the previous experiments but generators 2 and 4 are unique in that their rotor swings do not decrease with tighter SPA constraints. With SVD constraints, the SPA constraints control rotor swings more effectively. Interestingly, setting the SVD limit below 0.005 makes the LPAC-ROP-SPA infeasible. This is not surprising as voltages may not be effectively controlled by generator dispatch and load pickups, especially during restoration stage where equipments are not fully restored. Local reactive power compensation is likely required for the feasibility of small SVD constraints. These results suggest that SPA constraints alone are not enough to ensure small rotor swings: It is advantageous to add SVD constraints to the ROP model and possibly to couple them with local reactive support.

Table 3.8: The 39-Bus New England Test System

	SPA Constraints			SPA and SVD Constraints		
θ^Δ Deg	Runtime (sec)	Blackout (%)	Δ (%)	Runtime (sec)	Blackout (%)	Δ (%)
180	7.48	39.6525	0.0000	10.50	39.7927	0.0000
10	7.60	39.6525	0.0000	9.83	39.7927	0.0000
5	8.25	39.6535	0.0025	8.00	39.7937	0.0025
2.5	7.63	39.6778	0.0636	8.91	39.8184	0.0645
1.25	7.78	39.7399	0.2203	9.12	39.8816	0.2234
0.625	7.64	39.7782	0.3170	10.55	39.9183	0.3157
0.3125	7.40	39.7999	0.3716	10.17	39.9385	0.3664
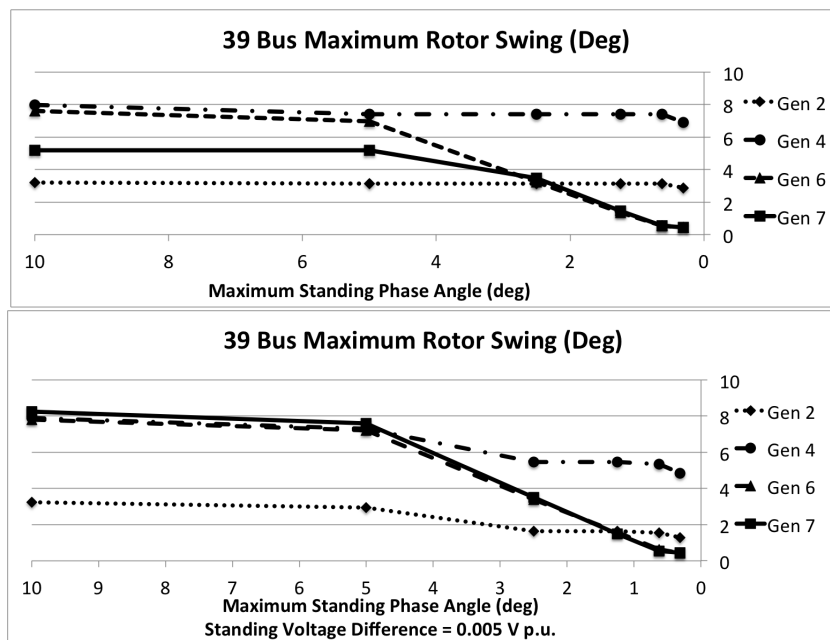
Figure 3.8: Maximum Rotor Swing on 39 Bus: SPA Constraints (top), SPA and SVD Constraints (below)

A Direct Stability Approach on Transmission Line Switching

The previous chapter presents our work to maintain transient stability by using static constraints. We demonstrate this technique through the implementation of standing phase angle constraints and voltage difference constraints in the power systems restoration planning problem. Static constraints are easy to implement, by just adding extra constraints (on steady states) to existing algorithms/software implementations. In general, this is an *indirect method* to maintain transient stability as it cannot directly reason on the dynamic behaviours of a system at the required time scale, hence can be inaccurate when determining the stability of a system. It relies on components being modeled in steady-states, and *indirectly* improve stability via adding extra constraints on these components.

For example, in our line closing routine proposed in previous chapter, we rely on a known fact that the rotor angle separations/swings could be minimized if the standing phase angles are minimized. We use generation dispatch as variables. While this generally works well for many benchmarks, we did not achieve expected result for the 39-bus benchmark. To guarantee transient stability in a more accurate manner, this chapter proposes a direct method to reason directly on the rotor swings of generators. We demonstrate how to incorporate this technique on another important power systems application: transmission line switchings, our second contribution in the thesis for maintaining system stability. While direct approaches allow us to directly extract stable solutions with high accuracy, these methods are usually computationally costly. In addition, they can also drastically increase the modeling complexity and hard to be implemented in computational problem which are already complex (e.g. our work in previous chapter).

4.1   Overview

Transmission line switching is a control action in electrical power systems that has generated increasing attention in recent years. Opening and closing transmission lines change the topology of the grid, redistribute power flows and change the operational state of the system. The control action has been proposed to address voltage issues in the grid, reduce generation costs [59, 60, 25], eliminate congestions, and avoid violating operational constraints [61].

Significant research has devoted to designing algorithms for Optimal Transmission Switch-

ing (OTS) [25]. The goal in OTS is to find the best (sequence of) lines to switch off in order to minimize generation costs. This line of research almost exclusively focuses on analyzing the power flow in the steady-states before and after the switchings. From a mathematical standpoint, the OTS problem for finding the optimal line(s) for single/multiple line switching(s) is a non-convex Mixed-Integer Non-Linear Program (non-convex MINLP), which is computationally challenging. For this reason, most OTS studies replace the non-convex AC power flow equations by the linear DC power flow equations [25, 62, 63, 64, 65]. This reduces the computational complexity, as the DC-OTS problem can be modeled as a Mixed-Integer Linear Program (MILP). Unfortunately, there is no guarantee that the resulting solution can be transformed into an AC-feasible solution [66]. To overcome this limitation, recent work has advocated the use of AC formulations (AC-OTS) or the use of tighter approximations and relaxations [59, 60, 68].

AC-OTS formulations produce an optimal AC-feasible steady state after switchings, but do not guarantee transient stability when the congestion level goes beyond traditional n-1 reliability analysis. Our simulation experiments on the IEEE-39 test case indicate the more congested the network is, the more difficult it becomes to ensure transient stability of OTS. Figure 4.1 depicts simulation results when line (2,25) is open for a congested case of the IEEE 39-bus test system [1, 2] with congested load data taken from NESTA [97]. In the first few seconds, the system seems to maintain stability. However, the system is insufficiently damped, causing oscillatory instability, and later a slipping of generator poles. A loss of generator synchronism (the top left rotor angle plot) can be seen after the fifth second, caused by insufficient damping of generator voltage control (seen from the top right terminal voltage and the bottom excitation control plots).

Power utilities routinely check system stability under peak loads, via simulations on various faulty scenarios (e.g. single line / three phase faults). However, these routines are not exhaustive and mainly served for instability prevention during faults. With growing penetration of renewable energy, transmission switching is often presented as a flexible control action and it becomes important to have automatic routines and controllers that *jointly co-optimize* operational decisions and control settings.

4.2   Our Main Contribution

This chapter is a step in remedying this situation. We propose an automatic routine which actively considered transient stability during optimization. Its key contribution is ***a nonlinear optimization model for Transient-Stable Line Switching (TSLS)*** whose role is to complement an AC-OTS model: For each contemplated line switching, the TSLS model determines set-points for its control variables in order to ensure transient stability or determine transient instability, in which case the switching is rejected. The TSLS optimization model uses a trapezoidal discretization of the differential algebraic equations for the 4th order 2-axis generator model with an automatic voltage regulator (AVR), consisting of an exciter and a stabilizer. The TSLS model features two types of control variables: generation dispatches and stabilizer parameters, and its objective function minimizes the rotor angle accelerations weighted by time in order to damp and stabilize the system. The TSLS model was evaluated primarily on the classical IEEE 10-machine 39-bus system [1, 2] with different congestion scenarios from the
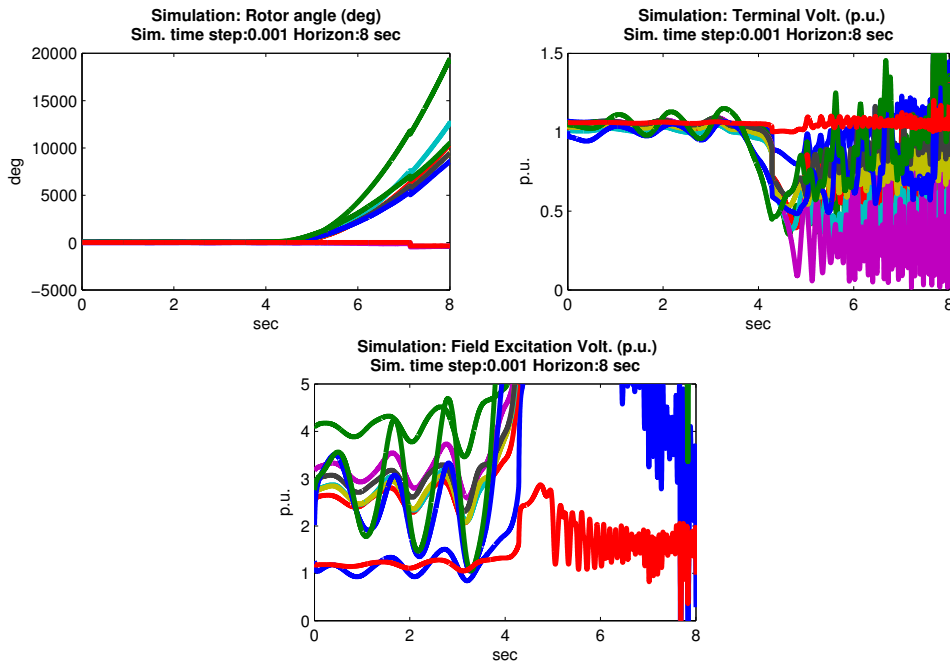
Figure 4.1: NESTA `nesta_case39_epri__api`: Rotor angles (deg, top left), terminal voltage (p.u., top right), and field excitation voltage (p.u., bottom) with 88% congestion level for all generators. Each line represents a generator.

NESTA benchmark [97] to capture peaks in demand, and further extended to the Simplified 14-Generator Model of the South East Australian Power System [98] for scalability studies. We also perform comparisons against the implementation on the classical 2nd order swing equation model. The key findings from the experiments can be summarized as follows:

1. The more congested the system is, the more difficult it is to ensure rotor stability.

2. Due to the lack of excitation controls in classical swing models, the classical model cannot maintain rotor stability for congested scenarios.

3. The variables controlling the set-points of the exciter and the stabilizer are critical to ensure rotor stability, in particular to maintain (small-signal) oscillation stability. With fixed constants for these parameters, stability cannot be obtained for the most congested case.

4. The longer horizon our algorithm considered for optimization, the more stable control solution we could obtain at the expense of computation runtime.

5. The TSLS optimization results were validated against POWERWORLD simulations and exhibits an average error in the order of 10^{-3} degree for rotor angles.

6. The TSLS optimization model is solved with one minute for the coarser, but highly accurate discretization on the IEEE-39 bus test system, and scale well to the larger South East Australian Power System.

Section 4.3 shows our related work in the literature. Section 4.4 introduces the background models and equations we used to derive our model. Section 4.5 introduces the trapezoidal discretization methods, followed by showing the equations and constraints we use to formalize our optimization model. Section 4.6 shows the resulting optimization model, and a high-level line switching routine to guarantee transient stability. Section 4.7 shows the computational case studies and results.

4.3 Related Work

Our work is closely related to the transient-stable optimal power flow problem, first proposed by Gan et al. [22]. The problem was later extended to multi-contingency settings [23] and power systems restorations [32]. All of the above approaches utilize the classical 2nd order swing equation model to reason on transient stability. Our work extends these works by further considering the more complex 4th order 2-Axis Model with automatic voltage regulation (AVR): including an exciter and a stabilizer (PSS) during optimization. Our work is also related to techniques improving stability during transmission loop closures in normal operating conditions, e.g., techniques on reducing rotor shaft impacts and standing phase angles [21, 18, 19, 20].

4.4 Background

The dynamic response of a power system after a disturbance can be abstractly written and described by [5, 23]:

$$\dot{x} = f(x,y), \ \ 0 = g(x,y)$$

where $f(\bullet)$ represents a set of first-order differential equations describing the power system dynamics, and $g(\bullet)$ represents a set of algebraic equations describing the passive equipments. Vector x captures the short-term dynamic variables and y is a vector of algebraic state variables. Given an initial condition for variables x and y, we then compute the transient states of the network over time. In this chapter, we mainly focus on generator electro-mechanical dynamics and phenomenon within a time horizon from a few seconds up to half of a minute. The remaining equipments in the power transmission network, including transmission lines, circuit breakers, and loads are modeled as passive equipments. We now describe the technical details of the generator dynamics in our model. Table 4.1 lists the notations and symbols we used to describe generator models and dynamics.

4.4.1 Generator Model: Swing Equation

This chapter captures the rotor dynamics by using the following two classical swing equations [5, 69]:

$$\frac{d\delta^i}{dt} = \omega^i - \omega^0, \qquad \frac{2H^i}{\omega^0}\frac{d\omega^i}{dt} = p_m^i - p_e^i - D^i\omega^i$$

Table 4.1: Nomenclature for generator models and dynamics

Nomenclature for generator dynamics	
δ	Rotor angle (rad)
ω	Rotor speed (rad/sec)
a	Rotor acceleration (rad/sec^2)
H	Inertia constant (MW · sec/MVA)
p_m, p_e	Active mechanical power & electrical power (p.u.)
q_e	Reactive electrical power (p.u.)
D	Damping coefficient (p.u.)
E_d, E_q	d-axis and q-axis generator stator emfs (p.u.)
X'	Transient reactance [Classical swing model] (p.u.)
X'_d, X'_q	d-axis and q-axis transient reactance [Two-axis model] (p.u.)
X_d, X_q	d-axis and q-axis synchronous reactance [Two-axis model] (p.u.)
E_{fd}	Excitation field voltage (p.u.)
T'_{do}, T'_{qo}	open circuit d- and q-axis time constants (sec)
I_d, I_q	d- anx q-axis stator currents (p.u.)
V_w, K_s, T_w	Washout output, gain, and time constant (sec) [PSS]
T_1 to T_4	Lead-lag time constants (sec) [PSS]
V_{ll1}, V_{ll2}	Lead-Lag output [PSS]
V_s, V_{ref}, E_s	PSS output, volt. reference, and exciter input
T_A, T_B	Lead-lag time constants (sec) [Excitor]
Δ	Discretization time constant (sec)
K_a, T_{fd}	Gain amplifying and time constants [Excitor]

where $H^i, \delta^i, D^i, \omega^i$, and ω^0 denote the inertia constant, rotor angle, the damping coefficient, the angular velocity, and the nominal angular velocity of a generator i. The nominal angular velocity is assumed constant for all generators at either 50Hz or 60Hz (i.e., $\omega^0 = 2\pi50$ or $\omega^0 = 2\pi60$). p^i_m and p^i_e represent the mechanical and electrical powers acting on the rotor of generator i. δ^i and ω^i are short-term dynamic variables, and p^i_m and p^i_e are algebraic state variables. In steady states, the mechanical power is assumed to be equal to the electrical power and the rotor angles of all generators remain constant (i.e., $\frac{d\omega^i}{dt} = 0, \forall i \in G$). The angular velocity ω^i is traditionally defined as an offset with respect to the nominal angular velocity ω^0, which allows us to drop the ω^0 term (first equation). Traditionally, D is an implicit constant used to approximate damping effects on windings and stabilizers. In cases when there are explicit models on damping controls, e.g. an automatic voltage regulator with stabilizers, the term $D^i w^i$ in the second equation can be ignored, or set D^i equals to zero.

4.4.2   Generator Model: Classical Swing Model

Due to its simplicity, transient studies throughout the literature often use the classical generator machine model [5, 69] to model generator machine, represented by a constant voltage source behind a fixed transient reactance. The active power p^i_e and reactive power q^i_e of a generator i

can then be easily characterized by the following two equations:

$$p_e^i = \frac{E_{fd}^i V^i}{X'^i} \sin(\delta^i - \theta^i)$$

$$q_e^i = -\frac{(V^i)^2}{X'^i} + \frac{E_{fd}^i V^i}{X'^i} \cos(\delta^i - \theta^i)$$

where E_{fd}^i, V^i, X'^i, δ^i, θ^i are the (constant) excitation field voltage, terminal bus voltage in magnitude, transient reactance, rotor angle, and the bus phase angle respectively.

4.4.3   Generator Model: 2-Axis Model

Our work use the more complex two-axis model [69] to account for excitation phenomenon, driven by automatic voltage regulators which are widely installed in nowadays power systems. In the two-axis model, the active (p_e^i) and reactive (q_e^i) power of generator i will be described directly in terms of the generator stator emfs, leading to rotor flux components in two axes: the direct axis (d-axis, E_d^i) and the quadrature axis (q-axis, E_q^i):

$$p_e^i = \frac{E_q^i V^i \sin(\delta^i - \theta^i)}{X_d'^i} + \frac{E_d^i V^i \cos(\delta^i - \theta^i)}{X_q'^i} + \frac{(V^i)^2 (X_d'^i - X_q'^i) \sin(2\delta^i - 2\theta^i)}{2X_d'^i X_q'^i}$$

$$q_e^i = -\frac{(V^i)^2}{X_d'^i} + \frac{E_q^i V^i \cos(\delta^i - \theta^i)}{X_d'^i} - \frac{E_d^i V^i \sin(\delta^i - \theta^i)}{X_q'^i} + \frac{(V^i)^2 (E_d'^i - E_q'^i)(\cos(2\delta^i - 2\theta^i) - 1)}{2X_d'^i X_q'^i}$$

where E_q^i, E_d^i, V^i, θ^i, $X_d'^i$, and $X_q'^i$ are the q-axis stator emf, d-axis stator emf, terminal bus voltage (magnitude), the bus phase angle, d-axis transient reactance, and q-axis transient reactance of generator i respectively. The dynamics of the two stator emfs E_q^i and E_d^i are further described by:

$$T_{do}'^i \frac{dE_q^i}{dt} = E_{fd}^i - E_q^i + (X_d^i - X_d'^i) I_d^i,$$

$$T_{qo}'^i \frac{dE_d^i}{dt} = -E_d^i + (X_q^i - X_q'^i) I_q^i$$

where E_{fd}^i is the excitation field voltage controlled by the automatic voltage regulators (AVRs) and power systems stabilizers (PSS), $T_{do}'^i$ and $T_{qo}'^i$ are the open circuit d- and q-axis time constants, X_d^i and X_q^i are the d- and q-axis synchronous reactance, and I_d^i and I_q^i are the d- and q-axis stator currents for generator i respectively. Finally, we have the following equations to link the stator currents to the terminal voltage and the stator emfs:

$$I_d^i = \frac{V^i \cos(\delta^i - \theta^i) - E_q^i}{X_d'^i}, I_q^i = \frac{V^i \sin(\delta^i - \theta^i) + E_d^i}{X_q'^i}$$

When combining with the swing equations, the two-axis model will give four ordinary differential equations (aka the 4th-order model), while the classical model will still have only two (aka the 2nd order classical model).
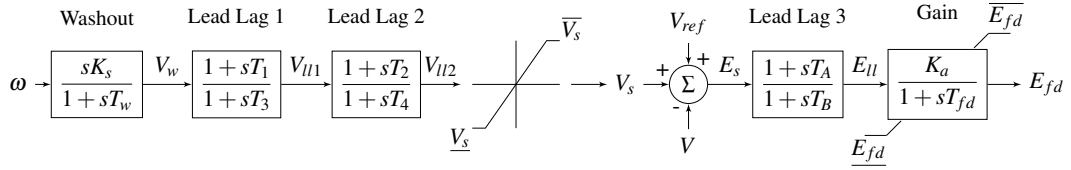
Figure 4.2: The control block diagram of our automatic voltage regulator (AVR), with one exciter: SEXS_PTI [7] and one stabilizer: STAB1 [7]

4.4.4 Automatic Voltage Regulation Model (AVR)

Our generator model implements a simplified excitation system model SEXS_PTI [7] combined with a speed-sensitive stabilizing model STAB1 [7]. Figure 4.2 shows the combined block diagram for all of the transfer functions in Laplace form. The circuit requires three external inputs: the terminal voltage V, the steady-state terminal voltage reference V_{ref}, and the angular velocity/speed of the rotor angle ω. The excitation circuit consists of three time constants: T_A and T_B in the lead-lag block and T_{fd} in the amplification block, one amplification gain parameter K_a and two limits $\overline{E_{fd}}$ and $\underline{E_{fd}}$ to avoid over-excitation. The speed-sensitive stabilizing circuit consists of 5 time constants: T_w in the wash out block and T_1 to T_4 in the two lead-lag block, one wash out gain constant K_s, and again two limits $\overline{V_s}$ and $\underline{V_s}$ to limit the stabilizing signal V_s.

4.5 Finite Difference Method: Trapezoidal Discretization

To optimize the generator model with the AVR containing ordinary differential equations, one method is to use direct time discretization method to convert the continuous optimization problem into a finite-time discretized nonlinear program. We follow previous work [22] and perform an implicit trapezoidal discretization to discretize the equations over a discrete horizon ($1 \leq t \leq T$). This approach discretizes the first-order differential equation

$$\frac{df(t)}{dt} = k(t)$$

over a finite discrete time horizon $1 \leq t \leq T$ with uniform time step Δ by converting it into its integral form

$$\int_t^{t+\Delta} \frac{df(t)}{dt} dt = f(t+\Delta) - f(t) = \int_t^{t+\Delta} k(t)dt$$

and using the Trapezoidal rule as follows:

$$\int_t^{t+\Delta} k(t)dt \approx \frac{\Delta}{2}[k(t) + k(t+\Delta)]$$

The same approximation is repeated to cover the required horizon and gives

$$f(t+\Delta) - f(t) \approx \frac{\Delta}{2}[k(t) + k(t+\Delta)], 1 \leq t \leq T$$

We now show the discretized formulations for building our optimization model. To simplify our notation, we normalize and define our set of discretized time steps t to be the set of positive integers $\{1, 2, \ldots, T\}$. Each adjacent pair of steps will be separate by the desired uniform time step Δ. We append t within brackets to variables to denote the values of the variables at time step t. We also use $t|_{t=n}$ to explicitly refer to a specific time step n $(1 \le n \le T)$.

4.5.1   Generator Dynamics: Swing equations

The Swing equations then become

$$\delta^i(t+1) - \delta^i(t) - \frac{\Delta}{2}(\omega^i(t+1) + \omega^i(t)) = 0 \tag{4.1}$$

$$\omega^i(t+1) - \omega^i(t) - \frac{\Delta}{2}(a^i(t+1) + a^i(t)) = 0 \tag{4.2}$$

$$a^i(t) - \frac{\omega^0}{2H^i}(p_m^i - p_e^i(t) - D^i\omega^i(t)) = 0 \tag{4.3}$$

for all generator $i \in G$ and all time steps $t \in [1..T-1]$. We set D^i to zero if an explicit damping model is implemented, e.g. if a power system stabilizer (PSS) is modeled explicitly. The initial boundary conditions at $t = 1$ is given by

$$\omega^i(t|_{t=1}) = 0, a^i(t|_{t=1}) = 0, \qquad\qquad \forall i \in G. \tag{4.4}$$

by assuming steady state holds in the first time step (i.e. at $t = 1$). For mechanical power, we assume the (supplying) power is in perfect balance with respect to the electrical (drawing) power in steady state (i.e. at $t = 1$), and remains constant throughout the transient period:

$$p_m^i = p_e^i(t|_{t=1}) \qquad\qquad \forall i \in G. \tag{4.5}$$

Since this study primarily focus on short-term transient effects with AVR controllers, the effect of most frequency/droop controllers acting on mechanical power are relatively small and insignificant, as these controllers respond and react in a comparatively slower time scale. Therefore, it is reasonable to assume mechanical power to be constant. Droop and frequency controls are known to be important on mid-term to long-term stability. Further extending our work to incorporate droop/frequency controllers will be left as future work.

To ensure rotor stability, one acceptable criteria [22] is to ensure that the rotor angles are not too far from each others before and after the disturbance period. One typical approach is to define a reference angle $\delta^r(t)$ representing the angle for the center of inertia (COI):

$$\delta^r(t) = \frac{\sum_{i \in G} H^i \delta^i(t)}{\sum_{i \in G} H^i}, \qquad\qquad 1 \le t \le T. \tag{4.6}$$

and to enforce constraints to ensure rotor angles are not too far from the angle for the COI. For all generators $i \in G$, the stability constraints will then be:

$$-\overline{\delta} \le \delta^i(t) - \delta^r(t) \le \overline{\delta}, \qquad\qquad \{1\} \cup \{t : T_k \le t \le T\} \tag{4.7}$$

where T_k is an adjustable time constant representing the earliest time that the constraint has to be enforced (after switchings), and $\bar{\delta}$ is an adjustable parameter representing the maximum rotor angle separation. In the literature, $\bar{\delta}$ is usually set to $\pi/2$ (in radian).

4.5.2 Generator Dynamics: Generator Power

The generation active and reactive power can be easily extended to the discretized space by repeating the equations to all time steps t. For the classical swing model, we have the following two equations. For all $i \in G, t \in [1..T]$:

$$p_e^i(t) = \frac{E_{fd}^i(t)V^i(t)}{X'^i} \sin(\delta^i(t) - \theta^i(t)) \tag{4.8}$$

$$q_e^i(t) = -\frac{(V^i(t))^2}{X'^i} + \frac{E_{fd}^i(t)V^i(t)}{X'^i} \cos(\delta^i(t) - \theta^i(t)) \tag{4.9}$$

For the two-axis model, we have the following:

$$p_e^i(t) = \frac{E_q^i(t)V^i(t)\sin[\delta^i(t) - \theta^i(t)]}{X_d'^i} + \frac{E_d^i(t)V^i(t)\cos[\delta^i(t) - \theta^i(t)]}{X_q'^i} +$$
$$\frac{[V^i(t)]^2(X_d'^i - X_q'^i)\sin[2\delta^i(t) - 2\theta^i(t)]}{2X_d'^i X_q'^i} \tag{4.10}$$

$$q_e^i(t) = -\frac{[V^i(t)]^2}{X_d'^i} + \frac{E_q^i(t)V^i(t)\cos[\delta^i(t) - \theta^i(t)]}{X_d'^i} - \frac{E_d^i(t)V^i(t)\sin[\delta^i(t) - \theta^i(t)]}{X_q'^i}$$
$$+ \frac{[V^i(t)]^2[E_d'^i(t) - E_q'^i(t)]\{\cos[2\delta^i(t) - 2\theta^i(t)] - 1\}}{2X_d'^i X_q'^i} \tag{4.11}$$

for all $i \in G, t \in [1..T]$.

4.5.3 Generator Dynamics: Stator EMF Dynamics

Similarly, the d- and q-axis stator emf dynamics will be discretized to:

$$T_{do}'^i E_q'^i(t) = E_{fd}^i(t) - E_q^i(t) + (X_d^i - X_d'^i)I_d^i(t) \tag{4.12}$$

$$T_{qo}'^i E_d'^i(t) = -E_d^i(t) + (X_q^i - X_q'^i)I_q^i(t) \tag{4.13}$$

$$I_d^i(t) = \frac{V^i(t)\cos[\delta^i(t) - \theta^i(t)] - V_q^i(t)}{X_d'^i} \tag{4.14}$$

$$I_q^i(t) = \frac{V^i(t)\sin[\delta^i(t) - \theta^i(t)] + V_d^i(t)}{X_q'^i} \tag{4.15}$$

for all $i \in G, t \in [1..T]$, with the following trapezoidal rule to approximate the rate of the emf dynamics:

$$E_q^i(t+1) - E_q^i(t) - \frac{\Delta}{2}[E_q'^i(t+1) + E_q'^i(t)] = 0 \qquad (4.16)$$

$$E_d^i(t+1) - E_d^i(t) - \frac{\Delta}{2}[E_d'^i(t+1) + E_d'^i(t)] = 0 \qquad (4.17)$$

for all $i \in G, t \in [1..T-1]$. Similarly, we have the following initial boundary conditions at $t = 1$:

$$E_d'^i(t|_{t=1}) = 0, E_q'^i(t|_{t=1}) = 0, \qquad\qquad \forall i \in G. \qquad (4.18)$$

by assuming steady state in the first time step.

4.5.4 Automatic Voltage Regulator: Exciter

We now show how we transform the transfer functions (in Laplace domain) in our AVR into time-domain differential equations for optimization. Let $O(s)/O(t)$ and $I(s)/I(t)$ be the output function and input function in the Laplace (s) / time (t) domain. We assume the transfer functions are given with the zero initial condition (i.e. O(0) and I(0) in Laplace domain are zero), which is a common property in power systems control. All of the transfer functions appearing in Figure 4.2 can be written in abstract form as:

$$\frac{K_m + sT_m}{K_n + sT_n} = \frac{O(s)}{I(s)}$$

$$\Longleftrightarrow I(s)(K_m + sT_m) = O(s)(K_n + sT_n)$$

$$\Longleftrightarrow s(I(s)T_m - O(s)T_n) = O(s)K_n - I(s)K_m$$

$$\Longleftrightarrow \frac{d}{dt}(I(t)T_m - O(t)T_n) = O(t)K_n - I(t)K_m$$

$$\Longleftrightarrow \frac{dX(t)}{dt} = O(t)K_n - I(t)K_m,$$

where $X(t)$ is defined as $I(t)T_m - O(t)T_n$. For lead-lag blocks, we have $K_m = K_n = 1$. These dynamic equations reduce to:

$$\frac{dX(t)}{dt} = O(t) - I(t)$$

For washout blocks, we have $K_n = 1, K_m = 0$. These dynamic equations similarly reduce to:

$$\frac{dX(t)}{dt} = O(t)$$

For excitation amplification blocks, we have $K_n = 1, T_m = 0$, and therefore we have:

$$\frac{dX(t)}{dt} = O(t) - K_m I(t), \text{ s.t. } X(t) = -T_n O(t)$$

By using the above three transformation rule, we have the following equations describing the excitation circuits:

$$T_{fd}^{'i} E_{fd}^{'i}(t) = -E_{fd}^i(t) + K_a^i E_{ll}^i(t) \qquad \text{(Gain)} \qquad (4.19)$$

$$X_{ll}^{'i}(t) = E_s^i(t) - E_{ll}^i(t) \qquad \text{(Lead-Lag)} \qquad (4.20)$$

$$X_{ll}^i(t) = T_B^i E_{ll}^i(t) - T_A^i E_s^i(t) \qquad \text{(Lead-Lag)} \qquad (4.21)$$

$$E_s^i(t) = V_{ref}^i - V^i(t) + V_s^i(t) \qquad \text{(Summation)} \qquad (4.22)$$

for all $i \in G, t \in [1..T]$, with the following trapezoidal rule to approximate the dynamics:

$$E_{fd}^i(t+1) - E_{fd}^i(t) - \frac{\Delta}{2}[E_{fd}^{'i}(t+1) + E_{fd}^{'i}(t)] = 0 \qquad (4.23)$$

$$X_{ll}^i(t+1) - X_{ll}^i(t) - \frac{\Delta}{2}[X_{ll}^{'i}(t+1) + X_{ll}^{'i}(t)] = 0 \qquad (4.24)$$

for all $i \in G, t \in [1..T-1]$. Again, we have the following initial boundary conditions at $t = 1$:

$$E_{fd}^{'i}(t|_{t=1}) = 0, X_{ll}^{'i}(t|_{t=1}) = 0 \qquad (4.25)$$

for all $i \in G$. The only equipment we remain to convert to the time domain is the non-windup limiters on the gain block. The limiters will change and set the differential $\frac{dE_{fd}}{dt}$ and the state E_{fd} when the state goes lower/higher than the lower/upper bounds (called saturation behaviours), as follows:

$$\frac{dE_{fd}}{dt} = 0 \wedge E_{fd} = \overline{E_{fd}}, \qquad \text{if } E_{fd} \geq \overline{E_{fd}} \wedge \frac{dE_{fd}}{dt} \geq 0$$

$$\frac{dE_{fd}}{dt} = 0 \wedge E_{fd} = \underline{E_{fd}}, \qquad \text{if } E_{fd} \leq \overline{E_{fd}} \wedge \frac{dE_{fd}}{dt} \leq 0$$

To implement the limiter (in time-domain) for optimization, binary/integer variables would need to be used, introducing significant computational complexity and making the approach intractable. One alternative proposal is to enforce **stricter** bounds:

$$\underline{E_{fd}^i} \leq E_{fd}^i(t) \leq \overline{E_{fd}^i}, \qquad \forall i \in G, 1 \leq t \leq T. \qquad (4.26)$$

One possible outcome is that we will not be able to look for stable solutions utilizing saturation behaviours of limiters (i.e. allowing excitation controls E_{fd} to go lower/higher than the bounds and use limiters to rectify the controls). While enforcing a stricter bounds would indeed result in a more **conservative** optimization, due to the requirement for solvers to look for control settings that satisfy the tightened bounds without saturation behaviours, this approach would still guarantee stability if a solution is being found.

One future research direction is to perform optimization on the relaxation of the constraints by enforce looser bounds. One way is to add slackness variables to $\overline{E_{fd}^i}$ and $\underline{E_{fd}^i}$ and minimize the overall magnitude of the slackness variables. Note that this approach is a relaxation approach which could allow originally infeasible or unstable solutions to be included in the solution set.

4.5.5   Automatic Voltage Regulator: Stabilizer

By using similar transformation technique, we will have the following equations to describe our stabilizer (PSS):

$$X_w'^i(t) = V_w^i(t) \qquad \text{(Wash out)} \qquad (4.27)$$

$$X_w^i(t) = K_s^i \omega^i(t) - T_w^i V_w^i(t) \qquad \text{(Wash out)} \qquad (4.28)$$

$$X_{ll1}'^i(t) = V_w^i(t) - V_{ll1}^i(t) \qquad \text{(Lead-Lag 1)} \qquad (4.29)$$

$$X_{ll1}^i(t) = T_3^i V_{ll1}^i(t) - T_1^i V_w^i(t) \qquad \text{(Lead-Lag 1)} \qquad (4.30)$$

$$X_{ll2}'^i(t) = V_{ll1}^i(t) - V_{ll2}^i(t) \qquad \text{(Lead-Lag 2)} \qquad (4.31)$$

$$X_{ll2}^i(t) = T_4^i V_{ll2}^i(t) - T_2^i V_{ll1}^i(t) \qquad \text{(Lead-Lag 2)} \qquad (4.32)$$

for all $i \in G, t \in [1..T]$, with the following trapezoidal rule:

$$X_w^i(t+1) - X_w^i(t) - \frac{\Delta}{2}[X_w'^i(t+1) + X_w'^i(t)] = 0 \qquad (4.33)$$

$$X_{ll1}^i(t+1) - X_{ll1}^i(t) - \frac{\Delta}{2}[X_{ll1}'^i(t+1) + X_{ll1}'^i(t)] = 0 \qquad (4.34)$$

$$X_{ll2}^i(t+1) - X_{ll2}^i(t) - \frac{\Delta}{2}[X_{ll2}'^i(t+1) + X_{ll2}'^i(t)] = 0 \qquad (4.35)$$

for all $i \in G, t \in [1..T-1]$, with similar initial conditions:

$$X_w'^i(t|_{t=1}) = 0, X_{ll1}'^i(t|_{t=1}) = 0, X_{ll2}'^i(t|_{t=1}) = 0 \qquad (4.36)$$

for all $i \in G$. We now remain to show how to handle the limiters in the stabilizers for our optimization formulation. These limiters are windup limiters (also called saturation limiters) for filtering and modifying signal V_s before inputing to the exciters. The limiters will change and set the state V_s when the input state V_{ll2} goes lower/higher than the lower/upper bounds, as follows:

$$V_s = \overline{V_s}, \qquad\qquad \text{if } V_{ll2} \geq \overline{V_s}$$

$$V_s = \underline{V_s}, \qquad\qquad \text{if } V_{ll2} \leq \overline{V_s}$$

$$V_s = V_{ll2}, \qquad\qquad \text{otherwise}$$

To implement this limiter for optimization and avoid integer variables with similar reasonings from previous sections, we choose to enforce the stricter bounds:

$$V_{ll2}^i(t) = V_s^i(t), \underline{V_s^i} \leq V_s^i(t) \leq \overline{V_s^i}, \qquad\qquad \forall i \in G, 1 \leq t \leq T. \qquad (4.37)$$

4.5.6   Power Network: AC Power Flow

It remains to link the AC power flow equations to the generator dynamics. The model states the active and reactive flow balance equations

$$\sum_{m \in G(n)} p_e^m(t) - \sum_{m \in O(n)} p_l^m - [V^n(t)]^2 g_s^n = \sum_{m \in N(n)} p^{nm}(t)$$

$$\sum_{m \in G(n)} q_e^m(t) - \sum_{m \in O(n)} q_l^m + [V^n(t)]^2 b_s^n = \sum_{m \in N(n)} q^{nm}(t) \qquad (4.38)$$

for all bus $n \in N$, where $p_e^m(t)$ and $q_e^m(t)$ are the active and reactive power of generator m, p_l^m and q_l^m are the active and reactive demands of load m, $[V^n(t)]^2 g_s^n$ and $[V^n(t)]^2 b_s^n$ describe the active and reactive power drawn by the bus shunt $(g_s^n + i b_s^n)$ at bus n, and $p^{nm}(t)$ and $q^{nm}(t)$ are the active and reactive power flow from n to m (i.e. bus injections). We use $G(n), O(n)$, and $N(n)$ to denote the set of generators, loads, and neighboring buses of bus n. In this work, we simplify our experiments and use constant active and reactive power loads to demonstrate our techniques. Note that we can easily extend our model with: impedance, current, or even dynamic loads (based on voltage/frequency) by adjusting and replacing the two terms: p_l^m and q_l^m. We reuse the AC power flow equations introduced in Chapter 2.1.2 for describing the power flow of a transmission line:

$$p^{nm}(t) = z^{nm}(t) \{ \frac{g^{nm}}{Tl^{nm}} [V^n(t)]^2 - \frac{V^n(t) V^m(t)}{Tr^{nm}} [g^{nm} \cos(\Theta^{nm}(t)) + b^{nm} \sin(\Theta^{nm}(t))] \}$$

$$q^{nm}(t) = z^{nm}(t) \{ -\frac{b^{nm} + (l_c^{nm})/2}{Tl^{nm}} [V^n(t)]^2 -$$

$$\frac{V^n(t) V^m(t)}{Tr^{nm}} [g^{nm} \sin(\Theta^{nm}(t)) - b^{nm} \cos(\Theta^{nm}(t))] \}$$

$$\text{s.t. } \Theta^{nm}(t) = \theta^n(t) - \theta^m(t) + \phi^{nm} \qquad (4.39)$$

where $g^{nm} + i b^{nm}$ is the line admittance, l_c^{nm} is the line charge, and $z^{nm}(t)$ is an on-off variable to determine whether line (n,m) is opened or closed at the current time period t. We assume $z^{nm}(t) = z^{mn}(t)$ for every time step t. During implementation, they will be implemented as the same variable. Recall ϕ^{nm} denotes the constant phase shift angle from bus n to bus m if transmission line (n,m) has a phase shifting transformer/device, Tr^{nm} denotes the off-nominal turns ratio of a transformer on line (n,m) with $Tr^{nm} = Tr^{mn}$, and Tl^{nm} is a modeling parameter setting to $[Tr^{nm}]^2$ if bus n connects to the *from* end of the transformer and bus m connects to the *to* end of the transformer.
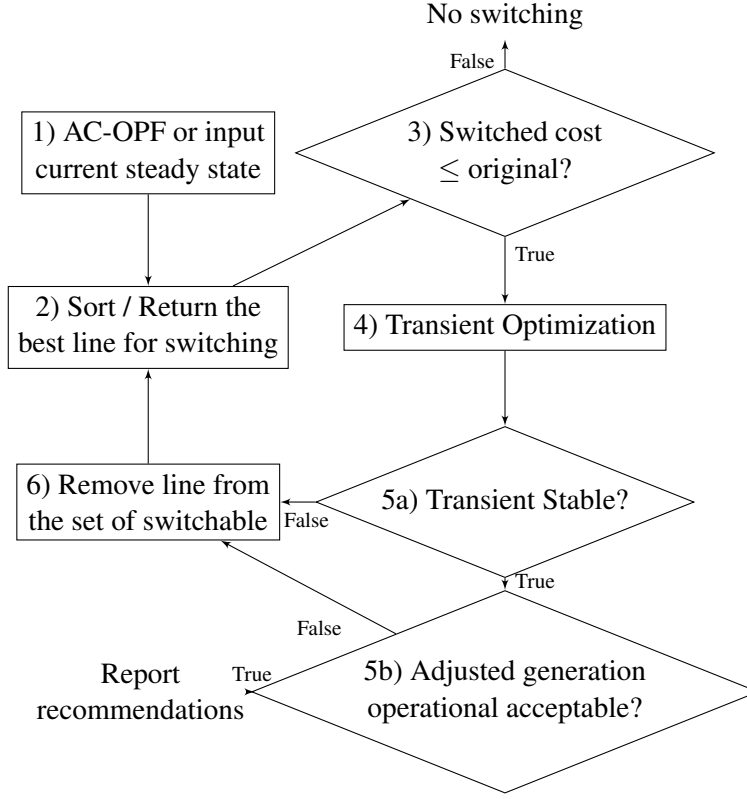
Figure 4.3: Transient Stable Line Switching Algorithm

4.5.7   Power Network: Operational Limits

The active and reactive generation and line thermal/power limits for the initial steady state are given by

$$\underline{p_e^i} \le p_e^i(t|_{t=1}) \le \overline{p_e^i} \qquad \forall i \in G \qquad (4.40)$$

$$\underline{q_e^i} \le q_e^i(t|_{t=1}) \le \overline{q_e^i} \qquad \forall i \in G \qquad (4.41)$$

$$[p^{nm}(t|_{t=1})]^2 + [q^{nm}(t|_{t=1})]^2 \le [\overline{S^{nm}}]^2 \qquad \forall(n,m) \in L \qquad (4.42)$$

where $\overline{S^{nm}}$ denotes the maximum apparent power. We also enforce the following limits across all time steps t:

$$\underline{V^n} \le V^n(t) \le \overline{V^n}, \qquad \forall n \in N \qquad (4.43)$$

$$-\overline{\theta} \le \delta^n(t) - \theta^n(t) \le \overline{\theta}, \qquad \forall n \in G \qquad (4.44)$$

$$-\overline{\theta} \le \theta^n(t) - \theta^m(t) \le \overline{\theta}, \qquad \forall(n,m) \in L \qquad (4.45)$$

4.6   Transient Stable Line Switching

This section presents our optimization model for transient-stable transmission line switching.

4.6.1 Line switching routine with transient stability

Figure 4.3 shows an automatic routine utilizing our proposed model to find the best transmission line to switch without causing transient instability. The routine itself can be seen as introducing a stability checker on top of the AC Optimal Transmission Switching Model (AC-OTS). If the AC-OTS model returns the global optimal solution, the overall routine would still be globally optimal. The main focus of our routine is to answer whether extra control actions are necessary to ensure stability for the switching proposed by AC-OTS.

1. The routine executes AC Optimal Power Flow algorithm (AC-OPF) to determine the current system state.

2. Based on the computed steady state, it finds the best line to switch (e.g., based on costs/congestions), e.g., by using the AC Optimal Transmission Switching Model in Chapter 2.1.4.2.

3. It checks whether the switched line reduces generation costs.

4. It then executes our model to search for a feasible optimal control solution to ensure finite-time transient stability when switching the proposed line.

5. It checks if the solution is transient stable and operationally acceptable.

6. If no feasible solution is found, the line will be discarded.

4.6.2 Transient optimization model

We now present the optimization model for implementing Step 4. TSLS-C uses the 2nd order classical swing equation model to model generator machines, while TSLS-T uses the 4th order 2-axis machine model to further consider excitation controls.

Transient Stable Line Switching with Classical Generator Model (TSLS-C)

$$\min \sum_{n \in G} \sum_{t \in [1,T]} [t(a^n(t))]^2 \qquad \text{(O1)}$$

$$
\begin{aligned}
s.t. \quad &\text{Swing equations \& stability:} && (4.1) - (4.7) \\
&\text{Generator power:} && (4.8) - (4.9) \\
&\text{AC network power flow:} && (4.38) - (4.39) \\
&\text{Operational limits:} && (4.40) - (4.45) \\
&\text{Active power flexible region:} && |p_e^i(t|_{t=1}) - p_T^i| \leq r p_T^i \\
&\text{Reactive power flexible region:} && |q_e^i(t|_{t=1}) - q_T^i| \leq r q_T^i \\
&\text{Re-dispatch cost constraint:} && c \leq (1 + \gamma) c_T
\end{aligned}
$$

Transient Stable Line Switching with Two-Axis Generator Model (TSLS-T)

$$\min \sum_{n \in G} \sum_{t \in [1,T]} [t(a^n(t))]^2 \tag{O1}$$

s.t.	Swing equations & stability:	$(4.1) - (4.7)$
	Generator power:	$(4.10) - (4.11)$
	Stator EMF dynamics:	$(4.12) - (4.18)$
	Excitation dynamics:	$(4.19) - (4.26)$
	PSS dynamics:	$(4.27) - (4.37)$
	AC network power flow:	$(4.38) - (4.39)$
	Operational limits:	$(4.40) - (4.45)$
	Active power flexible region:	$\|p_e^i(t\|_{t=1}) - p_T^i\| \leq r p_T^i$
	Reactive power flexible region:	$\|q_e^i(t\|_{t=1}) - q_T^i\| \leq r q_T^i$
	Re-dispatch cost constraint:	$c \leq (1 + \gamma)c_T$

where p_T^i and q_T^i are the active and reactive power of generator i in step 1, c and c_T are total generation costs of the current optimization problem and the generation costs in step 1. r and γ are adjustable parameters governing the maximum generator resources and maximum increase in generation costs allowed to achieve transient stability. Since our model could only guarantee stability within the computed horizon, solutions obtained from the model may not guarantee to be (oscillation) stable at any future time steps. One way to consider the stability continuity is to restrict our attention to solutions that provide enough damping and reduce the magnitude/amplitude of transient swings over time. The objective function (O1) minimizes the sum of time-weighted rotor angle accelerations, where the time-weights ensure that the solutions have smaller swings (in terms of amplitude) as time increases.

4.7 Computational Case Study

This section evaluates the TSLS optimization models on the classical IEEE 10-machine 39-bus systems [1, 2] with the network data from Matpower [99]. The dynamics data (i.e., generator machine and AVR parameter) are obtained from a recent release (November 2013) of the IEEE PES Task Force on benchmark systems for stability controls [4]. To increase the difficulty of the test case, the computational results consider size congested scenarios from the NESTA test systems [97] (case `nesta_case39_epri__api`) which scales the load by 50%, 70%, 80%, 85%, 88%, and 90% of the maximum peak load of the system. To ease comparisons between different settings, the experiments assume that the proposed line switching occurs at time 0.002s. The TSLS models then consider a 4 second horizon, with stability parameters: $T_k = 3s$ and $\overline{\delta} = \frac{\pi}{2}$. The switching routine in Figure 4.3 is implemented in AMPL [100] and uses BONMIN 1.8.4 [101] with default MA27 [102] linear solver for steps 1 and 2. The TSLS optimization models in step 4 use IPOPT 3.12.6 [103] compiled with an advanced linear solver HSL_MA77, designed for large scale systems by using an out-of-core multi-frontal method [102]. By default, the solver converges to local sub-optimal solutions.

The computational studies evaluates TSLS-C model by using generator dispatches as con-

trol variables. For TSLS-T, we further explore two versions of the model: TSLS-G and TSLS-PSS. The TSLS-G model uses generator dispatches as its only control variables, while TSLS-PSS further allows to use PSS controls (in the AVR circuit) apart from generator dispatch. Since time constants T_1 to T_4 (in PSS) are adjustable [104], the major difference between the TSLS-G and TSLS-PSS models is the fact that T_1 to T_4 are constants in TSLS-G and control variables in TSLS-PSS. In the experiments, T_1 and T_2 take their values within $[2,5]$, and T_3 and T_4 within $[0.02, 0.08]$ unless specified otherwise.

Table 4.2: Results for the TSLS-C Model: Dispatch distance (MW/MVAR), Cost Difference ($), and Runtime (sec.).

Congestion (%)	$D^i = 10, r = 1\%, \gamma = 0.2\%$				$D^i = 10, r = 5\%, \gamma = 0.2\%$			
	Line	Dispatch dist.	Cost diff.	Runtime	Line	Dispatch dist.	Cost diff.	Runtime
50	(4,14)	6.48/5.82	0.65 (0.02%)	96.97	(4,14)	32.10/29.00	3.23 (0.12%)	100.99
70	(15,16)^2	14.05/7.57	4.72 (0.11%)	321.89	(16,17)	45.66/37.09	8.58 (0.20%)	124.42
80	(2,25)^2	9.16/4.86	0.23 (0.00%)	198.49	(2,25)^2	28.93/36.63	10.33 (0.20%)	177.98
85	No SW^3	Converge Err.	-	-	No SW^3	Converge Err.	-	-
88	No SW^4	Converge Err.	-	-	No SW^4	Converge Err.	-	-
90	No SW^4	Converge Err.	-	-	No SW^4	Converge Err.	-	-
Congestion (%)	$D^i = 20, r = 1\%, \gamma = 0.2\%$				$D^i = 20, r = 5\%, \gamma = 0.2\%$			
	Line	Dispatch dist.	Cost diff.	Runtime	Line	Dispatch dist.	Cost diff.	Runtime
50	(4,14)	6.48/5.82	0.65 (0.02%)	87.59	(4,14)	32.10/29.00	3.23 (0.12%)	99.37
70	(15,16)^2	14.05/7.57	4.72 (0.11%)	274.34	(16,17)	45.47/37.49	8.58 (0.20%)	117.00
80	(2,25)^2	9.16/4.86	0.23 (0.00%)	253.83	(2,25)^2	25.55/36.29	10.33 (0.20%)	134.24
85	No SW^3	Converge Err.	-	-	No SW^3	Converge Err.	-	-
88	No SW^4	Converge Err.	-	-	No SW^4	Converge Err.	-	-
90	No SW^4	Converge Err.	-	-	No SW^4	Converge Err.	-	-

Table 4.3: Results for the TSLS-G Model: Dispatch distance (MW/MVAR), Cost Difference ($), and Runtime (sec.).

Congestion (%)	$r = 1\%, \gamma = 0.2\%$				$r = 5\%, \gamma = 0.2\%$			
	Line	Dispatch dist.	Cost diff.	Runtime	Line	Dispatch dist.	Cost diff.	Runtime
50	(4,14)	6.48/4.64	0.67 (0.02%)	81.10	(4, 14)	32.24/23.10	3.37 (0.12%)	68.66
70	(16,17)	13.98/7.59	1.84 (0.04%)	198.73	(16,17)	52.52/28.89	8.58 (0.20%)	199.33
80	(16,17)	21.03/6.04	7.93 (0.15%)	96.83	(16,17)	39.24/32.07	10.33 (0.20%)	91.14
85	(2,25)	7.96/5.58	0.70 (0.01%)	79.07	(2,25)	39.94/27.79	3.58 (0.06%)	74.62
88	(16,17)^2	10.96/5.69	3.76 (0.06%)	294.01	(16,17)^2	34.33/28.07	11.93 (0.20%)	249.78
90	No SW^4	Converge Err.	-	-	No SW^4	Converge Err.	-	-

Evaluation of the TSLS-C Model   We first evaluate the TSLS-C model, which uses the simplified classical model for generator. We approximate the transient reactance X'^i for the classical generator by taking the average of the d-axis and q-axis transient reactance, i.e. set to $(X'^i_d + X'^i_q)/2$. Since the classical model assume constant excitation (i.e. E^i_{fd} is constant) and does not involve explicit modeling on damping, we test our routine with two damping parameters: $D^i = 10$ and $D^i = 20$, and report our results for $r = 1\%, \gamma = 0.2\%$ and $r = 5\%, \gamma = 0.2\%$ respectively. Table 4.2 presents the computational results for the TSLS-C model, including the proposed line for switching, the total CPU runtime, and two metrics to measure how much generation resource the model is using to achieve transient stability. The first metric is the

generation differences (in L2 norm, MW/MVAR) with respect to the original steady state:

$$\text{Active power (MW):} \quad \sqrt{\sum_{n \in G} (p_e^i(t|_{t=1}) - p_T^i)^2}$$

$$\text{Reactive power (MVAR):} \quad \sqrt{\sum_{n \in G} (q_e^i(t|_{t=1}) - q_T^i)^2}$$

The second metric is the increased cost (in dollars and percentage) due to the change in dispatch.

When the first line proposed for switching (by Step 2 in Figure 4.3) is not transient stable (i.e. no feasible solution is found), the table indicates the number of lines further being checked, in superscripts after the line results. If none of the lines being proposed are transient stable (i.e. all lines give infeasible solutions), we report 'No SW' and indicate the number of lines being checked in superscripts. If the first line being proposed gives transient stable result (i.e. the first line result in a locally optimal solution), we report the line and skip the number indicating the number of lines being checked.

For 50% congestion settings, the TSLS-C model verifies that the system with small changes to the generator dispatch (with costs $\leq 0.2\%$) ensures that the system is not unstable over the finite horizon considered after the line switching. When the congestion reaches 70%, the TSLS-C model with $r = 1\%$ could not find any stable generation dispatch for the 1st proposed transmission line (16,17). Therefore, the switching routine recommended the second best transmission line (15,16) to perform switching. With $r = 5\%$, the routine successfully find a stable dispatch for line (16,17) to maintain stability. When congestion level increases to 85%, the TSLS-C models could not find any transient-stable dispatches. Since TSLS-C does not consider excitation control circuits (e.g. AVR), the model could fail to find stable solution when congestion level increases and excitation controls become necessary.

Evaluation of the TSLS-G Model Table 4.3 presents the computational results for the TSLS-G model, again with $r = 1\%, \gamma = 0.2\%$ and $r = 5\%, \gamma = 0.2\%$. With excitation control circuits implemented in TSLS-G, the model manages to find transient stable solutions up to 85% congestion, indicating excitation control could become necessary for congested network. When the congestion reaches 88%, the TSLS-G model could not find any stable generation dispatch within the 1%/5% generation limit, and therefore, the switching routine recommended the second best transmission line (16,17) to perform switching. When congestion level increases to 90%, the TSLS-G model could not find any transient-stable dispatches.

Solutions of the TSLS-G model are only stable in the fixed finite-time horizon (i.e. short term transient stable) and may become unstable in later time periods (e.g. oscillation unstable). To verify the long-term stability of the TSLS-G solutions, a transient simulation on Power-World simulator (ver. 17) [7] (at 10^{-3} sec. step size) was run on the 85% and 88% congestion case. We initialize the dispatch of the optimization model on opening line (2,25) and (16,17) respectively for these two cases. Figure 4.4 and 4.5 present the results. Figure 4.4 indicates an increasing magnitude in rotor angle oscillations, due to undamped excitation controls. For Figure 4.5, we observe the system eventually becomes unstable at about 11 seconds. Clearly, using only generator dispatch as control variables are insufficient to ensure long-term stability.
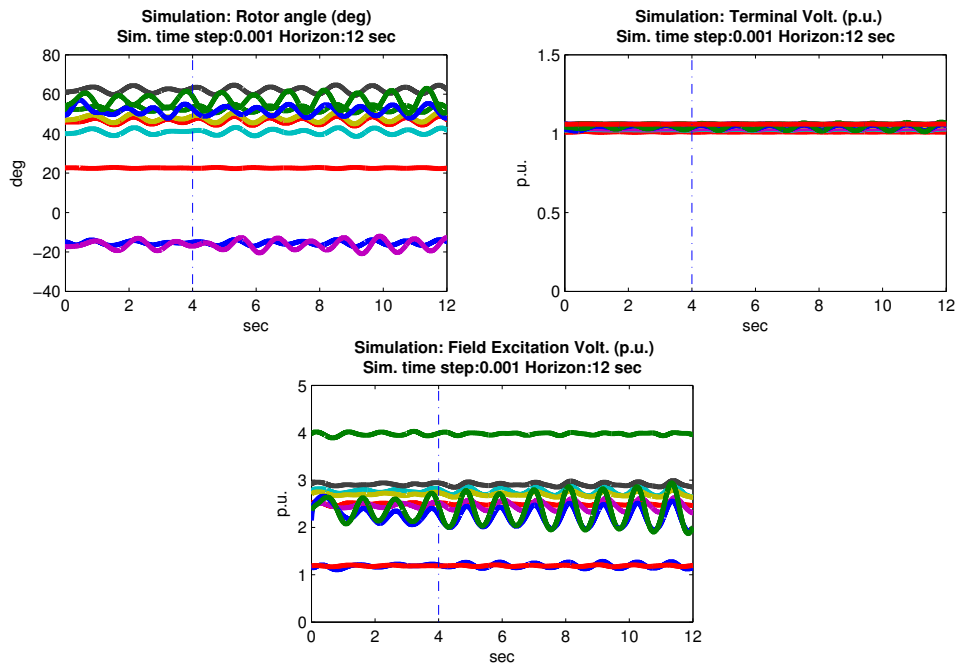
Figure 4.4: TSLS-G Model: Rotor angles (deg), and terminal voltage (p.u.), and excitation field voltage (p.u.) for 85% congestion level ($r = 1\%, \gamma = 0.2\%$) on opening line (2,25). Each line represents a generator.
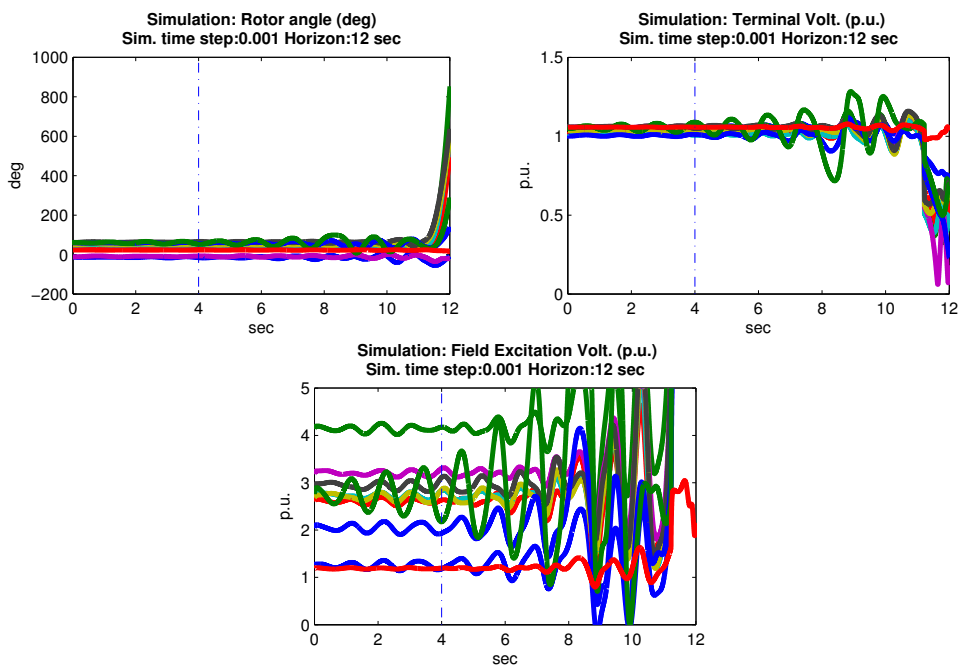
Figure 4.5: TSLS-G Model: Rotor angles (deg), and terminal voltage (p.u.), and excitation field voltage (p.u.) for 88% congestion level ($r = 1\%, \gamma = 0.2\%$) on opening line (16,17). Each line represents a generator.

This leads us to focus on the TSLS-PSS model.

Table 4.4: Results for the TSLS-PSS Model: Dispatch distance (MW/MVAR), Cost Difference ($), and Runtime (sec.).

Congestion (%)	No dispatch change: $r = 0\%, \gamma = 0.2\%$				$r = 1\%, \gamma = 0.2\%$			
	Line	Dispatch dist.	Cost diff.	Runtime	Line	Dispatch dist.	Cost diff.	Runtime
50	(4,14)	0.00/0.00	0.00 (0.00%)	1206.84	(4,14)	6.67/6.65	0.82 (0.03%)	493.14
70	(16,17)	0.00/0.00	0.00 (0.00%)	496.97	(16,17)	14.15/7.53	1.89 (0.04%)	1206.73
80	(16,17)	0.00/0.00	0.01(0.00%)	511.07	(16,17)	20.21/7.89	7.52 (0.15%)	185.18
85	(2,25)	0.00/0.00	0.00 (0.00%)	239.08	(2,25)	7.95/5.56	0.70 (0.01%)	102.82
88	(2,25)	0.00/0.00	0.00 (0.00%)	417.57	(2,25)	2.64/7.59	0.77 (0.01%)	289.64
90	No SW[4]	Converge Err.	-	-	No SW[4]	Converge Err.	-	-

Congestion (%)	No dispatch change: $r = 5\%, \gamma = 0.2\%$			
	Line	Dispatch dist.	Cost diff.	Runtime
50	(4,14)	33.23/29.12	4.34 (0.16%)	195.98
70	(16,17)	52.51/28.89	8.58 (0.20%)	689.44
80	(16,17)	39.17/33.57	10.33 (0.20%)	195.87
85	(2,25)	37.70/27.76	3.48 (0.06%)	186.46
88	(2,25)	12.01/39.60	3.64 (0.06%)	191.51
90	No SW[4]	Converge Err.	-	-

Evaluation of the TSLS-PSS Model   Table 4.4 presents the results of the TSLS-PSS model, with $r = 0\%$ (i.e. no dispatch change), $r = 1\%$, and $r = 5\%$, and with $\gamma = 0.2\%$. During implementation, a direct implementation of $r = 0$, e.g. by adding equality constraints to enforce $p_e^i(t|_{t=1}) = p_T^i$, may lead of convergence issues in IPOPT. To avoid numerical convergence issues, we alternatively implement:

$$|p_e^i(t|_{t=1}) - p_T^i| \leq \varepsilon |p_T^i|$$
$$|q_e^i(t|_{t=1}) - q_T^i| \leq \varepsilon |q_T^i|$$

where ε is a small enough tolerance. In our model, we set ε to 10^{-5}.

Once again, the change in generator dispatch is minimal and the optimization model ensures the network is stable over the finite horizon for the recommended line switching and all congestion levels, except 90%. The simulation results, initialized with the AVR damping control, are shown in Figures 4.6 for congestion levels at 85% and 88% at $r = 0\%$, i.e. without any generation dispatch changes. The figure shows an improved damping of rotor angles and stable voltage magnitudes, demonstrating the benefits of the model. Controlling the exciter/stabilizer settings is thus critical in using transmission line switching in highly congested situations, in particular in maintaining small-signal stability, and is a promising avenue for managing congestion.

Time horizon: 4 seconds vs 12 seconds   One challenging parameter to tune in the TSLS models is the required time horizon T for optimization. A longer time T would allow the model to reason on the swing dynamics longer, resulting in: a) better optimization quality in damping for oscillation stability, and b) could guarantee transient stability for a longer time period. On the other hand, a longer time horizon eventually also increases the model size
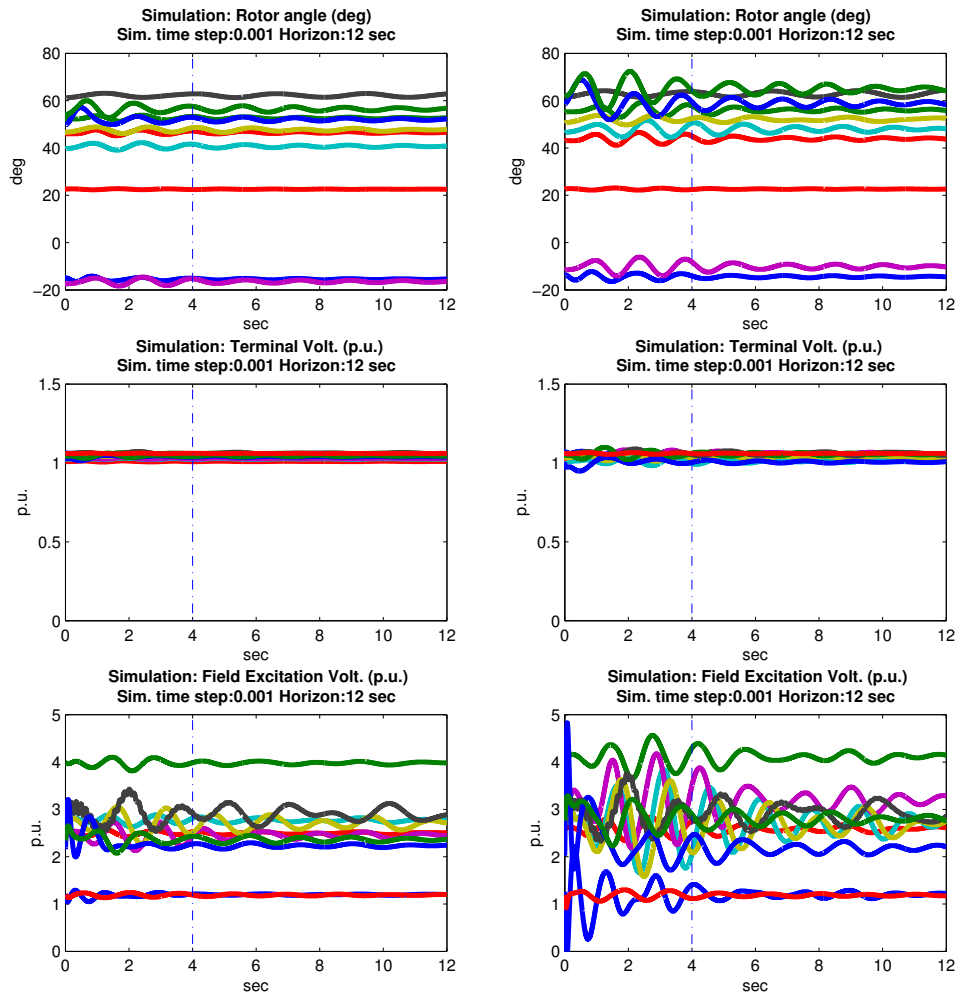
Figure 4.6: TSLS-PSS Model: Rotor angles (deg), terminal voltage (p.u.), and excitation field voltage (p.u.) with no dispatch change (i.e. $r = 0\%$) for opening line (2,25). Left: congestion level 85%, right: congestion level 88%. Each line represents a generator.

and computational runtime. Table 4.5 presents the results of the TSLS-PSS model with again $r = 0\%, 1\%$, and 5%, but now optimized on a time horizon T of 12 seconds. For all of the cases, the model runs drastically slower than the model with a 4 seconds of horizon. For 50% and 70% congestion cases with tight dispatch limit ($r = 0\%$ or $r = 1\%$), the model even fails to converge to a stable solution within a time limit of 1 hour for the first/second proposed transmission line. For $r = 0\%$, the routine barely manages to find a transient stable solution for the third proposed line.

Figure 4.7 shows the simulated results for congestion levels at 88% with $r = 1\%$ on the TSLS-PSS model (with excitation controls). Plots on the left are optimized with a horizon of $T = 4$ seconds, while plots on the right are optimized with $T = 12$ seconds. Both cases are simulated in PowerWorld for up to 12 seconds of simulation time. For $T = 4$ seconds, we notice two unexpected phenomenon.

First, high-frequency oscillations appear in the excitation control voltage plot. Since Pow-

Table 4.5: Results for the TSLS-PSS Model with $T = 12$ seconds: Dispatch distance (MW/M-VAR), Cost Difference ($), and Runtime (sec.).

Congestion (%)	No dispatch change: $r = 0\%, \gamma = 0.2\%$				$r = 1\%, \gamma = 0.2\%$			
	Line	Dispatch dist.	Cost diff.	Runtime	Line	Dispatch dist.	Cost diff.	Runtime
50	$(16,17)^3$	0.00/0.00	0.00 (0.00%)	16893.53	No SW[3]	Time Limit	-	-
70	$(7,8)^3$	0.00/0.00	0.00 (0.00%)	19497.61	No SW[3]	Time Limit	-	-
80	(16,17)	0.00/0.00	0.00 (0.00%)	2923.28	(16,17)	18.15/7.97	6.72 (0.13%)	2457.50
85	(2,25)	0.00/0.00	0.00 (0.00%)	777.26	(2,25)	7.95/5.56	0.70 (0.01%)	734.02
88	(2,25)	0.00/0.00	0.00 (0.00%)	2493.72	(2,25)	2.06/6.73	0.81 (0.01%)	2605.59
90	No SW[4]	Time Limit	-	-	No SW[4]	Time Limit	-	-

Congestion (%)	No dispatch change: $r = 5\%, \gamma = 0.2\%$			
	Line	Dispatch dist.	Cost diff.	Runtime
50	(4,14)	33.11/28.52	3.97 (0.14%)	1105.76
70	(16,17)	52.51/28.89	8.58 (0.20%)	4545.76
80	(16,17)	39.15/30.39	10.33 (0.20%)	3374.95
85	(2,25)	39.31/27.75	3.56 (0.06%)	815.53
88	(2,25)	10.15/29.42	3.82 (0.06%)	3125.51
90	No SW[4]	Time Limit	-	-

erWorld is known to have potential numerical issues (often exhibits as high frequency oscillations) when time constant parameters are too small or gain parameters are too large [105, 106], we further decrease the integration step size of the simulation routine from 10^{-3}s to 10^{-4}s and re-run the simulation. We observe the fast-oscillations in the excitation voltage control signals disappear (Figure 4.8), suggesting numerical stability issues from the simulator PowerWorld. Note that these difficulties were also encountered in our case studies when the lead-lag ratios T_1/T_3 or T_2/T_4 were large.

Second, one excitation control signal appears to have increasing oscillations in amplitude (see right plot of Figure 4.8), suggesting potential oscillation stability issues in the corresponding generator. Note that this issue does not happen at $r = 0\%$. Since the optimization routine only optimizes for 4 seconds, one possible reason is that the rotor angles with $r = 1\%$ are in fact damping better in terms of rotor angle than $r = 0\%$, when considered with only 4 seconds horizon, by co-optimizing the generator dispatch and PSS together. However, as the generator is a heavier generator (with larger inertia value) comparing to the other generators, optimizing with 4 seconds could only barely reason the rotor/excitation control swings with less than 2 cycles/periods. Optimizing at a longer horizon (e.g. 12 seconds) allows more swing cycles to be considered, and remove the issue.

Optimization Versus Simulation   It is interesting to compare the results of the TSLS-PSS model with a PowerWorld [7] simulation on the same case studies, as the TSLS-PSS uses a conservative approximation of the limiters and employs a trapezoidal discretization with fixed steps. We validate the TSLS-PSS model on coarser and fine discretization steps ranging from 0.160s to 0.040s with a 4 seconds of horizon. Transient simulations in PowerWorld are run with the second order Runge-Kutta integration method (RK) with 10^{-3} second step size. To avoid the risks of validating against erroneous simulation results on PowerWorld (e.g. numerical errors with high frequency oscillating swings), we added a constraint in the model to restrict the max ratio to 60 for this validation study. Table 4.6 updates Table 4.4 with the additional
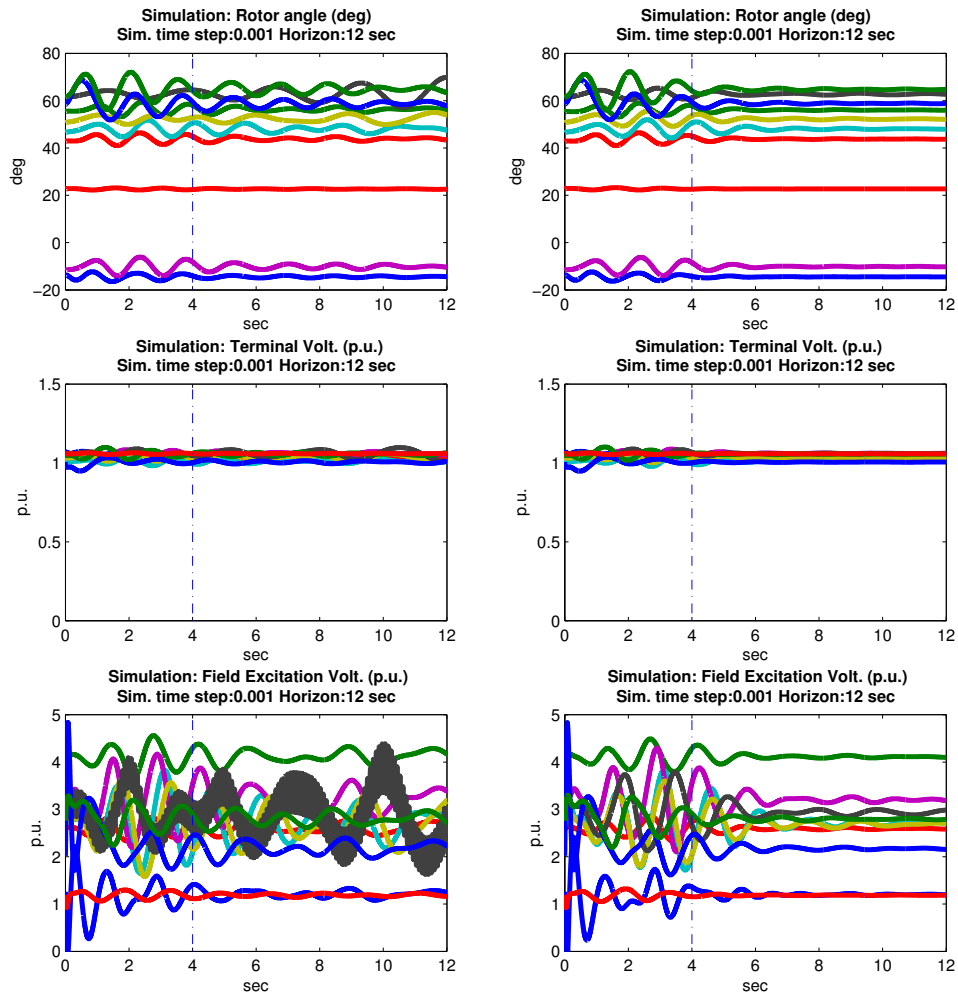
Figure 4.7: TSLS-PSS Model: Rotor angles (deg), terminal voltage (p.u.), and excitation field voltage (p.u.) with 1% dispatch change (i.e. $r = 1\%$) on 88% congestion case for opening line (2,25). Left: 4 seconds horizon, right: 12 seconds horizon. Each line represents a generator.

restriction and the results are similar in nature when comparing to the earlier studies.

We are now in a position to compare the TSLS-PSS model and the simulation results seeded with the generator dispatch and AVR values found by the optimization model. The results are given in Table 4.7 which, for each time step, reports the number of variables in the optimization, the CPU runtime (sec.), the cost difference (in %), and a metric to measure the accuracy of the optimization results with respect to the simulation outcomes. Since the rotor angles solutions obtained by optimization are on a coarser time-grid when comparing to simulation, we use linear interpolation method to transform the rotor angle time series (of all generators) to the same time scale used by PowerWorld simulation for comparison purposes. The accuracy metric is then expressed in terms of $\delta_s^n(t)$ and $\delta_o^n(t)$, which denote the rotor angle obtained by the simulation and the interpolated rotor angle obtained by optimization for generator n at the simulated time $t \in T^s$ respectively. It computes the average errors (L2 norm)
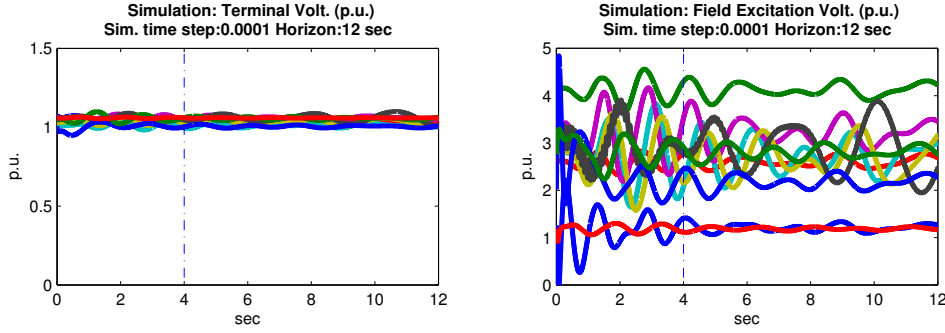
Figure 4.8: TSLS-PSS Model: terminal voltage (p.u.) and excitation field voltage (p.u.) with 1% dispatch change for opening line (2,25) at congestion level 88%. Increased simulation time step to 10^{-4}. Each line represents a generator.

Table 4.6: Results for the Range-Restricted TSLS-PSS Model: Dispatch distance (MW/M-VAR), Cost Difference (\$), and Runtime (sec.).

Congestion	No dispatch change: $r = 0\%, \gamma = 0.2\%$				$r = 1\%, \gamma = 0.2\%$			
(%)	Line	Dispatch dist.	Cost diff.	Runtime	Line	Dispatch dist.	Cost diff.	Runtime
50	(4,14)	0.00/0.00	0.00 (0.00%)	712.41	(4,14)	6.52/7.03	0.78 (0.03%)	205.96
70	(16,17)	0.00/0.00	0.00 (0.00%)	169.03	(16,17)	14.15/7.53	1.89 (0.04%)	553.96
80	(16,17)	0.00/0.00	0.01 (0.00%)	350.82	(16,17)	20.21/7.89	7.52 (0.15%)	115.63
85	(2,25)	0.00/0.00	0.00 (0.00%)	117.08	(2,25)	7.95/5.56	0.70 (0.01%)	142.74
88	(2,25)	0.00/0.00	0.00 (0.00%)	616.84	(2,25)	2.77/8.39	0.63 (0.01%)	151.33
90	No SW[4]	Converge Err.	-	-	No SW[4]	Time Limit	-	-

Congestion	No dispatch change: $r = 5\%, \gamma = 0.2\%$			
(%)	Line	Dispatch dist.	Cost diff.	Runtime
50	(4,14)	32.57/26.68	3.63 (0.13%)	127.08
70	(16,17)	52.51/28.89	8.58 (0.20%)	347.14
80	(16,17)	39.17/33.57	10.33 (0.20%)	123.67
85	(2,25)	34.97/27.80	3.36 (0.06%)	161.65
88	(2,25)	11.81/39.90	3.52 (0.06%)	189.75
90	No SW[4]	Time Limit	-	-

on the rotor angles (deg) by the following equation:

$$\frac{1}{|G||T^s|} \sum_{n \in G} \sqrt{\sum_{t \in T^s} [\delta_s^n(t) - \delta_o^n(t)]^2}$$

This accuracy metric represents the average errors of rotor angles in degrees, per generator machine and time point. Figure 4.9 further shows the error plots reporting the difference between optimization and simulation on rotor angles (deg.), generator terminal voltage (p.u.), and excitation control field voltage (p.u.) for the 88% cases, ranging from coarse discretization to fine discretization.

Table 4.7 and Figure 4.9 show the TSLS-PSS model has high accuracy with respect to simulation, with an average error in the scale of 10^{-3} deg. The finer discretization step we used for trapezoidal discretization, the smaller error we obtained at the cost of increasing computational runtime. The error functions further show finer discretization decreases the worst-case error to

Table 4.7: Runtime (sec.), Generation cost difference (%), and average errors (deg)

Time step (sec.)	Model var. num.	Dispatch Distance: $r = 5\%$, Cost distance: $\gamma = 0.2\%$										
		70%			80%			85%			88%		
		Error	Cost diff.	Runtime	Error	Cost diff.	Runtime	Error	Cost diff.	Runtime	Error	Cost diff.	Runtime
0.160	14,470	0.005	0.2%	195.30	0.006	0.2%	70.61	0.003	0.06%	46.00	0.008	0.06%	56.18
0.125	18,243	0.003	0.2%	216.82	0.003	0.2%	94.90	0.002	0.06%	114.46	0.004	0.06%	90.82
0.080	27,945	0.001	0.2%	347.14	0.001	0.2%	123.67	0.001	0.06%	161.65	0.001	0.06%	189.75
0.040	54,895	0.001	0.2%	1248.46	0.001	0.2%	1047.25	0.001	0.06%	508.72	0.002	0.06%	587.56

Time step (sec.)	Model var. num.	Dispatch Distance: $r = 1\%$, Cost distance: $\gamma = 0.2\%$										
		70%			80%			85%			88%		
		Error	Cost diff.	Runtime	Error	Cost diff.	Runtime	Error	Cost diff.	Runtime	Error	Cost diff.	Runtime
0.160	14,470	0.005	0.04%	167.52	0.006	0.15%	43.23	0.003	0.01%	61.71	0.009	0.01%	42.06
0.125	18,243	0.003	0.04%	217.29	0.003	0.15%	66.08	0.002	0.01%	72.75	0.005	0.01%	60.74
0.080	27,945	0.001	0.04%	553.96	0.001	0.15%	115.63	0.001	0.01%	142.74	0.002	0.01%	151.33
0.040	54,895	0.001	0.04%	1668.45	0.001	0.15%	1079.93	0.001	0.01%	275.79	0.003	0.01%	432.34

Time step (sec.)	Model var. num.	Dispatch Distance: $r = 0\%$, Cost distance: $\gamma = 0.2\%$										
		70%			80%			85%			88%		
		Error	Cost diff.	Runtime	Error	Cost diff.	Runtime	Error	Cost diff.	Runtime	Error	Cost diff.	Runtime
0.160	14,470	0.005	0.00%	108.83	0.006	0.00%	55.80	0.003	0.00%	64.27	0.009	0.00%	106.95
0.125	18,243	0.003	0.00%	810.23	0.003	0.00%	126.79	0.002	0.00%	59.04	0.005	0.00%	389.87
0.080	27,945	0.001	0.00%	169.03	0.001	0.00%	350.82	0.001	0.00%	117.08	0.002	0.00%	616.84
0.040	54,895	0.001	0.00%	1113.11	0.001	0.00%	1540.50	0.001	0.00%	203.10	0.003	0.00%	4979.84

2 deg in a 4 seconds horizon.

One notable phenomenon for finite difference discretization is that the error accumulates when time horizon increases, with more error accumulated at later time steps. This phenomenon could be observed from the rotor angle plots in Figure 4.9, with larger errors at the end of the time horizon. One question at hand is how large the error would accumulate when the time horizon increases for optimization. We present the simulation result on the simulation study with a 12 seconds horizon in Table 4.8, for 80%, 85%, and 88% congestion cases with $r = 0\%, 1\%$, and 5% and a fixed discretization step size of 0.080 seconds. Figure 4.10 further shows the error plots for the three congestion cases with $r = 0\%$. The results show we still manage to control the average errors in the scale of 10^{-3} deg, with the worst-case errors in less than 2 deg in a 12 seconds horizon.

Table 4.8: Runtime (sec.), Generation cost difference (%), and average errors (deg) for 12 seconds horizon optimization at 0.080 seconds time step discretization

Dispatch dist. %	Model var. num.	Dispatch Distance: $r = 0\%, 1\%, 5\%$, Cost distance: $\gamma = 0.2\%$								
		80%			85%			88%		
		Error	Cost diff.	Runtime	Error	Cost diff.	Runtime	Error	Cost diff.	Runtime
5%	81,848	0.001	0.20%	3374.95	0.000	0.06%	815.53	0.001	0.06%	3125.51
1%	81,848	0.001	0.13%	2457.50	0.000	0.01%	734.02	0.001	0.01%	2605.59
0%	81,848	0.001	0.00%	2923.28	0.000	0.00%	777.26	0.001	0.00%	2493.72

Extension to other benchmark systems   This section further demonstrates how we readily apply our techniques on transient-stable line switching to other larger benchmark systems.

Figure 4.9: Error functions on rotor angles (deg), terminal voltage (p.u.), and excitation controls (p.u.) for 88% congestion, with $r = 0\%$ and $\gamma = 0.2\%$. Discretization steps size (top to bottom): 0.160s, 0.125s, 0.080s, and 0.040s. Each line represents a generator.

We use the Simplified 14-Generator Model of the South East Australian Power System [98] from the IEEE PES Task Force on Benchmark Systems for Stability Controls as an example.

The benchmark is a 50Hz system consists of: 14 aggregated generators, 59 buses, 5 Static VAR Compensators (SVC), and 9 switched shunt capacitor/reactor banks. The benchmark also contains detailed dynamic models and data for transient stability studies. One main characteristics of the network is that it consists of many parallel identical transmission lines and parallel identical transformers. Since this work primarily focus on transmission line switchings only, we decide to keep all parallel lines as separate lines (without reduction/aggregation). On the other hand, we aggregate all parallel transformers in the network for simplicity, by reducing to equivalent transformers according to the benchmark data. We use the peak load and generation data from the benchmark report, i.e. case 3 in the report, to evaluate our model/algorithms in congested scenarios. Similar to the IEEE 39-bus system, we vary the loads by 70%, 90%, 100%, 110%, and 115% from the peak load data. We model the SVC as flexible reactive power sources, with reactive power bounded by the maximum and minimum values indicated in the
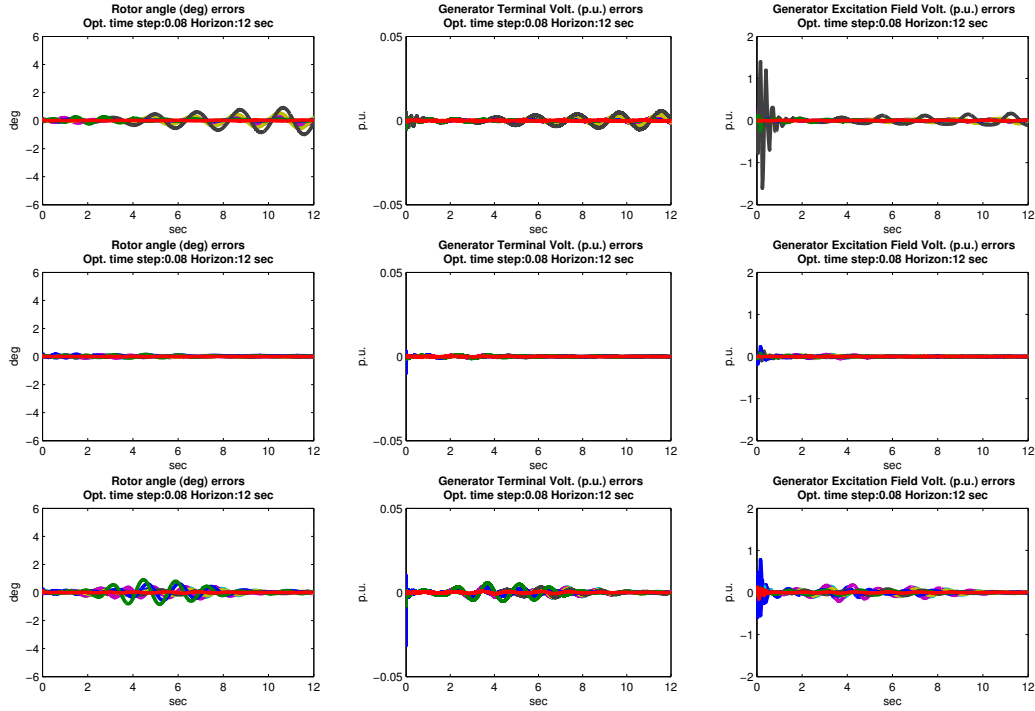
Figure 4.10: Error functions on rotor angles (deg), terminal voltage (p.u.), and excitation controls (p.u.) for (top to bottom) 80%, 85%, and 88% congestion, with $r = 0\%$ and $\gamma = 0.2\%$, discretization steps size of 0.080s, and a time horizon of 12 seconds. Each line represents a generator.

data report. In other words, SVC are also adjustable resources in our model for maintaining stability. For switched shunt capacitor/reactor banks settings and transformer tap/turn ratios settings, we again use the data in the report corresponding to the peak load situation, i.e. case 3 in the report. Note that these two parameters are not flexible resources in our experimental settings, but should be straightforward to generalize them to be flexible. To implement SVC and switched shunt capacitor/reactor banks, there are two approaches. One approach is to treat these devices as generators with only reactive power capabilities, and set the active power p_e to zero and ignore the generator model (i.e. Two-axis model/swing model) on these generators. Another approach we implemented is to directly extended our model to handle these devices. We first extend (4.38) to:

$$\sum_{m \in G(n)} p_e^m(t) - \sum_{m \in O(n)} p_l^m - [V^n(t)]^2 g_s^n = \sum_{m \in N(n)} p^{nm}(t)$$

$$\sum_{m \in G(n)} q_e^m(t) - \sum_{m \in O(n)} q_l^m + [V^n(t)]^2 b_s^n + \sum_{m \in S(n)} q_s^m + \sum_{m \in C(n)} q_c^m = \sum_{m \in N(n)} q^{nm}(t)$$

where $S(n)$ and $C(n)$ denote the set of SVC devices and switched shunt capacitor/reactor banks, and q_s^m and q_c^m denote the reactive power generated/absorbed by the corresponding SVC device and capacitor/reactor bank. Since SVC devices are flexible, we need to add proper

maximum/minimum bounds:

$$\underline{q_s^m} \leq q_s^m \leq \overline{q_s^m}$$

and the flexible region constraints:

$$|q_s^m - q_{sT}^m| \leq r|q_{sT}^m|$$

where q_{sT}^m denotes the reactive power set-points of SVC devices in the steady-state solution (i.e. Step 1 of our transient stable routine in Figure 4.3), and r is the tolerance parameter we had introduced and used in previous sections.

The benchmark report mainly uses the 6th order generator model (except two generator machines with the 5th order model) for modeling transient dynamics, together with two different excitation systems (ST1A and AC1A) and four different PSS stabilizing system circuits. Since our generator model is a 4th order model and our excitation and PSS stabilizing system are more simplified (lower order) than the benchmark data, we only use parts of the data, by mainly ignoring higher-order parameters, in order to fit into our transient model for evaluation. On cases where the lower-order parameters are missing, we approximate these parameters by using higher-order data. Table 4.9, 4.10, and 4.11 report the parameters for our 4th order two-axis synchronous generator model, the excitation system (SEXS_PTI), and the stabilizing system (STAB1) respectively. Since the benchmark report does not provide generator costs data/function parameters, we assume the generation costs of all generators follow the common generator function $c()$,

$$c(n, p_g^n) = c_2^n[p_g^n]^2 + c_1^n p_g^n + c_0^n, \ \ n \in G$$

where p_g^n denotes the active power generated by generator n and c_2^n, c_1^n, and c_0^n denotes the cost coefficient for generator n. For simplicity, we assume c_2^n and c_0^n are both 0 and reduce $c(n, p_g^n)$ to linear. Table 4.12 shows the cost parameters for our experimental study.

Table 4.9: Two-axis synchronous generator machine model parameters for the 14-Generator Model benchmark (in system 100 MVA base)

Gen. Machine	H	X_d'	X_q'	X_d	X_q	T_{do}'	T_{qo}'
101	143.986	0.006	0.010	0.028	0.016	8.50	1.50
201	128.006	0.007	0.017	0.045	0.044	8.50	0.30
202	77.784	0.011	0.018	0.079	0.076	4.50	1.50
204	128.006	0.007	0.017	0.045	0.044	8.50	0.30
203	57.782	0.013	0.018	0.103	0.076	5.00	2.00
301	149.341	0.006	0.016	0.051	0.028	7.50	0.85
302	62.216	0.014	0.045	0.113	0.101	7.50	1.50
402	29.997	0.030	0.055	0.190	0.180	6.50	1.40
404	79.992	0.016	0.038	0.110	0.070	9.00	1.40
403	46.218	0.017	0.023	0.129	0.096	5.00	2.00
401	46.218	0.017	0.023	0.129	0.096	5.00	2.00
501	23.331	0.045	0.120	0.330	0.255	7.50	1.50
502	40.000	0.030	0.080	0.200	0.150	7.50	3.00
503	75.015	0.025	0.035	0.230	0.200	5.00	1.00

Table 4.13 presents the results of the TSLS-PSS model on the 14-Generator benchmark,

Table 4.10: Excitation parameters for the 14-Generator Model benchmark

Gen. Machine	K_a	$T_f d$	T_A	T_B	$\overline{E_{fd}}$	$\underline{E_{fd}}$
101	200	0.100	2.500	13.250	5.5	-5.5
201	400	0.020	0.500	1.120	5.5	-5.5
202	400	0.020	0.000	0.000	5.5	-5.5
204	400	0.020	0.500	1.120	5.5	-5.5
203	300	0.010	0.350	0.700	5.5	-5.5
301	400	0.050	1.140	6.420	5.5	-5.5
302	200	0.050	0.000	0.000	5.5	-5.5
402	300	0.050	1.520	9.800	5.5	-5.5
404	250	0.200	0.136	0.023	5.5	-5.5
403	300	0.010	0.350	0.700	5.5	-5.5
401	300	0.100	4.000	40.000	5.5	-5.5
501	1000	0.040	0.000	0.000	5.5	-5.5
502	400	0.500	1.400	16.000	5.5	-5.5
503	300	0.010	0.200	0.800	5.5	-5.5

Table 4.11: Power Systems Stabilizer (PSS) parameters for the 14-Generator Model benchmark

Gen. Machine	K_s	T_w	T_1	T_3	T_2	T_4	$\overline{V_s}$	$\underline{V_s}$
101	2.884	7.5	0.373	0.007	0.038	0.007	1	-1
201	1.042	7.5	0.128	0.007	0.006	0.007	1	-1
202	1.258	7.5	0.286	0.007	0.111	0.007	1	-1
204	1.249	7.5	0.010	0.007	0.000	0.000	1	-1
203	1.930	7.5	0.071	0.007	0.029	0.007	1	-1
301	1.758	7.5	0.168	0.007	0.012	0.007	1	-1
302	2.515	7.5	0.050	0.007	0.000	0.000	1	-1
402	3.525	7.5	0.278	0.007	0.100	0.007	1	-1
404	2.273	7.5	0.115	0.007	0.006	0.007	1	-1
403	2.667	7.5	0.091	0.007	0.002	0.007	1	-1
401	3.012	7.5	0.208	0.007	0.208	0.007	1	-1
501	4.388	7.5	0.033	0.007	0.000	0.000	1	-1
502	4.410	7.5	0.500	0.007	0.059	0.007	1	-1
503	2.669	7.5	0.200	0.350	0.187	0.067	1	-1

with $r = 0\%$ (i.e. no dispatch change, subject to ε tolerance), $r = 1\%$, $r = 5\%$, and $r = 10\%$, and with $\gamma = 0.2\%$. Once again, the change in generator dispatch is minimal and the optimization model ensures the network is transient stable over the 4 seconds finite horizon for switching the 1st recommended line at all congestion levels with a slightly longer runtime, except 70% cases. Since the excitation and PSS parameters are specifically tuned (by the benchmark report) for peak loads, switching a line may not be transient stable when loads are deviated from the target settings. With a slightly larger dispatch tolerance, TSLS-PSS manages to find transient stable solutions. Figure 4.11 further shows the optimization results for the TSLS-G model (top row) and the TSLS-PSS mode (bottom row), on the 115% congestion cases, with $r = 10\%$ and $\gamma = 0.2\%$. Similar to the IEEE 39-bus test system, TSLS-G model again fails to maintain oscillation stability (as seen from the excitation control plot), while TSLS-PSS further maintain oscillation stability by adjusting PSS controls.
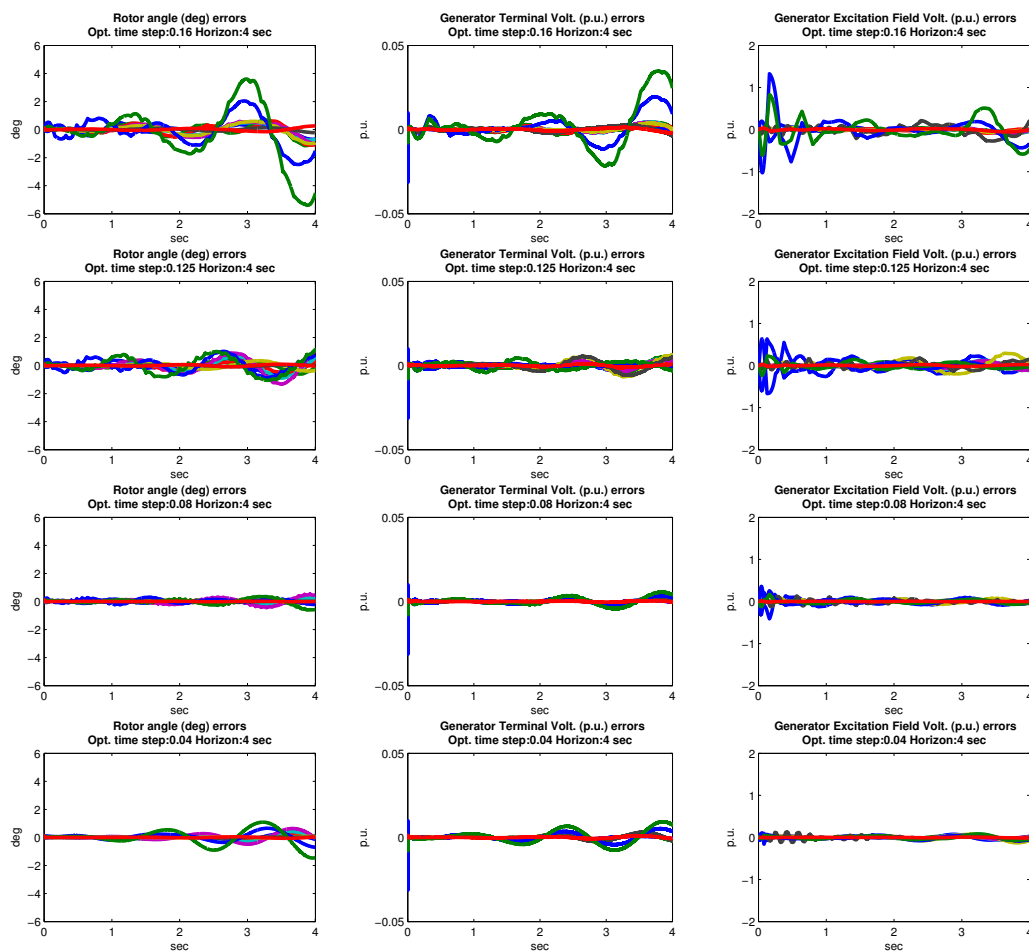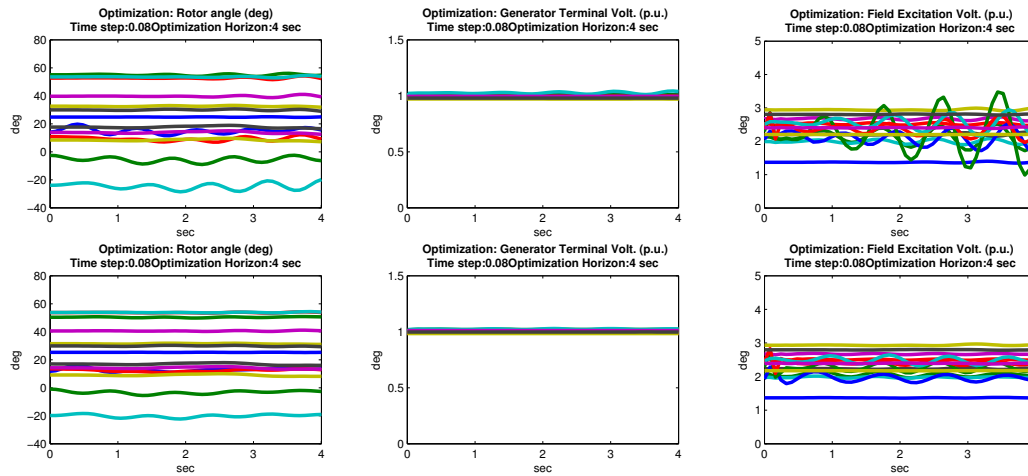
Figure 4.11: Optimization solutions on rotor angles (deg), terminal voltage (p.u.), and excitation controls (p.u.) for the 115% congestion case, with $r = 10\%$ and $\gamma = 0.2\%$, discretization steps size of 0.080s, and a time horizon of 4 seconds. Top: TSLS-G model, Bottom: TSLS-PSS model. Each line represents a generator.

Table 4.12: Generation cost parameters for the 14-Generator Model benchmark

Gen. Machine	c_0	c_1	c_2
101	0	0.294	0
201	0	0.942	0
202	0	0.947	0
204	0	0.551	0
203	0	0.635	0
301	0	1.165	0
302	0	0.294	0
402	0	0.735	0
404	0	0.867	0
403	0	1.572	0
401	0	0.942	0
501	0	0.735	0
502	0	0.867	0
503	0	0.735	0

Table 4.13: Results for TSLS-PSS Model on the 14-Generator Model: Dispatch distance (MW/MVAR), Cost Difference ($), and Runtime (sec.).

Congestion	No dispatch change: $r = 0\%, \gamma = 0.2\%$				$r = 1\%, \gamma = 0.2\%$			
(%)	Line	Dispatch dist.	Cost diff.	Runtime	Line	Dispatch dist.	Cost diff.	Runtime
70	$(307,308)^2$	0.02/0.00	0.02 (0.00%)	5197.02	$(307,308)^2$	27.03/8.76	21.62 (0.19%)	3885.45
90	(408,410)	0.03/0.00	0.01 (0.00%)	176.26	(408,410)	36.59/8.48	10.75 (0.07%)	448.11
100	(411,412)	0.05/0.01	0.02 (0.00%)	1041.86	(411,412)	44.98/10.09	12.29 (0.06%)	273.96
110	(405,408)	0.03/0.02	0.01 (0.00%)	192.84	(405,408)	30.27/15.91	9.46 (0.04%)	331.32
115	(405,408)	0.03/0.02	0.01 (0.00%)	203.14	(405,408)	31.17/18.98	10.88 (0.05%)	2137.22

Congestion	$r = 5\%, \gamma = 0.2\%$				$r = 10\%, \gamma = 0.2\%$			
(%)	Line	Dispatch dist.	Cost diff.	Runtime	Line	Dispatch dist.	Cost diff.	Runtime
70	(507,508)	95.63/47.58	11.80 (0.10%)	784.51	(507,508)	179.62/88.69	22.02 (0.20%)	314.10
90	(408,410)	156.88/44.19	32.95 (0.20%)	373.97	(408,410)	218.52/101.25	32.95 (0.20%)	348.24
100	(411,412)	169.75/65.72	38.57 (0.17%)	394.00	(411,412)	174.32/133.19	38.57 (0.20%)	266.77
110	(405,408)	121.51/54.27	44.54 (0.20%)	419.80	(405,408)	87.49/64.74	44.54 (0.20%)	296.32
115	(405,408)	104.50/62.72	47.63 (0.20%)	528.44	(405,408)	103.38/97.65	47.63 (0.20%)	2643.55

Dynamic Compressor Optimization in Natural Gas Pipeline Systems

The growing dependence of electric power systems on gas-fired generators to balance fluctuating and intermittent production by renewable energy sources has increased the variation and volume of flows withdrawn from natural gas transmission pipelines. Adapting pipeline operations to maintain efficiency and security under these dynamic conditions requires optimization methods accounting for substantial intra-day transients. Efficient methods in practice are required to respond to potential rapid change in generation dispatch.

Our third piece of work to maintain system stability will be on the natural gas pipeline system, now being coupled and influenced drastically by the electric power systems. This chapter presents a computationally efficient method for minimizing gas compression costs under dynamic conditions where deliveries to customers, including natural gas generators, are described by time-dependent mass flows. The optimization method uses a simplified representation of gas flow physics, provides a choice of discretization schemes in time and space, and exploits a two-stage approach to minimize energy costs and ensure smooth and physically meaningful solutions. The resulting large-scale nonlinear programs are solved using an interior-point method. The optimization scheme is validated by comparing the solutions with an integration of the dynamic equations using an adaptive time-stepping differential equation solver, as well as a different, recently proposed optimal control scheme. The comparison shows that solutions to the discretized problem are feasible for the continuous problem and also practical from an operational standpoint. The results also indicate that our scheme produces at least an order of magnitude reduction in computation time relative to the state-of-the-art and scales to large gas transmission networks with more than 6000 kilometers of total pipeline.

5.1 Overview

In recent decades, the increasing penetration of renewable energy sources into electric power grids and the growth in availability of natural gas have driven installation of gas-fired electric power plants. These plants were installed to meet most of the demand for new generating capacity and reserves [107, 108, 109]. Gas-fired generators often go online and shut down several times a day, and are able to rapidly adjust their production. This capability allows them to be attractive resources for balancing the fluctuation of renewable energy sources such as

wind and solar [110, 111, 80].

Historically, withdrawals from natural gas transmission systems came from utilities and industrial consumers. Their usages are predictable and exhibit low variation in demand [80]. These withdrawals are traded using day-ahead contracts for fixed deliveries and implicitly assume that injections and withdrawals remain nearly constant [112]. As a result, optimization approaches for natural gas transmission systems have traditionally restricted attention to steady-state models [113, 114].

However, the growing use of gas-fired power plants for electricity generation [109, 115] has prompted concerns in both industry sectors [111]. The integration of electric and gas systems may result in gas-fired generator dispatch and commitment schedules that create substantial intra-day fluctuations in high-volume gas flows. The physics underlying these fuctuations cannot be adequately captured by steady-state models [29, 30], raising challenges highlighted in recent studies [116]. To enable natural gas systems to inter-operate with electric power systems on the time-scale of generator dispatch, the Optimal Gas Flow problem (OGF) must take into account transient flow conditions and new optimization models are required to capture the gas dynamics in pipeline networks [117]. In particular, an automatic control methodology for optimally managing transient intra-day flows in gas transmission systems necessitates stable, accurate, physics-based, and efficient optimization algorithms for computing model-based compressor control protocols.

5.2   Prior and Related Work

Early studies [26, 27] focused on optimizing steady-state gas flows, for which the state equations are algebraic relations. Recent efforts have scaled and improved optimization techniques for similar problems [84, 85, 82, 86, 87]. In short-term operations, the operating set-points for gas compressor stations can be readily changed, and compressor optimization for steady-state flows has been solved in the form of an Optimal Gas Flow problem (OGF) [82].

Recent studies [79, 11] focusing on transient flow dynamics use Euler equations for compressible gas flow in one-dimension. These equations are significantly simplified as the system under considerations do not experience waves or shocks in the corresponding appropriate spatial and temporal scales. These partial differential equations (PDEs), even after simplifications, are still highly nonlinear and are challenging to simulate [118], in particular for networks coupling hundreds of equations over different domains [119]. The vast majority of previous studies on gas pipeline transients were focused on physical modeling and simulation of initial value problems (IVPs) [120, 121, 122]. Thorley et al. [118] gave an excellent survey on the early literature. These traditional approaches to solve the PDEs usually yield fine space-time discretization schemes, which are not tractable when transformed to optimization problems.

The nonlinearity and complexity of gas pipeline network dynamics is an obstacle to the tractable optimization of these flows under transient conditions. Several studies [123, 124, 125, 6] have proposed optimization schemes for gas networks on the time-scale of daily operations and the issues of computation time and scalability have been noted repeatedly. These dynamic optimization methods aim to provide time-dependent schedules for compressor discharge pressures satisfying pipeline constraints and meeting time-varying loads. These computations are

typically intensive and often too slow for real-time decision-making. This motivates the need for new optimization tools.

Existing approaches for dynamic optimization in gas pipelines typically fall into one of two categories: a simulation-based approach or a discretize-then-optimize approach. Simulation-based methods in general optimize controllable parameters and rely on repeated executions of high-fidelity simulations to ensure that operational constraints (e.g., pressure limits in a natural gas system) are satisfied [123, 126]. By solving initial value problem (IVP) based on fine and detailed physical-engineering models to evaluate dynamic constraints, this method provides strong guarantees that all operational constraints are satisfied, hence the solution will be feasible. These methods are usually augmented with adjoint-based gradient [127] methods, exploiting sparsity of matrices and allowing parallelization to speed up the computational time. However, higher order derivatives and Jacobians of active constraints for accelerating convergence and improving robustness are in general computationally costly.

Alternatively, the discretize-then-optimize approach allows rapid evaluations on the Jacobians (constraint) for the entire optimization period [124]. This method starts with an optimal control formulation including a cost objective and constraints on state variables. Differential-algebraic approximations of the PDE dynamic constraints are then imposed within the optimization problem, instead of being enforced by independent simulations. The entire problem is discretized using approximations of the functions evaluated at time- / space- collocation points, by local difference schemes [125] or spectral approximation schemes [6]. This results in a nonlinear program (NLP), or a mixed-integer nonlinear program (MINLP) if binary/integer variables exist, with algebraic objective and constraint functions. One drawback of this method is that the resulting NLP/MINLP formulation can be huge and require efficient techniques to solve, e.g. by taking advantage of the special structure of the problem or by recently developed general optimization tools exploiting sparse constraint matrix [34].

Recent approaches in building a reduced order representation of PDE dynamics on graphs [128] and their extensions to control system modeling [6, 34], have enabled tractable representations of gas pipeline system dynamics. These models can be used to express constraints in dynamic optimization problems and allow the constraints over the entire optimization time interval to be represented by a coarse discretization scheme. Our work follows the discretize-then-optimize approach. Even though our proposed framework will be discretized on a coarser grid with lower accuracy when comparing to simulation-based approaches for computational tractability, our results show the induced error remains local and the solutions are acceptable.

5.3 Our Main Contribution

Our work examine the Dynamic Optimal Gas Flow problem (DOGF), which generalizes the OGF to capture the dynamics of a gas pipeline network subject to time-dependent intra-day consumptions. The objective of the DOGF is to minimize the cost of gas compression subject to system pressure constraints and time-dependent flow withdrawals. Our main contribution is *an efficient optimization scheme* for the DOGF, that is validated with an accurate simulation method for gas pipeline networks with dynamic flows and compressor operations. The DOGF is formulated for optimizing intra-day flow schedules. We further simplify our work by not considering valves as controllable variables, as major topological changes for re-routing flows

by changing valve positions are typically made on a weekly or monthly basis. Generalizing the problem to include valves will significantly increase the model complexity with potentially a large number of binary variables, and beyond the scope of our work. By fixing the system topology, we formulate the DOGF as a continuous-time and continuous-state optimal control problem, which can be discretized as a nonlinear program.

The key aspects of our optimization scheme can be summarized as follows. The hydrodynamic relations describing gas flows are discretized in time and space using first-order approximations [6]. Several approximations of the nonlinear constraints are proposed: The spatial discretization is performed by either the trapezoidal rule or a lumped element approximation, while the temporal discretization employs either a trapezoidal rule or a pseudospectral approximation. While trapezoidal, lumped element, and similar space-discretization schemes have been used in simulation studies [118, 128], pseudospectral schemes are often used for time discretization in computational optimal control [129]. For various combinations of discretization schemes in time and space, we investigate the trade-offs between computational efficiency of the optimization and feasibility of the physical model, and further verified by a fine-grained simulation. While a significant theory exists on the convergence of computational optimal control methods based on pseudospectral approximation [130, 131], such schemes will result in a dense matrix to solve due to its discretization nature. Simpler local discretization rules, on the other hand, result in a sparse matrix allowing state-of-the-art NLP solvers to exploit sparse matrix computations yielding a faster runtime and potentially more accurate solutions. We find that for the DOGF problem, the combination of lumped elements in space and trapezoidal rule in time yields the most advantageous discretization.

We acknowledge that, in general, time and space discretizations for PDEs cannot be chosen independently. In this study, we focus on practical algorithmic aspects of dynamic optimization of pipeline transients, rather than the theoretical justifications of particular discretization schemes for parabolic PDE systems. We support the resulting optimization approach by empirically comparing the solution of the dynamic constraints (pressures and flows) to solutions using a validated high-fidelity simulation of the same constraints. This approach is inspired by the simulation methodology for solving initial value problems [6, 128], where the uniform lumped element space discretization yields a differential algebraic equation (DAE) system on a fixed space grid. Starting from the initial conditions, the equations are integrated forward in time using adaptive stepping, thus falling into the class of method of lines (MOL) approaches [132]. We apply time-discretization to the dynamic constraints after they have been discretized in space, and examine the quality of solutions empirically based on several case studies.

Moreover, to compensate for potential inaccuracies and model operational constraints on compressors, our work proposes a two-stage optimization approach. In the first stage, the scheme optimizes the compression cost (the original objective). In order to obtain a solution that appropriately represents smooth fluid flow physics and operational considerations, the second stage minimizes the second-order time derivative of the compressor boost ratios while ensuring that the overall compression costs remain close to the value found in the first stage.

The resulting large-scale, nonlinear optimization problems (with up to 130,000 decision variables) are solved using the IPOPT 3.12.2, ASL routine (version 2015) nonlinear optimization system [103]. The solutions produced by our optimization scheme are compared to a validated dynamic simulation method for gas pipeline networks with transient compression

[133, 134], which is parametrized by the compressor ratios from our optimized solutions. The validation process indicates our optimization scheme produces solutions with no pressure constraint violations and with physically meaningful mass flow and pressure trajectories, matching close to the corresponding simulations. The compressor ratios from our four discretization variants exhibit negligible differences and converge to the same solution. The main benefit of our optimization scheme is its computational efficiency. It provides a highly accurate solution to a previously investigated 24-pipe gas network case study in less than 30 seconds, and demonstrates scalability to three pipeline networks with 25, 40, and 135 nodes, 24, 45, and 170 pipes, and with total pipeline lengths of 477, 1118, and 6964 kilometers respectively.

The rest of the chapter is organized as follows. Section 5.4 contains a summary of physical modeling of gas pipeline networks, and formulates the DOGF. Section 5.5 describes the discretization schemes that we examine. Section 5.6 motivates and presents our two-stage optimization approach to enforce smooth, physically accurate solutions. Section 5.7 describes computational and validation results for three case studies on systems of increasing scale and complexity. Section 5.8 presents an extended formulation to showcase how to model other related/similar problems.

5.4 The Dynamic Optimal Gas Flow Problem (DOGF)

We now introduce the equations to formalize the DOGF. Terminologies and notations for the natural gas transmission systems have been introduced in Chapter 2.2, and readers are advised to refer to Table 2.3 for referencing purposes.

The DOGF uses directly the two main dimensionless equations introduced in Chapter 2.2 to reason on the natural gas dynamics:

$$\frac{\partial \tilde{p}_{ij}}{\partial \tilde{t}_{ij}} + \frac{\partial \tilde{q}_{ij}}{\partial \tilde{x}_{ij}} = 0, \tag{5.1}$$

$$2\tilde{p}_{ij}\frac{\partial \tilde{p}_{ij}}{\partial \tilde{x}_{ij}} + \tilde{q}_{ij}|\tilde{q}_{ij}| = 0, \tag{5.2}$$

Since design limits and regulations for pipeline systems require pressure to remain within specified bounds, we have the following constraints on pressure to bound values within $[\underline{\tilde{p}}_{ij}, \overline{\tilde{p}}_{ij}]$:

$$\underline{\tilde{p}}_{ij} \le \tilde{p}_{ij}(\tilde{t}_{ij}, \tilde{x}_{ij}) \le \overline{\tilde{p}}_{ij}. \tag{5.3}$$

To model the action of compressors (introduced in Chapter 2.2), we have the following two equations:

$$\lim_{\tilde{x}_{ij} \searrow c_{ij}} \tilde{p}_{ij}(\tilde{t}_{ij}, \tilde{x}_{ij}) = R_{ij}(\tilde{t}_{ij}) \lim_{\tilde{x}_{ij} \nearrow c_{ij}} \tilde{p}_{ij}(\tilde{t}_{ij}, \tilde{x}_{ij}), \tag{5.4}$$

$$\lim_{\tilde{x}_{ij} \searrow c_{ij}} \tilde{q}_{ij}(\tilde{t}_{ij}, \tilde{x}_{ij}) = \lim_{\tilde{x}_{ij} \nearrow c_{ij}} \tilde{q}_{ij}(\tilde{t}_{ij}, \tilde{x}_{ij}). \tag{5.5}$$

with the cost of compression S_{ij} proportional to the required power, and is approximated by

$$S_{ij}(\tilde{t}_{ij}) = \eta^{-1}|\tilde{q}_{ij}(\tilde{t}_{ij},c_{ij})|(\max\{R_{ij}(\tilde{t}_{ij}),1\}^{2K}-1) \qquad (5.6)$$

In this study we do not consider pressure regulation (decompression), so the compressor ratio for a given station must remain bounded within a feasible operating region

$$\max\{\underline{R}_{ij},1\} \leq R_{ij} \leq \overline{R}_{ij}. \qquad (5.7)$$

A compression ratio with a value greater than 1, i.e., $R_{ij}(\tilde{t}_{ij}) \geq 1$, corresponds to a compressor applying power in its defined working direction. A value of $R_{ij}(\tilde{t}_{ij}) = 1$ denotes a compressor which is bypassed by the flow, in either the working or the reverse direction.

In addition to the dynamic equations (5.1)-(5.2) and continuity conditions for compressors (5.4)-(5.5) that characterize the system behavior on each pipe $P_{ij} \in \mathscr{P}$, we specify balance conditions for each junction $J_i \in \mathscr{J}$. We first define variables for the unique nodal pressure $p_i(t)$ at each junction, as well as mass injections $f_i(t)$ from outside the system (negative for withdrawals/consumption). Each junction $J_j \in \mathscr{J}$ then has a flow balance condition

$$\sum_{J_k \in \mathscr{J}:P_{jk}\in\mathscr{P}} \tilde{q}_{jk}(\tilde{t}_{ij},0) - \sum_{J_i \in \mathscr{J}:P_{ij}\in\mathscr{P}} \tilde{q}_{ij}(\tilde{t}_{ij},L_{ij}) = f_j(t), \qquad (5.8)$$

as well as a pressure continuity condition

$$\tilde{p}_{ij}(\tilde{t}_{ij},L) = p_j(t) = p_{jk}(\tilde{t}_{ij},0), \qquad (5.9)$$
$$\forall J_i,J_k \in \mathscr{J} \text{ s.t. } P_{ij},P_{jk} \in \mathscr{P}$$

where $\tilde{t}_{ij}$ is the pipe-dependent dimensionless time transformed from the time t in nominal unit. A subset of the junctions $\mathscr{S} \subset \mathscr{J}$ may be treated as "slack" nodes, which reasonably represent large sources in a transmission system, such as significant storages or interconnections. For these junctions, the mass inflow $f_i(t)$ is a free variable and the nodal pressure is defined at a supply pressure boundary parameter $s_i(t)$ (in dimensionless pressure unit). For the remaining junctions, which reasonably represent consumers or small suppliers, the nodal pressure $p_i(\tilde{t}_{ij})$ is free and the mass inflow is initialized with an injection/withdrawal boundary parameter $d_i(t)$ (in dimensionless flux unit). These boundary conditions are given by

$$p_i(t) = s_i(t), \qquad f_i(t) = d_i(t). \qquad (5.10)$$

The injections and withdrawals of the pipeline network are expressed in terms of mass flow in our formulations. While the contracts and daily nominations of natural gas are given in units of energy, e.g., kWh or mmBtu, the assumption of uniform system-wide composition allows us to use the mass flow units. In practice, the mass flow nominated depends on the calorific value, which is normally assumed to be known at the sources. Our focus is on large-scale transmission pipelines receiving gas from processing plants, which supply gas with composition of less than 2% variability. Preliminary validation using real data of transmission pipeline modeling with density and mass flow models has recently shown to be an acceptable approach in an industrial setting [135].

The optimization problem that we solve involves a gas pipeline network for which the conditions at each junction are parameterized by an injection/withdrawal $d_i(t)$ or supply pressure $s_i(t)$. The design goal is for the system to deliver all of the required flows $d_i(t)$ while maintaining feasible system pressure given the physics-based dynamic constraints, and minimizing the cost of compression over a time interval $[0,T]$. Let $\tilde{T}_{ij} = T\frac{\lambda a^4 q_N^3}{D_{ij}A_{ij}^3 p_N^3}$ to be the dimensionless time horizon of P_{ij}. This cost objective is given by

$$C = \sum_{P_{ij} \in \mathscr{C}} \int_0^{\tilde{T}_{ij}} S_{ij}(\tilde{t}_{ij}) d\tilde{t}_{ij} \tag{5.11}$$

In this study, we consider time-periodic boundary conditions on the system state and controls, i.e.,

$$\tilde{p}_{ij}(0,\tilde{x}_{ij}) = \tilde{p}_{ij}(\tilde{T}_{ij},\tilde{x}_{ij}), \tilde{q}_{ij}(0,\tilde{x}_{ij}) = \tilde{q}_{ij}(\tilde{T}_{ij},\tilde{x}_{ij}), \forall P_{ij} \in \mathscr{P} \tag{5.12}$$

$$R_{ij}(0) = R_{ij}(\tilde{T}_{ij}), \quad \forall P_{ij} \in \mathscr{C} \tag{5.13}$$

and therefore feasible parameter functions also must satisfy $d_i(0) = d_i(T)$ and $s_i(0) = s_i(T)$. The complete formulation is

$$
\begin{aligned}
\min \quad & C \text{ in } (5.11) \\
s.t. \quad & \text{pipe dynamics: } (5.1),(5.2) \\
& \text{compressor continuity: } (5.4),(5.5) \\
& \text{junction conditions: } (5.8),(5.9) \\
& \text{density \& compression constraints: } (5.3),(5.7) \\
& \text{periodicity constraints: } (5.12),(5.13) \\
& \text{boundary parameters: } (5.10) \\
& \text{compressor power: } (5.6)
\end{aligned}
\tag{5.14}
$$

This problem is a continuous problem. In the next section, we describe a spatial and temporal discretization scheme, and conditions that facilitate efficient solution of this PDE-constrained optimization problem using standard nonlinear programming tools.

5.5 Discretization to a Nonlinear Program

We now introduce several discretization schemes to tackle the continuous optimal control problem. With different discretization schemes, the sparsity of the constraints to enforce the nonlinear spatiotemporal dynamics will be different, and could affect the speed of NLP solvers exploiting sparse matrix algebra. In all of our schemes, we have the following common notions. For each pipe P_{ij}, we have: 1) a set of $M+1$ time points $\tilde{t}_m^{ij}$, and 2) a set of $N_{ij}+1$ space points $\tilde{x}_n^{ij}$. Normalization and rescaling is performed after choosing the collocation points throughout the network in order to maintain consistency of the time/space discretization. We use a uniform grid for trapezoidal scheme for simplicity. For pseudospectral methods, the collocation points are chosen according to the polynomial approximation scheme.

5.5.1   Trapezoidal Quadrature Rule Approximation

For trapezoidal discretization, we discretize $\tilde{t}_m^{ij}$ and $\tilde{x}_n^{ij}$ uniformly:

$$\tilde{t}_m^{ij} = m\Delta_{ij}^t, \quad m = 0, 1, \ldots, M, \tag{5.15}$$

$$\tilde{x}_n^{ij} = n\Delta_{ij}^x, \quad m = 0, 1, \ldots, N_{ij}, \tag{5.16}$$

$$\Delta_{ij}^t = \frac{\tilde{T}_{ij}}{M}, \quad \Delta_{ij}^x = \frac{\tilde{L}_{ij}}{N_{ij}}. \tag{5.17}$$

Δ_{ij}^t and Δ_{ij}^x are (dimensionless) time and space discretization steps, and $\tilde{T}_{ij}$ is the dimensionless time horizon for pipe P_{ij} obtained from T according to (2.3). We omit the subscripts $\{ij\}$ on N_{ij} when they are clear from the context. For each of the $(M+1) \times (N_{ij}+1)$ discrete points in the time-space grid $\{(\tilde{t}_m^{ij}, \tilde{x}_n^{ij}) : 0 \leq m \leq M, 0 \leq n \leq N_{ij}\}$ within the (dimensionless) domain $[0, \tilde{T}_{ij}] \times [0, \tilde{L}_{ij}]$ for the flow dynamics on a pipe P_{ij}, we define

$$\tilde{p}_{ij}^{mn} \triangleq \tilde{p}_{ij}(\tilde{t}_m^{ij}, \tilde{x}_n^{ij}), \quad \tilde{q}_{ij}^{mn} \triangleq \tilde{q}_{ij}(\tilde{t}_m^{ij}, \tilde{x}_n^{ij}) \tag{5.18}$$

to be the pressure and mass flow variables at time $\tilde{t}_m^{ij}$ and location $\tilde{x}_n^{ij}$. In this discretization, we define temporal and spatial derivative variables at time $\tilde{t}_m^{ij}$ and location $\tilde{x}_n^{ij}$ by

$$\tilde{p}t_{ij}^{mn} \triangleq \frac{\partial \tilde{p}_{ij}}{\partial \tilde{t}_{ij}}(\tilde{t}_m^{ij}, \tilde{x}_n^{ij}), \quad \tilde{p}x_{ij}^{mn} \triangleq \frac{\partial \tilde{p}_{ij}}{\partial \tilde{x}_{ij}}(\tilde{t}_m^{ij}, \tilde{x}_n^{ij}), \tag{5.19}$$

$$\tilde{q}x_{ij}^{mn} \triangleq \frac{\partial \tilde{q}_{ij}}{\partial \tilde{x}_{ij}}(\tilde{t}_m^{ij}, \tilde{x}_n^{ij}). \tag{5.20}$$

A constraint that relates the discretized variables (5.18) to their derivatives (5.19)-(5.20) is created by approximating the integral over a time or space step by the trapezoid rule. This yields

$$\forall P_{ij} \in \mathscr{P} - \mathscr{C}, 0 \leq m \leq M-1, 0 \leq n \leq N: \quad \tilde{p}_{ij}^{m+1,n} - \tilde{p}_{ij}^{mn} \approx \frac{\Delta_{ij}^t}{2}\left(\tilde{p}t_{ij}^{m+1,n} + \tilde{p}t_{ij}^{mn}\right) \tag{5.21}$$

$$\forall P_{ij} \in \mathscr{P} - \mathscr{C}, 0 \leq m \leq M, 0 \leq n \leq N-1:$$

$$\tilde{p}_{ij}^{m,n+1} - \tilde{p}_{ij}^{mn} \approx \frac{\Delta_{ij}^x}{2}\left(\tilde{p}x_{ij}^{m,n+1} + \tilde{p}x_{ij}^{mn}\right), \quad \tilde{q}_{ij}^{m,n+1} - \tilde{q}_{ij}^{mn} \approx \frac{\Delta_{ij}^x}{2}\left(\tilde{q}x_{ij}^{m,n+1} + \tilde{q}x_{ij}^{mn}\right)$$

$$\tag{5.22}$$

5.5.2   Non-dimensional Dynamic Equation with Compressors

The non-dimensional dynamic equations (5.1)-(5.2) are then discretized in the above variables by

$$\forall P_{ij} \in \mathscr{P} - \mathscr{C}, 0 \leq m \leq M, 0 \leq n \leq N: \quad \tilde{p}t_{ij}^{mn} + \tilde{q}x_{ij}^{mn} = 0, \quad 2\tilde{p}_{ij}^{mn}\tilde{p}x_{ij}^{mn} + \tilde{q}_{ij}^{mn}|\tilde{q}_{ij}^{mn}| = 0$$

$$\tag{5.23}$$

For each pipe with compressors $P_{ij} \in \mathscr{C}$, we define the discrete compression variables R_{ij}^m for $m = 0, 1, \ldots, M$, and assume that the compressor is located at $c_{ij} = x_k$ for some $0 \leq k \leq N$,

where the dependence of k on the pipe P_{ij} in question is clear from the context. The pipe is then divided into two pipes P_{iju} and P_{ijl}, with non-dimensional lengths L_{iju} and L_{ijl}, and for which we define the discretized variables

$$\tilde{p}_{iju}^{mn} \triangleq \tilde{p}_{ij}(\tilde{t}_m^{ij}, \tilde{x}_n^{ij}), \quad \tilde{q}_{iju}^{mn} \triangleq \tilde{q}_{ij}(\tilde{t}_m^{ij}, \tilde{x}_n^{ij}), \quad 0 \le n \le k \tag{5.24}$$

$$\tilde{p}_{ijl}^{mn} \triangleq \tilde{p}_{ij}(\tilde{t}_m^{ij}, \tilde{x}_n^{ij}), \quad \tilde{q}_{ijl}^{mn} \triangleq \tilde{q}_{ij}(\tilde{t}_m^{ij}, \tilde{x}_n^{ij}), \quad k \le n \le N \tag{5.25}$$

and corresponding spatial derivative variables $\tilde{pt}_{iju}^{mn}$, $\tilde{px}_{iju}^{mn}$, and $\tilde{qx}_{iju}^{mn}$ for $0 \le n \le k$ and $\tilde{pt}_{ijl}^{mn}$, $\tilde{px}_{ijl}^{mn}$, and $\tilde{qx}_{ijl}^{mn}$ for $k \le n \le N$. These state and derivative variables satisfy

$$\tilde{p}_{iju}^{m+1,n} - \tilde{p}_{iju}^{mn} \approx \frac{\Delta_{ij}^t}{2}(\tilde{pt}_{iju}^{m+1,n} + \tilde{pt}_{iju}^{mn}), \quad 0 \le n \le k, \tag{5.26}$$

$$\tilde{p}_{ijl}^{m+1,n} - \tilde{p}_{ijl}^{mn} \approx \frac{\Delta_{ij}^t}{2}(\tilde{pt}_{ijl}^{m+1,n} + \tilde{pt}_{ijl}^{mn}), \quad k \le n \le N \tag{5.27}$$

for $P_{ij} \in \mathscr{C}$ and $0 \le m \le M-1$, and

$$\tilde{p}_{iju}^{m,n+1} - \tilde{p}_{iju}^{mn} \approx \frac{\Delta_{ij}^x}{2}(\tilde{px}_{iju}^{m,n+1} + \tilde{px}_{iju}^{mn}), \quad 0 \le n < k, \tag{5.28}$$

$$\tilde{p}_{ijl}^{m,n+1} - \tilde{p}_{ijl}^{mn} \approx \frac{\Delta_{ij}^x}{2}(\tilde{px}_{ijl}^{m,n+1} + \tilde{px}_{ijl}^{mn}), \quad k \le n \le N, \tag{5.29}$$

$$\tilde{q}_{iju}^{m,n+1} - \tilde{q}_{iju}^{mn} \approx \frac{\Delta_{ij}^x}{2}(\tilde{qx}_{iju}^{m,n+1} + \tilde{qx}_{iju}^{mn}), \quad 0 \le n < k, \tag{5.30}$$

$$\tilde{q}_{ijl}^{m,n+1} - \tilde{q}_{ijl}^{mn} \approx \frac{\Delta_{ij}^x}{2}(\tilde{qx}_{ijl}^{m,n+1} + \tilde{qx}_{ijl}^{mn}), \quad k \le n \le N \tag{5.31}$$

for $P_{ij} \in \mathscr{C}$ and $0 \le m \le M$. In addition, we require continuity constraints at the compressor location to connect pipes P_{iju} and P_{ijl} for all $P_{ij} \in \mathscr{C}$ and $0 \le m \le M$, which take the form

$$R_{ij}^m = \frac{\tilde{p}_{ijl}^{mk}}{\tilde{p}_{iju}^{mk}}, \quad \tilde{q}_{ijl}^{mk} = \tilde{q}_{iju}^{mk}. \tag{5.32}$$

The equations (5.1)-(5.2) on either side of the compressor are discretized for $P_{ij} \in \mathscr{C}$ by

$$\tilde{pt}_{iju}^{mn} + \tilde{qx}_{iju}^{mn} = 0, \quad 0 \le n \le k, \tag{5.33}$$

$$2\tilde{p}_{iju}^{mn}\tilde{px}_{iju}^{mn} + \tilde{q}_{iju}^{mn}|\tilde{q}_{iju}^{mn}| = 0, \quad 0 \le n \le k, \tag{5.34}$$

$$\tilde{pt}_{ijl}^{mn} + \tilde{qx}_{ijl}^{mn} = 0, \quad k \le n \le N, \tag{5.35}$$

$$2\tilde{p}_{ijl}^{mn}\tilde{px}_{ijl}^{mn} + \tilde{q}_{ijl}^{mn}|\tilde{q}_{ijl}^{mn}| = 0, \quad k \le n \le N, \tag{5.36}$$

for all $P_{ij} \in \mathscr{C}$ and $0 \le m \le M$. The equations (5.21)-(5.23) and (5.26)-(5.36) discretize the dynamic equations (5.1)-(5.2) and continuity conditions for compressors (5.4)-(5.5).

5.5.3   Pseudospectral Approximation

Another approach to time discretization is a pseudospectral approximation, which is a global approximation scheme that is endowed with the desirable properties of spectral accuracy [130]. We use the Legendre-Gauss-Lobatto (LGL) pseudospectral collocation scheme for time discretization [136, 137, 138]. Suppose we want to discretize a function into $M + 1$ time points $(\tau_0, \ldots, \tau_M)$. The scheme employs a Legendre polynomial of order M ($L_M(\tau)$) as the interpolant, and the appropriate time collocation points for the discretization are given as the zeros of the derivative of L_M (i.e., the zeros of $\frac{\partial L_M(\tau)}{\partial \tau}$). These points lie within the interval $[-1, 1]$, and rescaling (via affine transformation) is required to rescale the time points $\tilde{t}_m^{ij} \in [0, \tilde{T}_{ij}]$ to dimensionless ones of the form $\tau_m \in [-1, 1]$. This yields

$$\tau_m = \frac{2\tilde{t}_m^{ij} - \tilde{T}_{ij}}{\tilde{T}_{ij}}, \tag{5.37}$$

and also induces a re-scaled function f^T on $\tau_m \in [-1, 1]$, of form

$$f^T(\tau_m) = f(\tilde{t}_m^{ij}) \text{ where } \tilde{t}_m^{ij} = \frac{\tilde{T}_{ij}(\tau_m + 1)}{2}. \tag{5.38}$$

The scheme is based on the Mth degree interpolating polynomial $f^M(\tau)$, constructed as follows:

$$f^M(\tau) = \sum_{m=0}^{M} f^T(\tau_m)\phi_m(\tau), \text{ where } \phi_m(\tau) = \frac{1}{M(M+1)L_M(\tau_m)} \frac{(\tau^2 - 1)\frac{\partial L_M(\tau)}{\partial \tau}}{\tau - \tau_m}. \tag{5.39}$$

Because ϕ_m is constructed such that $\phi_m(\tau_j)$ will be 1 if $m = j$ and 0 otherwise, f^M will be equal to f^T on all discretized re-scaled points $(\tau_0, \ldots, \tau_M)$. By restricting our attention to f^M and only at the discretized points, we have the following approximation for differentiation:

$$\frac{\partial f(\tilde{t}_m^{ij})}{\partial \tilde{t}_{ij}} = \frac{\partial f^T(\tau_m)}{\partial \tau} \frac{\partial \tau}{\partial \tilde{t}_{ij}} \approx \frac{2}{\tilde{T}_{ij}} \frac{\partial f^M(\tau_m)}{\partial \tau} = \sum_{j=0}^{M} D_{mj} f^T(\tau_j) = \sum_{j=0}^{M} D_{mj} f(\tilde{t}_j^{ij}), \quad \forall 0 \le m \le M \tag{5.40}$$

where D_{mj} is the time differentiation coefficient on the jth Legendre polynomial at time τ_j:

$$D_{mj} = \frac{2}{\tilde{T}_{ij}} \begin{cases} \frac{L_M(\tau_m)}{L_M(\tau_j)} \frac{1}{\tau_m - \tau_j}, & m \ne j \\ -\frac{M(M+1)}{4}, & m = j = 0 \\ \frac{M(M+1)}{4}, & m = j = M \\ 0, & \text{otherwise} \end{cases} \tag{5.41}$$

We also obtain an expression for integration in $\tilde{t}_{ij}$ from t_a to t_b given by

$$
\int_{t_a}^{t_b} f(\tilde{t}_{ij}) d\tilde{t}_{ij} = \int_{\tau_a}^{\tau_b} f^T(\tau) \frac{\partial \tilde{t}_{ij}}{\partial \tau} d\tau \approx \frac{\tilde{T}_{ij}}{2} \int_{\tau_a}^{\tau_b} f^M(\tau) d\tau
$$
$$
= \frac{\tilde{T}_{ij}(\tau_b - \tau_a)}{2} \sum_{j=0}^{M} [f^T(\tau_j) w_j] = (t_b - t_a) \sum_{j=0}^{M} [f(\tilde{t}_j^{ij}) w_j]
$$

(5.42)

where w_j is the weighting coefficient with respect to the Lagrange polynomial ϕ_j:

$$
w_j = \frac{1}{M(M+1)} \frac{1}{(L_M(\tau_j))^2}
$$

(5.43)

To change from trapezoidal time discretization to LGL pseudospectral discretization, we replace (5.21), (5.26), and (5.27) by

$$
\tilde{p}t_{ij}^{mn} \approx \sum_{g=0}^{M} D_{mg} \tilde{p}_{ij}^{gn}
$$

(5.44)

for all $P_{ij} \in \mathscr{P} - \mathscr{C}$, $0 \le m \le M$, and $0 \le n \le N$, and

$$
\tilde{p}t_{iju}^{mn} \approx \sum_{g=0}^{M} D_{mg} \tilde{p}_{iju}^{gn}, \quad 0 \le n \le k,
$$

(5.45)

$$
\tilde{p}t_{ijl}^{mn} \approx \sum_{g=0}^{M} D_{mg} \tilde{p}_{ijl}^{gn}, \quad k \le n \le N
$$

(5.46)

for $P_{ij} \in \mathscr{C}$ and $0 \le m \le M$, where $\tilde{T}_{ij}$ is the pipe-dependent dimensionless time horizon, and k is the compressor location of pipe P_{ij}.

5.5.4 Lumped Element Approximation

We have approximated equations (5.1)-(5.2) by spatial discretization for both the pressure and flux variables and a time discretization for the pressure variables. One way to further decrease the computational complexity is to simplify the space discretization by using a lumped element approximation, where spatial derivative variables are removed. Instead of approximating spatial derivatives by (5.22) and (5.28)-(5.31), a lumped-element approximation is applied to the non-dimensional dynamic equations (5.1)-(5.2) by integrating along each pipe segment in space, either explicitly or by the trapezoid quadrature rule. This approximation yields the

relations:

$$\int_{\tilde{x}_n^{ij}}^{\tilde{x}_{n+1}^{ij}} \frac{\partial \tilde{p}_{ij}}{\partial \tilde{t}_{ij}} d\tilde{x}_{ij} \approx \frac{\Delta_{ij}^x}{2}(\tilde{pt}_{ij}^{mn} + \tilde{pt}_{ij}^{m,n+1}), \tag{5.47}$$

$$\int_{\tilde{x}_n^{ij}}^{\tilde{x}_{n+1}^{ij}} \frac{\partial \tilde{q}_{ij}}{\partial \tilde{x}_{ij}} d\tilde{x}_{ij} = \tilde{q}_{ij}^{m,n+1} - \tilde{q}_{ij}^{mn}, \tag{5.48}$$

$$\int_{\tilde{x}_n^{ij}}^{\tilde{x}_{n+1}^{ij}} 2\tilde{p}_{ij} \frac{\partial \tilde{p}_{ij}}{\partial \tilde{x}_{ij}} d\tilde{x}_{ij} = \int_{\tilde{x}_n^{ij}}^{\tilde{x}_{n+1}^{ij}} \frac{\partial (\tilde{p}_{ij})^2}{\partial \tilde{x}_{ij}} d\tilde{x}_{ij} = (\tilde{p}_{ij}^{m,n+1})^2 - (\tilde{p}_{ij}^{mn})^2, \tag{5.49}$$

$$\int_{\tilde{x}_n^{ij}}^{\tilde{x}_{n+1}^{ij}} \tilde{q}_{ij}|\tilde{q}_{ij}| d\tilde{x}_{ij} \approx \frac{\Delta_{ij}^x}{2}(\tilde{q}_{ij}^{mn}|\tilde{q}_{ij}^{mn}| + \tilde{q}_{ij}^{m,n+1}|\tilde{q}_{ij}^{m,n+1}|) \tag{5.50}$$

Substituting back into (5.1)-(5.2) yields

$$\frac{\Delta_{ij}^x}{2}(\tilde{pt}_{ij}^{mn} + \tilde{pt}_{ij}^{m,n+1}) + \tilde{q}_{ij}^{m,n+1} - \tilde{q}_{ij}^{mn} = 0, \tag{5.51}$$

$$(\tilde{p}_{ij}^{m,n+1})^2 - (\tilde{p}_{ij}^{mn})^2 + \frac{\Delta_{ij}^x}{2}(\tilde{q}_{ij}^{mn}|\tilde{q}_{ij}^{mn}| + \tilde{q}_{ij}^{m,n+1}|\tilde{q}_{ij}^{m,n+1}|) = 0, \tag{5.52}$$

for all $P_{ij} \in \mathscr{P} - \mathscr{C}$, $0 \le m \le M$, and $0 \le n \le N - 1$. By similar reasoning on pipes with compressors, we obtain (5.53)-(5.56) replacing (5.28)-(5.31):

$$\frac{\Delta_{ij}^x}{2}(\tilde{pt}_{iju}^{mn} + \tilde{pt}_{iju}^{m,n+1}) + \tilde{q}_{iju}^{m,n+1} - \tilde{q}_{iju}^{mn} = 0, \qquad 0 \le n \le k-1, \tag{5.53}$$

$$(\tilde{p}_{iju}^{m,n+1})^2 - (\tilde{p}_{iju}^{mn})^2 + \frac{\Delta_{ij}^x}{2}(\tilde{q}_{iju}^{mn}|\tilde{q}_{iju}^{mn}| + \tilde{q}_{iju}^{m,n+1}|\tilde{q}_{iju}^{m,n+1}|) = 0, \qquad 0 \le n \le k-1, \tag{5.54}$$

$$\frac{\Delta_{ij}^x}{2}(\tilde{pt}_{ijl}^{mn} + \tilde{pt}_{ijl}^{m,n+1}) + \tilde{q}_{ijl}^{m,n+1} - \tilde{q}_{ijl}^{mn} = 0, \qquad k \le n \le N-1, \tag{5.55}$$

$$(\tilde{p}_{ijl}^{m,n+1})^2 - (\tilde{p}_{ijl}^{mn})^2 + \frac{\Delta_{ij}^x}{2}(\tilde{q}_{ijl}^{mn}|\tilde{q}_{ijl}^{mn}| + \tilde{q}_{ijl}^{m,n+1}|\tilde{q}_{ijl}^{m,n+1}|) = 0, \qquad k \le n \le N-1 \tag{5.56}$$

for all $P_{ij} \in \mathscr{C}$ and $0 \le m \le M$. Overall, lumped element approximation can be seen as a simplified trapezoidal rule discretization in space, where (5.22) and (5.28)-(5.31) are omitted and (5.23), (5.33)-(5.36) are replaced with (5.51)-(5.52) and (5.53)-(5.56).

5.5.5 Constraints and Objective

We now show how to express the problem constraints and objective. The pressure variables must lie within the operational/safety bounds, as given in (5.3). In discretized form, we have for all $0 \le m \le M$ that

$$\underline{\tilde{p}}_{ij} \le \tilde{p}_{ij}^{nm} \le \overline{\tilde{p}}_{ij}, \qquad\qquad P_{ij} \in P-C, \quad 0 \le n \le N, \tag{5.57}$$

$$\underline{\tilde{p}}_{ij} \le \tilde{p}_{iju}^{nm} \le \overline{\tilde{p}}_{ij}, \qquad\qquad P_{ij} \in C, \quad 0 \le n \le k, \tag{5.58}$$

$$\underline{\tilde{p}}_{ij} \le \tilde{p}_{ijl}^{nm} \le \overline{\tilde{p}}_{ij}, \qquad\qquad P_{ij} \in C, \quad k \le n \le N \tag{5.59}$$

In addition, the compression ratio must lie within operational requirements and satisfy

$$\max\{\underline{R}_{ij}, 1\} \leq R_{ij}^m \leq \overline{R}_{ij}. \tag{5.60}$$

for all $P_{ij} \in \mathscr{C}$ and $0 \leq m \leq M$. The cost of compression is then expressed by a constraint

$$S_{ij}^m = \eta^{-1} \tilde{qm}_{ij}^m ((R_{ij}^m)^{2K} - 1) \tag{5.61}$$

for all $P_{ij} \in \mathscr{C}$ and $0 \leq m \leq M$, where $\tilde{qm}_{ij}^m$ is an auxiliary variable with the constraints

$$\tilde{qm}_{ij}^m \geq \tilde{q}_{iju}^{mk}, \quad \tilde{qm}_{ij}^m \geq -\tilde{q}_{iju}^{mk}, \tag{5.62}$$

so that minimizing $\tilde{qm}_{ij}^m$ will minimize $|\tilde{q}_{iju}^{mk}|$ (when $R_{ij}^m > 1$). Compressor cost is also constrained to be positive, i.e.,

$$S_{ij}^m \geq 0. \tag{5.63}$$

The balance conditions at junctions are enforced as follows. For all $0 \leq m \leq M$ and $J_j \in \mathscr{J}$,

$$\sum_{J_k \in \mathscr{J}: P_{jk} \in \mathscr{P}} \tilde{q}_{jk}^{m0} - \sum_{J_i \in \mathscr{J}: P_{ij} \in \mathscr{P}} \tilde{q}_{ij}^{mN} + \sum_{J_k \in \mathscr{J}: P_{jk} \in \mathscr{P}} \tilde{q}_{jku}^{m0} - \sum_{J_i \in \mathscr{J}: P_{ij} \in \mathscr{P}} \tilde{q}_{ijl}^{mN} = f_j^m, \text{ and} \tag{5.64}$$

For all $J_i, J_k \in \mathscr{J}$ s.t. $P_{ij}, P_{jk} \in \mathscr{P}$,

$$\tilde{p}_{ij}^{mN} = \tilde{p}_j^m = \tilde{p}_{jk}^{m0}. \tag{5.65}$$

Parametrization of these balance conditions for $0 \leq m \leq M$ is given by

$$f_i^m = \tilde{d}_i(t_m), \qquad\qquad J_i \in \mathscr{J} - \mathscr{S}, \tag{5.66}$$
$$p_i^m = \tilde{s}_i(t_m), \qquad\qquad J_i \in \mathscr{S}, \tag{5.67}$$

where $\tilde{d}_i(t)$ and $\tilde{s}_i(t)$ are given flow injection/withdrawal or supply pressure functions (in dimensionless form). The time-periodic boundary conditions on the states and controls are given for $0 \leq m \leq M$ by

$$-\varepsilon \leq \tilde{p}_{ij}^{0n} - \tilde{p}_{ij}^{Mn} \leq \varepsilon, \qquad\qquad \forall P_{ij} \in \mathscr{P} - \mathscr{C}, 0 \leq n \leq N \tag{5.68}$$
$$-\varepsilon \leq \tilde{p}_{iju}^{0n} - \tilde{p}_{iju}^{Mn} \leq \varepsilon, \qquad\qquad \forall P_{ij} \in \mathscr{C}, 0 \leq n \leq k \tag{5.69}$$
$$-\varepsilon \leq \tilde{p}_{ijl}^{0n} - \tilde{p}_{ijl}^{Mn} \leq \varepsilon, \qquad\qquad \forall P_{ij} \in \mathscr{C}, k \leq n \leq N \tag{5.70}$$
$$-\varepsilon \leq R_{ij}^0 - R_{ij}^M \leq \varepsilon, \qquad\qquad \forall P_{ij} \in \mathscr{C}. \tag{5.71}$$

where ε is a sufficiently small tolerance. The integral in the objective of problem (5.14) is approximated by a Riemann sum (normalized by U_m) of the form

$$C_1 \approx \sum_{P_{ij} \in \mathscr{C}} \sum_{m=0}^{M} U_m S_{ij}^m. \tag{5.72}$$
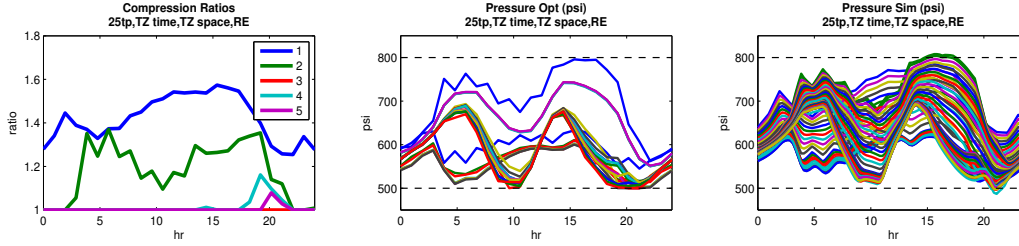
Figure 5.1: A non-smooth solution with trapezoidal time and space discretization. Left to right: Compression ratios; Pressure trajectories (optimization); Pressure trajectories (simulation)

where U_m denotes weights for the compression energy at time point m. We set U_m to $2/(M+1)$ for trapezoidal time discretization and to $2 \times w_m$ for pseudospectral time discretization to allow comparisons on the objective values for both discretization on the same scale (i.e. the dimensionless time interval re-scaled to $[-1, 1]$).

5.6   The Two-Stage Optimization Model

A direct encoding of the optimization problem over the discretized constraints and objectives may result in solutions where the pressure, flow, and compression ratio solutions may not be smooth. Figure 5.1 exhibits such a behavior on one of our test cases. The left and middle subfigures depict the compressor ratios and the pressures obtained by such a direct encoding. The right figure shows the results of a dynamic adaptive simulation using the optimal compressor ratios. The rapidly changing compression ratios in the optimal solution are undesirable from an operational standpoint: The application of such non-smooth controls would result in fast changes in pressure and flux (as seen in the right subfigure in Figure 5.1) which may cause severe damage to turbomachinery or piping. Moreover, the jitters in the pressure trajectories (in the middle subfigure) indicates that the physics is not represented accurately. Finally, the simulated pressures for these compressor ratios also violate their bounds and raises potential safety issues in practice.

The main problem with our model is that none of our constraints/objective consider smoothness to be an essential operational requirement. Therefore, the optimization solver would eventually consider non-smooth solutions that are infeasible to implement in practice. Indeed, If the compression ratio can be suddenly decreased and then increased later to compensate for the pressure losses on the discretized time intervals, the objective values can be further minimized. One suggestion is to further add constraints to limit the maximum deviation of control variables for each time step. However, our experimental results show that this method cannot fully tackle the problem, and the solver will still optimize for non-smooth solutions. These solutions minimize costs by maximizing the deviation of control variables, but stay within the maximum deviation limit.

To remedy these limitations, we add a second objective function that aims at producing

smooth compressor ratios. This second objective minimizes

$$C_2 = \sum_{P_{ij} \in \mathscr{C}} \sum_{m=0}^{M} \left[\frac{\partial^2 R_{ij}^m}{\partial \tilde{t}_{ij}^2} \right]^2 \tag{5.73}$$

i.e., the sum of the second derivatives of the compressor ratios over time. For the trapezoidal time discretization, the second derivatives can be approximated by

$$\frac{\partial^2 R_{ij}^m}{\partial \tilde{t}_{ij}^2} \approx \left(R_{ij}^{m+1} - R_{ij}^m \right) - \left(R_{ij}^m - R_{ij}^{m-1} \right) = R_{ij}^{m+1} + R_{ij}^{m-1} - 2R_{ij}^m$$

where we map R_{ij}^{-1} to R_{ij}^{M-1} and R_{ij}^{M+1} to R_{ij}^1 for the boundary cases. For the pseudospectral time discretization, we use

$$\frac{\partial^2 R_{ij}^m}{\partial \tilde{t}_{ij}^2} \approx \sum_{g=0}^{M} \frac{2}{\bar{T}_{ij}} D_{mg}^2 R_{ij}^g$$

where D^2 is equal to the matrix product of the differential matrix D with itself (i.e., $D^2 = D \cdot D$).

To integrate the two objectives, we employ a lexicographic strategy in our implementation, known as the two-stage method/decomposition [139]. We first solve the original nonlinear program with the first objective (5.72), and then solve the nonlinear program with the second objective (5.73), while imposing the additional constraint

$$C_1 \leq (1+r)f, \text{ where } 0 \leq r \leq 1 \tag{5.74}$$

where f is the objective value obtained from the first step. Intuitively, the tolerance r is a user-adjustable parameter that quantifies the factor of increase in compression energy that can be traded for a smoother solution. In our implementation, the second stage is initialized with the first-stage solution. This two-stage approach had the desirable property that smoothness can be controlled effectively, which was not the case when using a weighted sum of the two objectives with a penalty on C_2 or when imposing a smoothness-enforcing constraint directly in a one-stage optimization model. Two-stage methods are widely used in robust optimization [139]. Our approach is also similar to regularization method [140], which is often use in machine learning algorithms. We now summarize our formulation. The first-stage optimiza-
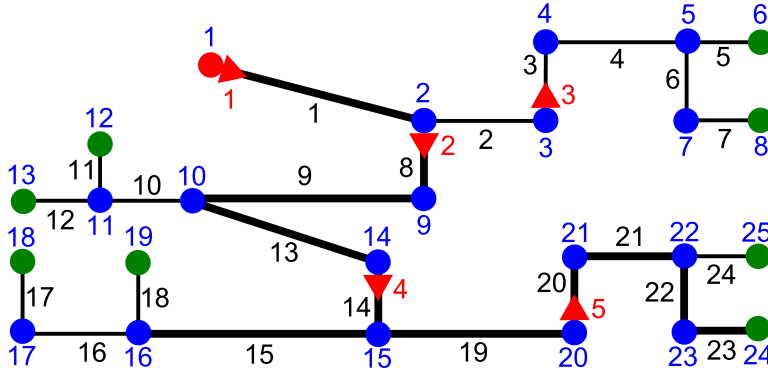
Figure 5.2: 24-pipe gas system test network used in the benchmark case study. Numbers indicate nodes (blue), edges (black), and compressors (red). Thick and thin lines indicate 36 and 25 inch pipes. Nodes are source (red), transit (blue), and consumers (green).

tion is specified by

$$
\begin{aligned}
\min \quad & C_1 : (5.72) \\
s.t. \quad & \text{time dynamics, either:} \begin{cases} \text{trapezoidal: } (5.21), (5.26) - (5.27), \text{ or} \\ \text{pseudospectral: } (5.44), (5.45) - (5.46) \end{cases} \\
& \text{space dynamics, either:} \begin{cases} \text{trapezoidal: } (5.22), (5.23), (5.28) - (5.31), (5.33) - (5.36), \text{ or} \\ \text{lumped element: } (5.51) - (5.56) \end{cases} \\
& \text{pressure \& compression safety constraints: } (5.57) - (5.60) \\
& \text{compressor power: } (5.61) - (5.63) \\
& \text{junction conditions: } (5.32), (5.64) - (5.65) \\
& \text{boundary parameters: } (5.66) - (5.67) \\
& \text{periodicity constraints: } (5.68) - (5.71)
\end{aligned}
$$

(5.75)

while the second-stage optimization is given by

$$
\begin{aligned}
\min \quad & C_2 : (5.73) \\
s.t. \quad & \text{1st stage problem constraints: } (5.75) \\
& \text{solution tolerance: } (5.74)
\end{aligned}
$$

(5.76)

5.7   Case Studies

The large-scale nonlinear programs for our DOGF are modeled with AMPL (version 2014) [100, 141] and solved with the nonlinear solver IPOPT 3.12.2, ASL routine (version 2015) [103] with AMPL pre-solve. The implementation is run on a Dell PowerEdge R415 with AMD Opteron 4226 and 64 GB of ram. We present the computational results on three case studies that include a validation of the approach, as well as results about solution quality, efficiency, and scalability.

Table 5.1: Aggregated Pressure Bound Violations (v_p, psi-days): 24 Pipe. (simulation: 10km space discretization)

	Trapezoidal time - trapezoidal space				Trapezoidal time - lumped element space			
Bounds	Tightened		Regular		Tightened		Regular	
Time pt.	5%	10%	5%	10%	5%	10%	5%	10%
25tp	0.000	0.000	0.913	0.899	0.000	0.000	0.939	0.876
50tp	0.000	0.000	0.076	0.058	0.000	0.000	0.116	0.090
100tp	0.000	0.000	0.000	0.007	0.000	0.000	0.000	0.000
200tp	0.000	0.000	0.004	0.000	0.000	0.000	0.000	0.000

	Pseudospectral time - trapezoidal space				Pseudospectral time - lumped element space			
Bounds	Tightened		Regular		Tightened		Regular	
Time pt.	5%	10%	5%	10%	5%	10%	5%	10%
25tp	0.000	0.000	0.451	0.205	0.000	0.000	0.186	0.059
50tp	0.000	Time Limit	0.026	0.026	0.000	0.000	0.000	0.021

5.7.1 Validation

The solution obtained using our implementation was validated on the 24-pipe benchmark gas network used in prior work [6], and illustrated in Figure 5.2. The pressures at supply sources were fixed at 500psi ($\approx 3.45 \times 10^6$ Pa), the dimensionless constants for the dimensionless equation transformation were set to $p_N = 250$psi ($\approx 1.72 \times 10^6$ Pa) and $q_N = 100$ kg/s, physical parameters $a = 377.968$ m/s, $\gamma = 2.5$, and $\lambda = 0.01$ were used, and a time horizon $T = 24$ hrs (86400s) was considered. Parameters $D_{ij}, A_{ij}, L_{ij}, \overline{R_{ij}}$, and $\underline{R_{ij}}$ were set according to the benchmark case study, as well as time-dependent profiles of gas injections/withdrawals $d_i(t)$. For the trapezoidal space approximation, each pipe P_{ij} is discretized uniformly according to its length L_{ij} into $\lceil L_{ij}/E \rceil + 1$ segments, where E is set to 10km by default. The test case is a tree network and hence the flow direction on each pipe is known. The compressors are placed on the first segment of the ith end of every pipe $P_{ij} \in \mathscr{C}$.

The admissible pressure range is 500 to 800 psi throughout the network. A feasible solution to the discretized problem that satisfies the pressure constraints may cause these constraints to be violated in a high-accuracy simulation of the dynamics for the continuous problem. To address this issue, one version of our implementation tightens the pressure bounds conservatively by 4% or less, i.e., in the range [520,780] psi for this particular benchmark. We refer to this as "tightened" problem, while optimizing over the nominal constraints of 500 to 800 psi is referred to as the "regular" problem.

The optimization results were validated by using the optimized compression ratio solution as a time-varying parameter in a validated dynamic simulation method [133, 134]. The trajectories computed using the simulation are used to validate the optimization solution in two ways. First, we quantify how much the constraints on pressure are exceeded by evaluating the L_2-norm of the violations. The violation measure aggregates violations over the 24-hour period by integrating the square of the pressure violations (psi) of the bounds at every junction. It is
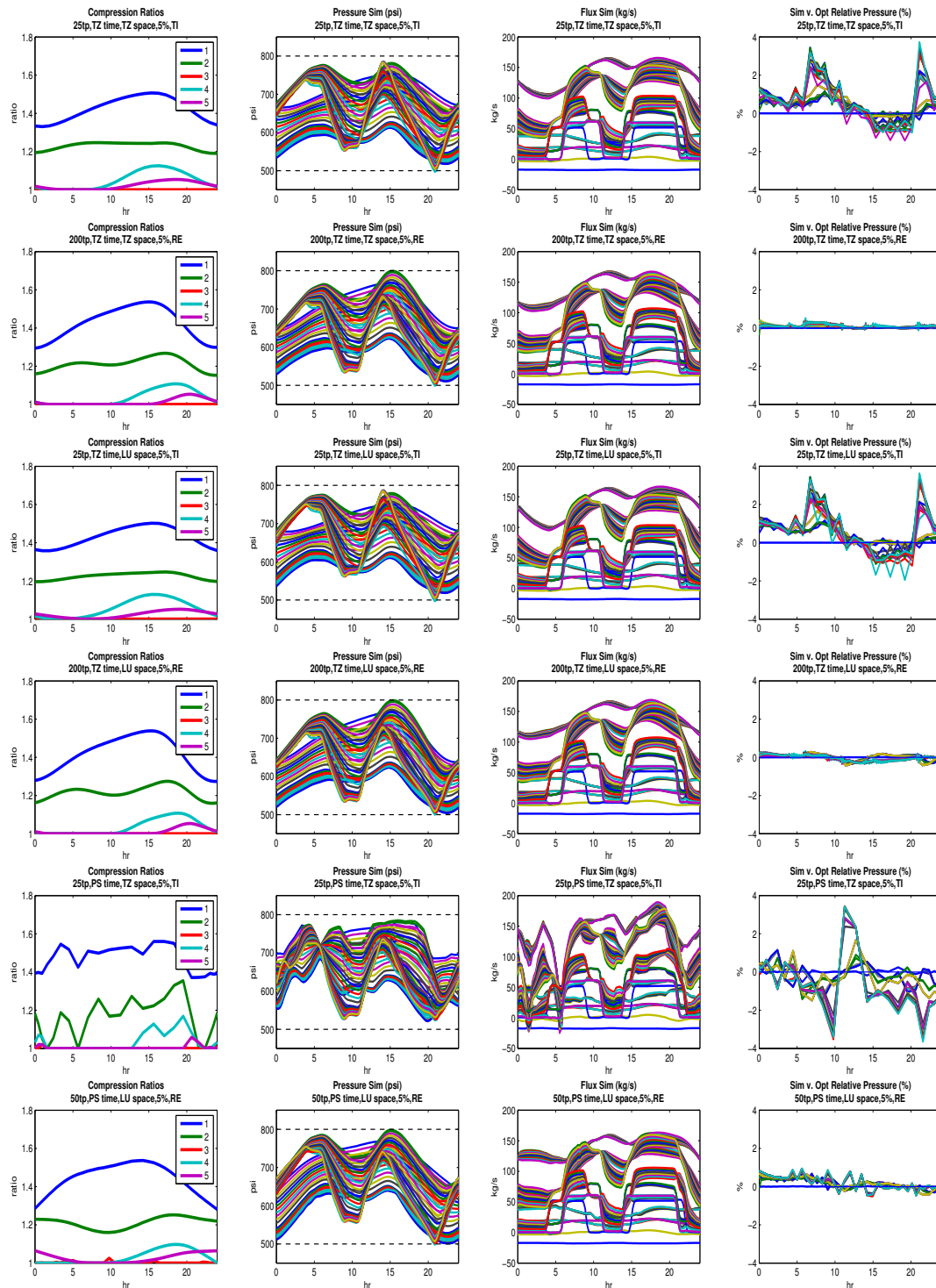
Figure 5.3: From top to bottom (24-System): Various discretization schemes: with different time points (tp), trapezoidal(TZ) / pseudospectral(PS) time scheme, trapezoidal(TZ) / lumped element(LU) space scheme, 5% re-optimization tolerance, and tightened(TI) / regular(RE) constraints. From left to right: Optimal compressor ratios; Pressure trajectories from simulation using the controls; Flux trajectories from the same simulation; Relative difference between pressure solution from optimization and pressure trajectories from simulation.

Table 5.2: Aggregated Pressure Bound Violations (v_p, psi-days): 24 Pipe. (simulation: 3km space discretization)

Bounds	Trapezoidal time - trapezoidal space				Trapezoidal time - lumped element space			
	Tightened		Regular		Tightened		Regular	
Time pt.	5%	10%	5%	10%	5%	10%	5%	10%
25tp	0.000	0.000	0.951	0.916	0.000	0.000	0.994	0.896
50tp	0.000	0.000	0.100	0.071	0.000	0.000	0.146	0.109
100tp	0.000	0.000	0.000	0.001	0.000	0.000	0.000	0.000
200tp	0.000	0.000	0.000	0.000	0.000	0.000	0.000	0.000

Bounds	Pseudospectral time - trapezoidal space				Pseudospectral time - lumped element space			
	Tightened		Regular		Tightened		Regular	
Time pt.	5%	10%	5%	10%	5%	10%	5%	10%
25tp	0.000	0.000	0.404	0.175	0.000	0.000	0.162	0.037
50tp	0.000	Time Limit	0.020	0.019	0.000	0.000	0.000	0.035

defined by

$$v_p = \sqrt{\sum_{P_{ij} \in \mathscr{P}} [\int_0^T (p_{ij}(t,0) - p_{\max})_+ \mathrm{d}t + \int_0^T (p_{\min} - p_{ij}(t,L_{ij}))_+ \mathrm{d}t]^2} \qquad (5.77)$$

where $(x)_+ = x$ if $x \geq 0$ and $(x)_+ \equiv 0$ if $x < 0$. The unit of the metric is psi-days. Tables 5.1 and 5.2 list solution values found using various time discretizations, smoothing parameter r, the tightened vs. regular problems, and using 3km and 10km space discretization settings. With tightened bounds, the optimization solution has no, or negligible, violations in the studied configurations.

Figure 5.3 depicts the optimal compressor ratio functions for 25 and 200 trapezoidal time discretization, 25 and 50 pseudospectral time discretization, with tightened and regular constraints, respectively, and with $E = 10$ km spatial trapezoidal discretization and lumped element approximation. The second-stage tolerance r is set to 5%. The results show that the compressor ratios over time are smooth, producing meaningful physical solutions and control profiles that can be implemented by operators. This is true even for coarse time discretizations. The only exception is the pseudo-spectral discretization (25tp, PS time, TZ space, 5%, tightened).

The last column of Figure 5.3 describes validation results that compare the optimization solutions with simulations. The simulation results were found by providing the optimal control solutions as input to a dynamic simulation of a differential algebraic equation (DAE) model of the network [6] and the adaptive time-stepping solver `ode15i` in MATLAB. Figure 5.3 reports the relative difference between the optimized pressure profiles p_j^m (re-scaled from dimensionless to nominal unit) for every junction in the network with the pressure trajectories $p_j^{m\star}$ obtained from simulations over time. Table 5.3 and Table 5.4 give the maximum relative error (in %) across all the pipe junctions and all the time steps for our four discretization

Table 5.3: Maximum relative difference (%) in pressure between simulation and optimization: 24 Pipe (simulation: 10km space discretization)

	Trapezoidal time - trapezoidal space				Trapezoidal time - lumped element space			
Bounds	Tightened		Regular		Tightened		Regular	
Time pt.	5%	10%	5%	10%	5%	10%	5%	10%
25tp	3.560	2.974	3.642	3.408	3.410	5.756	5.641	3.413
50tp	1.935	2.668	1.503	2.767	2.721	3.350	3.302	2.431
100tp	2.062	2.480	2.126	1.723	1.883	3.500	2.137	2.923
200tp	1.412	1.335	1.248	1.314	1.291	1.499	1.267	1.399

	Pseudospectral time - trapezoidal space				Pseudospectral time - lumped element space			
Bounds	Tightened		Regular		Tightened		Regular	
Time pt.	5%	10%	5%	10%	5%	10%	5%	10%
25tp	3.936	4.777	4.107	4.785	3.861	4.767	4.001	4.694
50tp	0.922	Time Limit	1.004	0.950	0.734	0.795	0.806	0.756

schemes with the formula:

$$\max_{0 \le m \le M} \left[\max_{J_j \in \mathscr{J}} \left(\left| \frac{p_j^m - p_j^{m\star}}{p_j^m} \right| \right) \right] \times 100\% \tag{5.78}$$

We tested the test cases with both regular and tightened constraints, with a 5% and 10% re-optimization tolerance, and with both 3km and 10km space discretization settings in simulations.

With only 25 time points, the (time and space) trapezoidal methods gave smooth control profiles with less than 4% of error when compared with simulations. This error disappears almost entirely with 200 time points. In general, the lumped element method with a trapezoidal discretization for time gives slightly less accurate results. Because the sources of the compared pressure profiles are qualitatively very different, i.e., optimization of algebraic equations that discretize PDEs over a fixed grid compared with adaptive time-stepping solution of an ODE system, these results are a powerful cross-validation of both models.

5.7.2 Solution Quality and Efficiency

Table 5.5 reports the objective value C_1, computation time, and the number of variables of the proposed method for: a) trapezoidal time, trapezoidal space discretization, b) trapezoidal time, lumped element space discretization, c) pseudospectral time, trapezoidal space discretization, and d) pseudospectral time, lumped element space discretization, with smoothness parameters r equals to 5% and 10%. We vary time points from 25pt up to 300pt/50tp for trapezoidal/pseudospectral time discretization respectively. The table gives the value of the C_1 objective after the first stage, and also in the second stage for $r = 5\%$ and 10%. CPU times in seconds reported by IPOPT for the first and second stages are also given. First, observe that enforcing the smoothness of the solution does not fundamentally decrease the quality of the C_1 objective, which is important from an operational standpoint. Second, as expected, refining the time discretization increases the objective value in the various trapezoidal schemes (since more constraints are added). Third, for the trapezoidal time discretization, the convergence rate is fast

Table 5.4: Maximum relative difference (%) in pressure between simulation and optimization: 24 Pipe (simulation: 3km space discretization)

	Trapezoidal time - trapezoidal space				Trapezoidal time - lumped element space			
Bounds	Tightened		Regular		Tightened		Regular	
Time pt.	5%	10%	5%	10%	5%	10%	5%	10%
25tp	3.584	3.014	3.732	3.443	3.420	5.744	5.625	3.451
50tp	1.937	2.591	1.537	2.697	2.658	3.285	3.330	2.340
100tp	2.047	2.391	2.037	1.618	1.833	3.377	2.167	2.906
200tp	1.357	1.225	1.222	1.268	1.251	1.391	1.274	1.365

	Pseudospectral time - trapezoidal space				Pseudospectral time - lumped element space			
Bounds	Tightened		Regular		Tightened		Regular	
Time pt.	5%	10%	5%	10%	5%	10%	5%	10%
25tp	3.928	4.765	4.049	4.716	3.807	4.772	3.990	4.584
50tp	0.957	Time Limit	0.996	0.951	0.743	0.738	0.776	0.761

and the solutions obtained with a coarse discretization are already of high quality, as illustrated in Figure 5.3. The lumped element approximation further reduces the model size by more than 50% and increases computational efficiency by factors from 4 to 25 depending on the accuracy of the discretization. As a result, the method exhibits excellent performance. Consider the time granularities with 25 and 50 points: For $r = 10\%$, the method requires less than 10 seconds, which indicates that it can be used during real-time operations. On the other hand, the pseudospectral time discretizations are orders of magnitude slower than trapezoidal scheme. Pseudospectral methods link every pressure/flux differential variable to pressure/flux variables at every time step [136, 138], producing a dense constraint matrix. Since the iteration counts of IPOPT for both types of discretization are similar in scale, the increased matrix density in the pseudospectral discretization is responsible for the observed loss in efficiency.

5.7.3 Scalability

To study the scalability of the proposed method, two additional instances are considered: Gaslib-40 and Gaslib-135 from the GasLib library [142]. The pressure ranges are set to 500 to 800 psi and 500 to 1000 psi for Gaslib-40 and Gaslib-135 respectively, and the source pressures are set to 600 psi. Tables 5.6 and 5.8 present the results on solution quality and efficiency. We omit results for pseudospectral time method since it does not converge or scales poorly on both benchmarks.

The trapezoidal time methods scale well on Gaslib-40 and they exhibit similar behavior as in the 24-pipe network. In particular, it can be solved in less than two minutes. The Gaslib-135 network is much more challenging and consists of more than 6000km of pipes. Hence, we only consider the lumped element method and relax the acceptable tolerances (termination condition) of IPOPT from 10^{-6} to 10^{-4} given the size of the test case. The cases that satisfy the acceptable tolerance but fail to reach the optimality region (IPOPT default: 10^{-8}) are marked with '$*$' in the objective column. The results show that the lumped element method finds high-quality solutions in reasonable time, solving a 25pt discretization in about an hour. The objective function does not necessarily increase monotonically due to the difficulty in reaching

Table 5.5: Objective Value (C_1) and runtimes on 24 Pipe Network.

		Trapezoidal time - trapezoidal space discretization					
	Var. no.	Objective Value			CPU Time (secs)		
		1st Stage	2nd Stage		1st Stage	2nd Stage	
			$r = 5\%$	10%		$r = 5\%$	10%
25tp	11441	2.012	2.112	2.213	12	22	8
40tp	18041	2.088	2.193	2.297	35	78	22
50tp	22441	2.073	2.176	2.280	32	75	28
60tp	26841	2.091	2.195	2.300	43	164	42
80tp	35641	2.106	2.211	2.316	45	208	55
100tp	44441	2.126	2.233	2.339	131	230	73
150tp	66441	2.105	2.210	2.316	266	800	280
200tp	88441	2.136	2.243	2.350	545	582	447
300tp	132441	2.136	2.243	2.349	32169	2028	639

		Trapezoidal time - lumped element space discretization					
	Var. no.	Objective Value			CPU Time (secs)		
		1st Stage	2nd Stage		1st Stage	2nd Stage	
			$r = 5\%$	10%		$r = 5\%$	10%
25tp	4785	2.003	2.103	2.203	3	5	3
40tp	7545	2.068	2.172	2.275	6	12	6
50tp	9385	2.069	2.172	2.276	9	21	10
60tp	11225	2.088	2.192	2.297	25	29	10
80tp	14905	2.096	2.201	2.306	22	49	23
100tp	18585	2.100	2.205	2.310	65	80	32
150tp	27785	2.105	2.210	2.315	163	335	86
200tp	36985	2.114	2.220	2.325	320	299	145
300tp	55385	2.115	2.221	2.327	1212	309	345

		Pseudospectral time - trapezoidal space discretization					
	Var. no.	Objective Value			CPU Time (secs)		
		1st Stage	2nd Stage		1st Stage	2nd Stage	
			$r = 5\%$	10%		$r = 5\%$	10%
25tp	11389	2.168	2.276	2.384	337	572	435
50tp	22339	2.114	2.219	2.325	17160	31882	46687

		Pseudospectral time - lumped element space discretization					
	Var. no.	Objective Value			CPU Time (secs)		
		1st Stage	2nd Stage		1st Stage	2nd Stage	
			$r = 5\%$	10%		$r = 5\%$	10%
25tp	4759	2.161	2.270	2.378	72	185	126
50tp	9334	2.147	2.255	2.362	14309	30535	29836

the feasibility region. Still these results are promising and demonstrate the method's ability to find high-quality solutions to large networks.

We also report results on the validation of the solutions for Gaslib-40. Figure 5.4 presents the pressure and flow profiles resulting from simulations. The figure shows the differences in percentage for each junction over time between optimization and simulation on pressure trajectories. Table 5.7 again shows the maximum relative error across all the pipe junctions. In this larger benchmark, the method produces smooth control profiles with less than 2% of error using 50 trapezoidal time points. Figure 5.5 further shows two compression solutions on the Gaslib-135 benchmark.
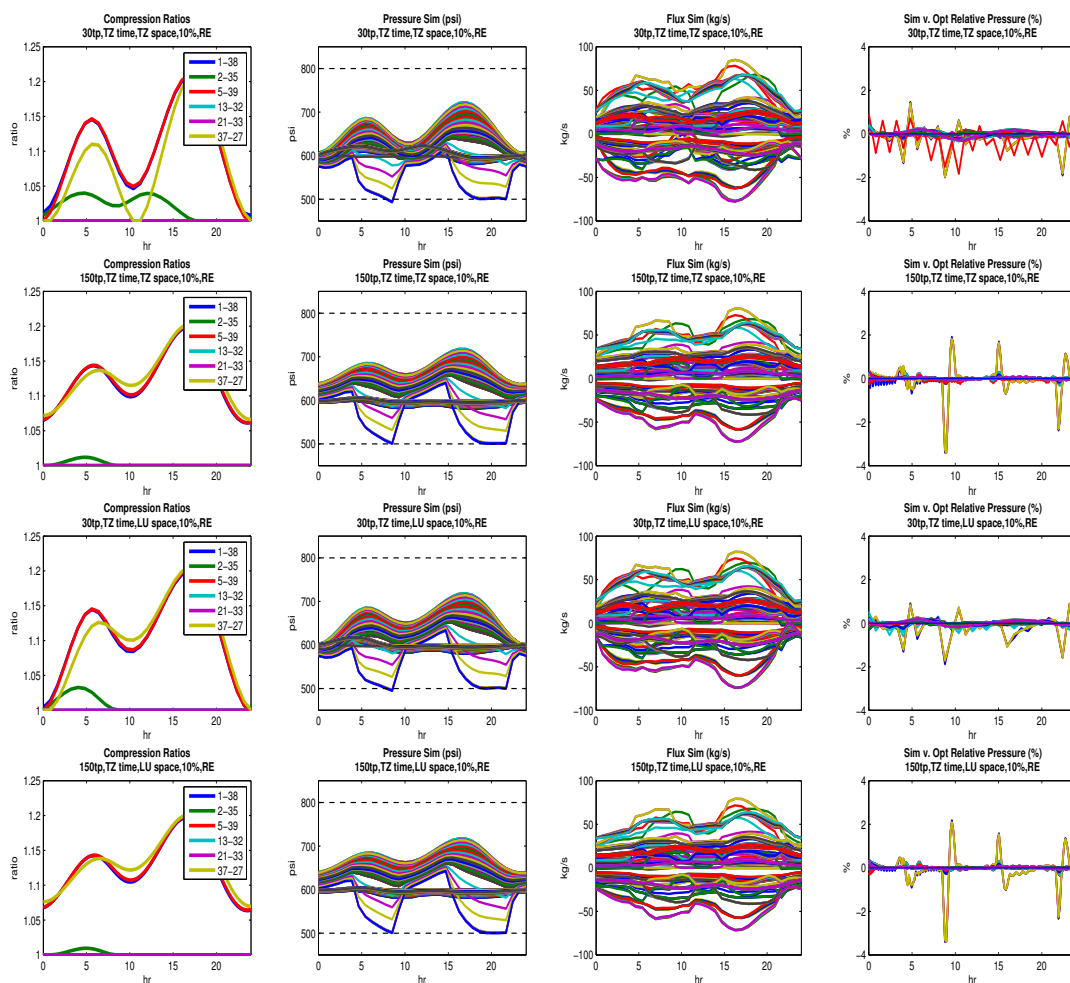
Figure 5.4: From top to bottom (Gaslib-40):: Various discretization schemes with: 30 and 150 time points (tp), trapezoidal(TZ) time scheme, trapezoidal(TZ) and lumped element(LU) space scheme, and 10% re-optimization tolerance. From left to right: Optimal control solution; Pressure trajectories from simulation using the controls; Flux trajectories from the same simulation; Relative difference between pressure solution from optimization and pressure trajectories from simulation.

The results in Figures 5.3–5.4 also show the benefits and justify our two-stage approach. The figures demonstrate that the largest errors occur when there are fast changes in the demands and are not due to compressor ratios.

5.8   Extensions & Variants

We now present a related optimization problem to showcase the generality of our proposed dynamic gas pipeline flow model. With the growing number of gas-fired generators, it becomes important in planning and signing contracts to understand how much gas could be supplied, packed into the system, and delivered to potential customers at any time. It is also important

Table 5.6: Objective Value (C_1) and runtimes on Gaslib-40 Pipe Network.

	Var. no.	Objective Value			CPU Time (secs)		
		1st Stage	2nd Stage		1st Stage	2nd Stage	
			$r = 5\%$	10%		$r = 5\%$	10%
20tp	20707	0.260	0.273	0.286	191	28	24
30tp	30567	0.294	0.309	0.323	541	54	268
40tp	40427	0.297	0.312	0.327	1143	164	444
50tp	50287	0.311	0.326	0.342	1316	213	1513
100tp	99587	0.321	0.337	0.353	9395	2666	1953
150tp	148887	0.323	0.339	0.355	15171	9363	8003

	Var. no.	Objective Value			CPU Time (secs)		
		1st Stage	2nd Stage		1st Stage	2nd Stage	
			$r = 5\%$	10%		$r = 5\%$	10%
20tp	6910	0.254	0.267	0.279	51	4	4
30tp	10200	0.297	0.312	0.326	45	40	39
40tp	13490	0.310	0.326	0.341	142	61	90
50tp	16780	0.311	0.326	0.342	148	84	153
100tp	33230	0.322	0.339	0.355	2566	648	575
150tp	49680	0.325	0.342	0.358	5139	3309	2605

(Top sub-table header: Trapezoidal time - trapezoidal space discretization. Bottom sub-table header: Trapezoidal time - lumped element space discretization.)

Table 5.7: Maximum relative difference (%) in pressure between simulation and optimization: Gaslib-40

	Trapezoidal time & trapezoidal space		Trapezoidal time & lumped element space	
Time pt.	5%	10%	5%	10%
20tp	6.198	Sim. Error	5.705	4.086
50tp	1.835	1.773	2.119	2.068
100tp	3.915	3.878	3.832	3.864
150tp	3.381	3.422	3.362	3.403

Table 5.8: Objective Value (C_1) and runtimes on Gaslib-135 Pipe Network.

	Var. no.	Objective Value			CPU Time (secs)		
		1st Stage	2nd Stage		1st Stage	2nd Stage	
			$r = 5\%$	10%		$r = 5\%$	10%
15tp	18769	2.027*	2.128	2.229	598	112	117
20tp	24634	2.492*	2.617	2.741*	713	314	445
25tp	30499	2.203*	2.313	2.423	1788	330	236

(Sub-table header: Trapezoidal time - lumped element space discretization.)

to understand the bottlenecks of transmission networks when planning for future upgrades.

In this section, we modify our optimization problem for the 24-pipe system to maximize the outflows for a set of important demand points $\mathscr{D} \subseteq \mathscr{J}$, while keeping the flow profiles for the other demands $\mathscr{J} \setminus \mathscr{D}$ fixed. In other words, equation (5.66) will be relaxed for demands in $\mathscr{D}$. To align our experiments with industry practice, we seek the maximal outflows that are steady (i.e., constant over time). Thus, we create decision variables f_j (negative for withdrawal) for
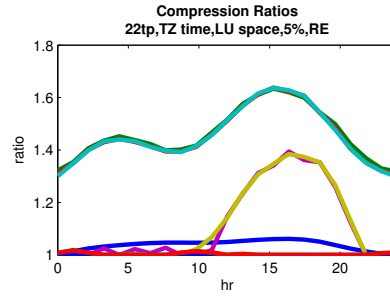
Figure 5.5: Compression ratio solutions for Gaslib-135 case studies, with 22 trapezoidal (TZ) time points, lumped element (LU) space, and re-optimization tolerance of $r = 5\%$.

functions $J_j \in \mathscr{D}$ and change (5.64) for these junctions to

$$\sum_{J_k \in \mathscr{J}:P_{jk} \in \mathscr{P}} \tilde{q}_{jk}^{m0} - \sum_{J_i \in \mathscr{J}:P_{ij} \in \mathscr{P}} \tilde{q}_{ij}^{mN} + \sum_{J_k \in \mathscr{J}:P_{jk} \in \mathscr{P}} \tilde{q}_{jku}^{m0} - \sum_{J_i \in \mathscr{J}:P_{ij} \in \mathscr{P}} \tilde{q}_{ijl}^{mN} = f_j, \quad f_j <= 0 \quad (5.79)$$

where f_j is now steady. We then replace (5.72) by

$$\max M_1 = -\sum_{J_j \in \mathscr{D}} c_j f_j \tag{5.80}$$

where c_j is the node-dependent costs. We further add penalty terms in (5.73) to smooth the source flux $\mathscr{S}$ which act as the slack variable in our formulation. This gives

$$C_2 = \sum_{P_{ij} \in \mathscr{C}} \sum_{m=0}^{M} \left[\frac{\partial^2 R_{ij}^m}{\partial \tilde{t}_{ij}^2} \right]^2 + w_p \sum_{J_j \in \mathscr{S}} \sum_{m=0}^{M} \left[\frac{\partial^2 f_j^m}{\partial t^2} \right]^2 \tag{5.81}$$

where w_p is the weight of the new penalty and f_j^m are the flux variables of the source. We use the same method as in (5.73) to approximate the second derivatives of f_j^m for both the trapezoidal and pseudospectral discretizations. Since we switch from minimization to maximization, we flip the inequality in (5.74) to obtain:

$$M_1 \geq (1 - r)v, \quad \text{where } 0 \leq r \leq 1, \tag{5.82}$$

and where v is the objective value obtained in the first step.

We report experimental results on on the 24 pipe system with three different cases:

1. Maximizing the outflow integral of 5 nodes with equal costs: $c_j = 1$ and $\mathscr{D} = \{6, 8, 12, 13, 19\}$,

2. Maximizing outflow of only node 19: $c_j = 1$ and $\mathscr{D} = \{19\}$, and

3. Case 1 with different weights/preferences c_j as shown in Table 5.9 (first two columns).

5.8.1 Case 1.

Table 5.10 shows the model size, objective values M_1, and computational runtimes for our 4 different discretization schemes on case 1 with varying number of time points and with

Table 5.9: Gas price ($ per 10 kg mass) and optimized demand (kg/s).

Node number	Gas price	Demand (case 1)	Demand (case 3)
Trapezoidal time, lumped space, 50 time point, $r = 7\%$			
6	1.0	21.582	0.000
8	1.5	16.498	36.067
12	2.0	87.537	38.836
13	2.0	0.057	0.025
19	3.0	0.000	46.364

Table 5.10: Objective Value (M_1) and runtimes on the maximum contractable throughput model: case 1

	Var. no.	Objective Value			CPU Time (secs)		
		1st Stage	2nd Stage		1st Stage	2nd Stage	
			$r = 3\%$	7%		$r = 3\%$	7%
		Trapezoidal time - trapezoidal space discretization					
25tp	11576	1.366	1.325	1.271	5	7	4
50tp	22701	1.356	1.315	1.261	25	17	36
100tp	44951	1.349	1.309	1.255	118	202	86
200tp	89451	1.348	1.308	1.254	1735	196	323
		Trapezoidal time - lumped element space discretization					
25tp	4920	1.362	1.322	1.267	3	1	1
50tp	9645	1.351	1.311	1.257	12	5	7
100tp	19095	1.345	1.304	1.251	88	21	26
200tp	37995	1.345	1.304	1.251	1017	143	248
		Pseudospectral time - trapezoidal space discretization					
25tp	11524	1.341	1.301	1.247	297	162	215
50tp	22599	1.352	1.312	1.258	33446	20305	17780
		Pseudospectral time - lumped element space discretization					
25tp	4894	1.350	1.309	1.255	112	141	186
50tp	9594	1.348	1.308	1.254	8262	13710	11775

two re-optimization tolerances: $r = 3\%$ and 7%. The smoothness weighting w_p is set to 50. Figures 5.6 and 5.7 present the optimized maximum demands, compression ratios, the pressure and the flux at each junction point, and the relative errors (in %) between simulation and optimization on 50 trapezoidal time points with lumped element discretization in space, and with $r = 3\%$ and $r = 7\%$. We obtain similar results to those of Sections 5.7.2–5.7.3. At the coarser discretization, the error between optimization and simulation is approximately 2%. The

convergence rate is fast for the trapezoidal time discretization and the solutions obtained with a coarse discretization are already of high quality. The lumped element approximation once again decreases the size of the model and improves the computational efficiency significantly. The pseudospectral time discretization is still orders of magnitude slower than the trapezoidal schemes.

Observe that the solution tends to allocate more flux for node 12 (refer to Figure 5.6/Table 5.9), located in the top-left portion of the 24-pipe network (see Figure 5.2), when compared to the other regions (e.g. the top-right and bottom-left regions). The path between the source at node 1 to node 11 consists of: a) a total of 165 km of three 36" diameter pipes, and b) one 5 km long 25" diameter pipe. If we roughly estimate resistance based on distance divided by diameter (in the unit of km/m), this will give a resistance metric of 188 (km/m). The path between the source at node 1 to node 5 consists of: a) one 100 km long 36" diameter pipe, and b) a total of 50km of three 25" diameter pipes. This will also give a resistance metric of 188 (km/m). However, the pipe length of pipe 11 (or 12) is slightly shorter than pipe 5 (or the combined length of pipe 6 and 7). This results in a lower resistance for allocating flux to the top-left region than the top-right region. Since we aim at minimizing compression energy for all of the compressors, the optimization model naturally chooses to optimize the path of least resistance (for compressor 2). Allocating flux to the path with more resistance would incur more compression energy (on compressor 3).
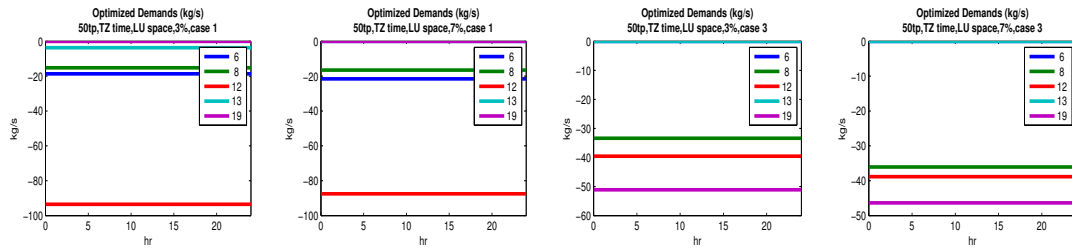

Figure 5.6: Optimized demands(kg/s). From left to right: case 1: $r = 3\%$ and 7%, and case 3: $r = 3\%$ and 7%.

5.8.2   Cases 2 and 3.

Case 2 is essentially a simplification of case 1, with the goal of finding the maximum contractable throughput for a specific demand point in the presence of the remaining known load profiles. Case 3 further considers price weights among different demands, with the goal to find the optimal contractable throughput based on maximum revenue to the pipeline operator. The optimal solution will then represent the maximum contractable revenue that the gas transmission system can obtain by optimizing allocation of supplies to flexible customers with different offer bids. We repeat the computational studies as done in previous sections on both cases with the trapezoidal time discretization and the lumped element space approximation. Table 5.11 shows the model size, objective values M_1, and computational runtimes. Figure 5.6 and Table 5.9 present one of the solutions for case 3 and compare it with case 1. Figures 5.7 and 5.8 also show the compression ratio, the pressure, and the flux at each junction point, and the
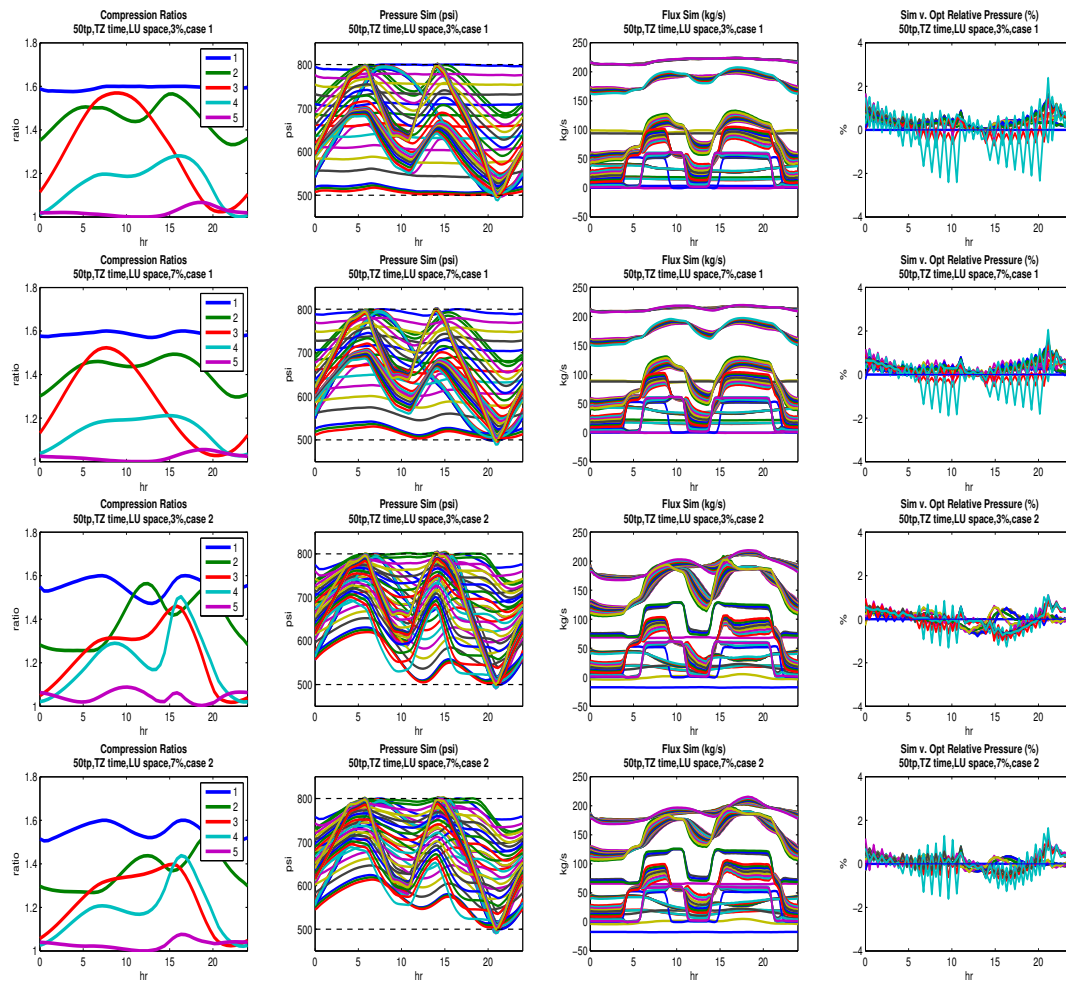
Figure 5.7: From top to bottom: Case 1 with 3% and 7% re-optimization tolerance, and case 2 with 3% and 7% re-optimization tolerance. Both with 50 trapezoidal time point, and lumped space approximation.

relative error (in %) between simulation and optimization for 50 time points. Once again, the results are consistent with the earlier case studies. The errors could be further reduced by increasing the discretization to 200 time points (Figure 5.8). Overall, these results show that the proposed method produces consistent results across a number of case studies and objectives.

Table 5.11: Objective Value (M_1) and runtimes: case 2 and 3

|		Case 2					
	Var. no.	Objective Value			CPU Time (secs)		
		1st Stage	2nd Stage		1st Stage	2nd Stage	
			$r = 3\%$	7%		$r = 3\%$	7%
25tp	4812	0.727	0.705	0.676	3	1	1
50tp	9437	0.704	0.683	0.654	7	4	5
100tp	18687	0.695	0.674	0.647	51	22	13
200tp	37187	0.696	0.675	0.647	500	178	330
		Case 3					
	Var. no.	Objective Value			CPU Time (secs)		
		1st Stage	2nd Stage		1st Stage	2nd Stage	
			$r = 3\%$	7%		$r = 3\%$	7%
25tp	4920	2.955	2.867	2.748	3	2	1
50tp	9645	2.913	2.826	2.709	12	4	5
100tp	19095	2.892	2.805	2.689	59	24	24
200tp	37995	2.893	2.807	2.691	359	89	180
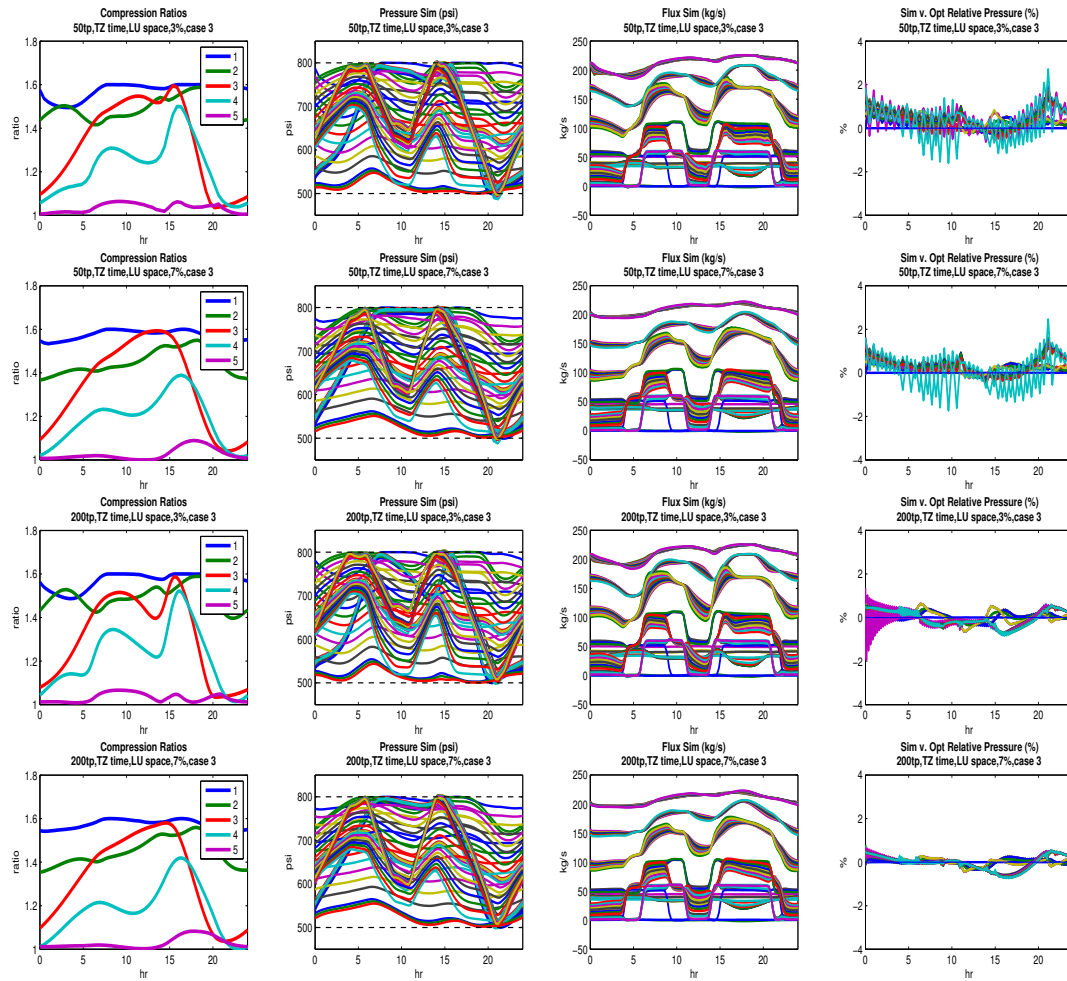
Figure 5.8: From top to bottom: Case 3 with 3% and 7% re-optimization, 50 trapezoidal time point, and lumped space approximation; Case 3 with 3% and 7% re-optimization, 200 trapezoidal time point, and lumped space approximation.

Conclusion and Future Work

In this thesis, we have introduced optimization techniques improving stability and control in three energy system applications.

6.1 Power System Restoration

Our first application focuses on the Restoration Ordering Problem (ROP) with transient stability and determines whether it is possible to transition between steady states produced by the ROP. We propose a new generalization of the ROP, the AC-ROP-SPASVD problem, that splits restoration steps into dispatching and closing steps. The formulation uses standing phase angle (SPA) constraints and voltage difference (VD) constraints as a surrogate for rotor swing reductions, which are being classified as indirect approaches in maintaining rotor angle stability. We show that using the DC power flow approximation can lead to infeasible solutions and adding SPA constraints on the DC power flow model does not reduce rotor swings. By utilizing the LPAC model, case studies indicate that the novel formulation reduces rotor swings of synchronous generators by over 50%, while having a negligible impact on the blackout size (i.e., $\leq 1.5\%$ increase), which is still optimized holistically. We further illustrate on the 39-Bus benchmark that reducing standing phase angles is not a sufficient condition for reducing rotor swings. To address this limitation, we further introduce VD constraints, which are effective in further reducing rotor swings.

Our contribution represent a first step in incorporating transient stability with power system restoration planning using indirect methods. Exploring a tighter integration of transient dynamics and optimization algorithms is an interesting direction for future work. Considering other important dynamics and known problems [16, 15], e.g. voltage and frequency dynamics, sustained over-voltage problems, and switching surges are also important future directions.

6.2 Transmission Line Switching

Our second application focuses on the Optimal Transmission Line Switching (OTS) problem with transient stability. We propose an automatic control and optimization routine to address transient stability during transmission line switching in congested situations. The optimization model uses a trapezoidal discretization of the differential algebraic equations for the 4th order two-axis generator model with an automatic voltage regulator (AVR), featuring two types

of control variables: generation dispatch and stabilizer parameters. We adopt an objective function minimizing the sum of the time-weighted rotor angle accelerations, to ensure increasingly smaller swings as time increases. Experimental results show that: 1) congestion leads to difficulties in ensuring rotor stability, 2) due to the lack of excitation controls, classical swing models cannot maintain rotor stability under congested conditions, 3) variables controlling setpoints of exciters and stabilizers are critical to ensure rotor stability, in particular to maintain (small-signal) oscillation stability, 4) with longer optimization horizons our algorithm is able to find more stable control solutions at the expense of computation runtime, 5) the optimization results validated against POWERWORLD simulations exhibit an average error in the order of 10^{-3} degrees for rotor angles, and 6) the optimization model is solved within minutes of computation time for the 0.16 sec discretization on the IEEE-39 bus test system, and scale well to the larger South East Australian Power System.

Our contribution can be viewed as an attempt to incorporate generator dynamic models into optimization. Future research directions include other higher order generator models and voltage/frequency dependent load models. Our work currently assumes that generator controls are the primary resources used for maintaining stability. With more flexible resources, e.g. battery resources, FACTs devices, and other digital controllers in smart grids, expected to be installed in the near future, incorporating these dynamics also represents venues for future work. The primary focus of our work is on transient stability and short-term oscillation stability. Extending this work to mid-term stability with frequency control is another opportunity for future work.

6.3   Dynamic Compressor Optimization

Our third contribution investigates the Dynamic Optimal Gas Flow (DOGF) problem in pipeline flow management. The problem is on minimizing operating costs of gas compressors while maintaining pressure constraints under dynamic intra-day conditions. The offtakes/demands by customers are described using time-dependent mass flow functions. This study was motivated by the growing reliance of electric power systems on gas-fired generators, which was driven by the need to balance intermittent sources of renewable energy and low gas prices. We present an efficient scheme for the DOGF that relies on a compact yet appropriately accurate representation of gas flow physics. We study and present two time discretization methods and two space discretization methods for our nonlinear optimization model. A two-stage approach is applied to minimize energy costs and maximize smoothness of compressor ratios. The resulting large-scale nonlinear programs are solved using an efficient general interior-point method, and the results are validated against an accurate simulation of the dynamic equations. The novel optimization scheme yields solutions that are feasible for the continuous problem and practical from an operational standpoint. Scalability of the scheme was demonstrated using three networks with 25, 40, and 135 nodes, 24, 45, and 170 pipes, and total pipeline lengths of 477, 1118, and 6964 kilometers respectively. We further extended the formulation to tackle the maximum throughput problem, demonstrating the flexibility of our model.

Our work extends the OGF problem with transient slow dynamics. One immediate extension to our work consists in applying this framework to other energy systems with similar dynamics/equations, e.g. water pipeline systems with fluid dynamic equations. Extending this

framework to other applications with gas dynamics would also be interesting, e.g. optimal control policies with other natural gas devices, expansion planning problems [143, 87], and reliability/security analysis [144, 115].

References

1. T. Athay, R. Podmore, and S. Virmani, "A practical method for the direct analysis of transient stability," *IEEE Transactions on Power Apparatus and Systems*, vol. PAS-98, no. 2, pp. 573–584, 1979. (cited on pages xv, 2, 9, 10, 50, and 64)

2. M. Pai, *Energy function analysis for power system stability*. Springer US, 1989. (cited on pages xv, 9, 10, 50, and 64)

3. Benchmark Systems for Stability Controls Task Force, "Benchmark systems for small-signal stability analysis and control (PES-TR18)," IEEE PES Power System Dynamic Performance Committee, Power System Stability Controls Subcommittee, Tech. Rep., Aug 2015. (cited on pages xv and 9)

4. I. Hiskens, "IEEE PES task force on benchmark systems for stability controls: 39 bus system MATLAB report," IEEE PES Power System Dynamic Performance Committee, Tech. Rep., Nov 2013, accessed 13 July 2016: http://eioc.pnnl.gov/benchmark/ieeess/IEEE39/New_England_Reduced_Model_(39_bus_system)_MATLAB_study_report.pdf. (cited on pages xv, 9, 10, and 64)

5. P. Kundur, *Power system stability and control*. McGraw-Hill Education, 1994. (cited on pages xv, 2, 7, 8, 10, 11, 12, 13, 14, 16, 22, 23, 24, 25, 26, 37, 39, 52, and 53)

6. A. Zlotnik, M. Chertkov, and S. Backhaus, "Optimal control of transient flow in natural gas networks," in *54th IEEE Conference on Decision and Control*, Osaka, Japan, 2015, pp. 4563–4570. (cited on pages xv, 27, 28, 29, 30, 80, 81, 82, 95, and 97)

7. "Powerworld simulator," PowerWorld Corporation, http://www.powerworld.com. (cited on pages xv, 36, 55, 66, and 70)

8. H. Mahgerefteh and O. Atti, "An analysis of the gas pipeline explosion at Ghislenghien, Belgium," in *2006 Spring Meeting & 2nd Global Congress on Process Safety*, April 2006. (cited on page 1)

9. B. Liscouski and W. Elliot, "Final report on the August 14, 2003 blackout in the United States and Canada: Causes and recommendations," *A report to US Department of Energy*, vol. 40, p. 4, 2004. (cited on page 1)

10. "Requirements for frequency and voltage ride through capability of small generating facilities: Order no. 828," Federal Energy Regulatory Commission. The United States of America, 2016, accessed 11 Jan 2017: https://www.ferc.gov/whats-new/comm-meet/2016/072116/E-11.pdf. (cited on page 1)

11. M. Herty, J. Mohring, and V. Sachers, "A new model for gas flow in pipe networks," *Mathematical Methods in the Applied Sciences*, vol. 33, no. 7, pp. 845–855, 2010. (cited on pages 2, 29, 30, 31, and 80)

12. B. Simon, C. Coffrin, and P. Van Hentenryck, "Randomized adaptive vehicle decomposition for large-scale power restoration," in *CPAIOR'12*, 2012, pp. 379–394. (cited on page 2)

13. C. Coffrin, P. V. Hentenryck, and R. Bent, "Last-mile restoration for multiple interdependent infrastructures," in *AAAI*, 2012. (cited on pages 2 and 18)

14. T. Nagata, H. Sasaki, and R. Yokoyama, "Power system restoration by joint usage of expert system and mathematical programming approach," *Power Systems, IEEE Transactions on*, vol. 10, no. 3, pp. 1473–1479, 1995. (cited on pages 2 and 18)

15. M. Adibi and L. Fink, "Power system restoration planning," *IEEE Transactions on Power Systems*, vol. 9, no. 1, pp. 22–28, 1994. (cited on pages 2, 16, 17, 36, 40, and 109)

16. M. Adibi and R. Kafka, "Power system restoration issues," *IEEE Computer Applications in Power*, vol. 4, no. 2, pp. 19–24, 1991. (cited on pages 2, 16, 17, 36, 40, and 109)

17. M. Adibi, J. Borkoski, and R. Kafka, "Power system restoration-the second task force report," *Power Systems, IEEE Transactions on*, vol. 2, no. 4, pp. 927–932, 1987. (cited on pages 2 and 17)

18. H. Ye and Y. Liu, "A new method for standing phase angle reduction in system restoration by incorporating load pickup as a control means," *International Journal of Electrical Power & Energy Systems*, vol. 53, pp. 664–674, 2013. (cited on pages 2, 36, 37, 40, 42, and 52)

19. A. Ketabi, A. Ranjbar, and R. Feuillet, "New approach to standing phase angle reduction for power system restoration," *European transactions on electrical power*, vol. 12, no. 4, pp. 301–307, 2002. (cited on pages 2, 36, 40, 42, and 52)

20. D. Hazarika and A. Sinha, "An algorithm for standing phase angle reduction for power system restoration," *Power Systems, IEEE Transactions on*, vol. 14, no. 4, pp. 1213–1218, 1999. (cited on pages 2, 36, 40, and 52)

21. N. Martins, E. De Oliveira, W. Moreira, J. L. R. Pereira, and R. Fontoura, "Redispatch to reduce rotor shaft impacts upon transmission loop closure," *IEEE Transactions on Power Systems*, vol. 23, no. 2, pp. 592–600, 2008. (cited on pages 2 and 52)

22. D. Gan, R. Thomas, and R. Zimmerman, "Stability-constrained optimal power flow," *IEEE Transactions on Power Systems*, vol. 15, no. 2, pp. 535–540, May 2000. (cited on pages 2, 24, 52, 55, and 56)

23. Y. Yuan, J. Kubokawa, and H. Sasaki, "A solution of optimal power flow with multicontingency transient stability constraints," *Power Systems, IEEE Transactions on*, vol. 18, no. 3, pp. 1094–1102, Aug 2003. (cited on pages 2, 24, and 52)

24. P. Van Hentenryck, C. Coffrin, and R. Bent, "Vehicle routing for the last mile of power system restoration," in *PSCC'11, Stockholm, Sweden*, 2011. (cited on pages 2, 3, 14, 35, 37, 40, and 42)

25. E. B. Fisher, R. P. O'Neill, and M. C. Ferris, "Optimal transmission switching," *IEEE Transactions on Power Systems*, vol. 23, no. 3, pp. 1346–1355, Aug 2008. (cited on pages 3, 14, 19, 49, and 50)

26. P. Wong and R. Larson, "Optimization of natural-gas pipeline systems via dynamic programming," *Automatic Control, IEEE Transactions on*, vol. 13, no. 5, pp. 475–481, 1968. (cited on pages 3, 31, and 80)

27. B. Rothfarb, H. Frank, D. M. Rosenbaum, K. Steiglitz, and D. J. Kleitman, "Optimal design of offshore natural-gas pipeline systems," *Operations research*, vol. 18, no. 6, pp. 992–1020, 1970. (cited on pages 3, 31, and 80)

28. C. A. Luongo, W. C. Yeung, and B. J. Gilmour, "Optimizing the operation of gas transmission networks," in *Computers in engineering*, 1991, vol. 24, pp. 663–666. (cited on page 3)

29. G. L. Peters, "Gas and electric infrastructure interdependency analysis," *Envision Energy Solutions*, vol. 22, 2012. (cited on pages 3 and 80)

30. ——, "Embedded natural gas-fired electric power generation infrastructure analysis: An analysis of daily pipeline capacity availability," EnVision Energy Solutions, Tech. Rep., 2012. (cited on pages 3 and 80)

31. T. W. K. Mak, C. Coffrin, P. Van Hentenryck, I. A. Hiskens, and D. Hill, "Power system restoration planning with standing phase angle and voltage difference constraints," in *Proceedings of the 18th Power Systems Computation Conference (PSCC'14)*, Wroclaw, Poland, 2014. (cited on page 4)

32. H. Hijazi, T. W. K. Mak, and P. Van Hentenryck, "Power system restoration with transient stability," in *AAAI'15*, 2015. (cited on pages 4 and 52)

33. T. W. K. Mak, P. Van Hentenryck, and I. A. Hiskens, "A nonlinear optimization model for transient stable line switching," in *IEEE American Control Conference*, Seattle, WA, 2017, pp. 2085–2092. (cited on page 4)

34. T. W. K. Mak, P. Van Hentenryck, A. Zlotnik, H. Hijazi, and R. Bent, "Efficient dynamic compressor optimization in natural gas transmission systems," in *IEEE American Control Conference*, Boston, MA, 2016, pp. 7484–7491. (cited on pages 4, 29, and 81)

35. T. W. K. Mak, P. Van Hentenryck, A. Zlotnik, and R. Bent, "Dynamic compressor optimization in natural gas pipeline systems," *INFORMS Journal on Computing*, p. in press, 2018. (cited on page 4)

36. C. Coffrin and P. Van Hentenryck, "A linear-programming approximation of AC power flows," *Informs Journal on Computing*, vol. 26, no. 4, pp. 718–734, 2014.   (cited on pages 13, 14, and 16)

37. C. Coffrin, H. Hijazi, and P. V. Hentenryck, "The qc relaxation: A theoretical and computational study on optimal power flow," *IEEE Transactions on Power Systems*, vol. 31, no. 4, pp. 3008–3018, July 2016. (cited on pages 13 and 16)

38. J. A. Momoh, R. Adapa, and M. E. El-Hawary, "A review of selected optimal power flow literature to 1993. i. nonlinear and quadratic programming approaches," *IEEE Transactions on Power Systems*, vol. 14, no. 1, pp. 96–104, Feb 1999. (cited on page 14)

39. J. A. Momoh, M. E. El-Hawary, and R. Adapa, "A review of selected optimal power flow literature to 1993. ii. newton, linear programming and interior point methods," *IEEE Transactions on Power Systems*, vol. 14, no. 1, pp. 105–111, Feb 1999. (cited on page 14)

40. H. W. Dommel and W. F. Tinney, "Optimal power flow solutions," *IEEE Transactions on Power Apparatus and Systems*, vol. PAS-87, no. 10, pp. 1866–1876, Oct 1968. (cited on page 14)

41. K. Lehmann, A. Grastien, and P. V. Hentenryck, "Ac-feasibility on tree networks is np-hard," *IEEE Transactions on Power Systems*, vol. 31, no. 1, pp. 798–801, Jan 2016. (cited on page 14)

42. T. J. Overbye, X. Cheng, and Y. Sun, "A comparison of the AC and DC power flow models for LMP calculations," in *Proceedings of the 37th Annual Hawaii International Conference on System Sciences*, 2004. (cited on pages 14 and 16)

43. D. Bienstock and S. Mattia, "Using mixed-integer programming to solve power grid blackout problems," *Discrete Optimization*, vol. 4, no. 1, pp. 115 – 141, 2007. (cited on page 14)

44. J. Salmeron, K. Wood, and R. Baldick, "Worst-case interdiction analysis of large-scale electric power grids," *IEEE Transactions on Power Systems*, vol. 24, no. 1, pp. 96–104, Feb 2009. (cited on page 14)

45. C. Coffrin, P. Van Hentenryck, and R. Bent, "Strategic stockpiling of power system supplies for disaster recovery." *Proceedings of the 2011 IEEE Power & Energy Society General Meetings (PES)*, 2011. (cited on pages 14 and 35)

46. B. Stott, J. Jardim, and O. Alsac, "DC power flow revisited," *IEEE Transactions on Power Systems*, vol. 24, no. 3, pp. 1290–1300, Aug 2009. (cited on pages 14 and 16)

47. U. G. Knight, *Power Systems Engineering and Mathematics*.   Pergamon Press Oxford, 1972. (cited on page 14)

48. A. J. Wood and B. F. Wollenberg, *Power generation, operation, and control*.   Wiley-Interscience, 1996. (cited on page 14)

49. L. Powell, *Power System Load Flow Analysis (Professional Engineering)*. McGraw-Hill Professional, 2004. (cited on page 14)

50. A. Gómez-Expósito, A. J. Conejo, and C. Cañizares, *Electric energy systems: analysis and operation*. CRC Press, 2008. (cited on page 14)

51. M. E. Baran and F. F. Wu, "Optimal capacitor placement on radial distribution systems," *IEEE Transactions on Power Delivery*, vol. 4, no. 1, pp. 725–734, Jan 1989. (cited on page 16)

52. K. Purchala, L. Meeus, D. V. Dommelen, and R. Belmans, "Usefulness of dc power flow for active power flow analysis," in *IEEE Power Engineering Society General Meeting, 2005*, June 2005, pp. 454–459 Vol. 1. (cited on page 16)

53. C. Coffrin, P. V. Hentenryck, and R. Bent, "Approximating line losses and apparent power in ac power flow linearizations," in *2012 IEEE Power and Energy Society General Meeting*, July 2012, pp. 1–8. (cited on page 16)

54. ——, "Accurate load and generation scheduling for linearized dc models with contingencies," in *2012 IEEE Power and Energy Society General Meeting*, July 2012, pp. 1–8. (cited on page 16)

55. R. Bent, C. Coffrin, R. R. E. Gumucio, and P. V. Hentenryck, "Transmission network expansion planning: Bridging the gap between ac heuristics and dc approximations," in *Power Systems Computation Conference (PSCC), 2014*, Aug 2014, pp. 1–8. (cited on page 16)

56. J. Lavaei and S. H. Low, "Zero duality gap in optimal power flow problem," *IEEE Transactions on Power Systems*, vol. 27, no. 1, pp. 92–107, Feb 2012. (cited on page 16)

57. D. S. Kirschen and T. L. Volkmann, "Guiding a power system restoration with an expert system," *Power Systems, IEEE Transactions on*, vol. 6, no. 2, pp. 558–566, 1991. (cited on pages 17 and 18)

58. L. A. Wolsey, *Integer Programming*. Wiley, 1998. (cited on page 19)

59. C. Coffrin, H. Hijazi, K. Lehmann, and P. Van Hentenryck, "Primal and dual bounds for optimal transmission switching," in *Proceedings of the 18th Power Systems Computation Conference (PSCC'14)*, 2014. (cited on pages 19, 20, 21, 49, and 50)

60. T. Potluri and K. W. Hedman, "Impacts of topology control on the ACOPF," in *2012 IEEE Power and Energy Society General Meeting*, July 2012, pp. 1–7. (cited on pages 19, 49, and 50)

61. W. Shao and V. Vittal, "Corrective switching algorithm for relieving overloads and voltage violations," *IEEE Transactions on Power Systems*, vol. 20, no. 4, pp. 1877–1885, Nov 2005. (cited on pages 19 and 49)

62. K. W. Hedman, R. P. O'Neill, E. B. Fisher, and S. S. Oren, "Optimal transmission switching - sensitivity analysis and extensions," *IEEE Transactions on Power Systems*, vol. 23, no. 3, pp. 1469–1479, Aug 2008.   (cited on pages 19 and 50)

63. J. D. Fuller, R. Ramasra, and A. Cha, "Fast heuristics for transmission-line switching," *IEEE Transactions on Power Systems*, vol. 27, no. 3, pp. 1377–1386, Aug 2012.   (cited on pages 19 and 50)

64. C. Barrows and S. Blumsack, "Transmission switching in the RTS-96 test system," *IEEE Transactions on Power Systems*, vol. 27, no. 2, pp. 1134–1135, May 2012.   (cited on pages 19 and 50)

65. C. Barrows, S. Blumsack, and R. Bent, "Computationally efficient optimal transmission switching: Solution space reduction," in *2012 IEEE Power and Energy Society General Meeting*, July 2012, pp. 1–8.   (cited on pages 19 and 50)

66. K. W. Hedman, S. S. Oren, and R. P. O'Neill, *Flexible Transmission in the Smart Grid: Optimal Transmission Switching*.   Berlin, Heidelberg: Springer Berlin Heidelberg, 2012, pp. 523–553.   (cited on pages 19 and 50)

67. A. Sorokin, S. Rebennack, P. M. Pardalos, N. A. Iliadis, and M. V. Pereira, *Handbook of Networks in Power Systems I*.   Springer Science & Business Media, 2012.   (cited on page 19)

68. M. Soroush and J. D. Fuller, "Accuracies of optimal transmission switching heuristics based on DCOPF and ACOPF," *IEEE Transactions on Power Systems*, vol. 29, no. 2, pp. 924–932, March 2014.   (cited on pages 19 and 50)

69. P. Sauer and M. Pai, *Power System Dynamics and Stability*.   Stipes Publishing L.L.C., 2006.   (cited on pages 23, 24, 52, 53, and 54)

70. K. W. Hedman, M. C. Ferris, R. P. O'Neill, E. B. Fisher, and S. S. Oren, "Co-optimization of generation unit commitment and transmission switching with n-1 reliability," *IEEE Transactions on Power Systems*, vol. 25, no. 2, pp. 1052–1063, May 2010.   (cited on page 24)

71. M. H. Haque and A. H. M. A. Rahim, "Determination of first swing stability limit of multimachine power systems through taylor series expansions," *IEE Proceedings C - Generation, Transmission and Distribution*, vol. 136, no. 6, pp. 373–380, Nov 1989.   (cited on page 24)

72. M. H. Haque, "Improvement of first swing stability limit by utilizing full benefit of shunt facts devices," *IEEE Transactions on Power Systems*, vol. 19, no. 4, pp. 1894–1902, Nov 2004.   (cited on page 24)

73. ——, "Evaluation of first swing stability of a large power system with various facts devices," *IEEE Transactions on Power Systems*, vol. 23, no. 3, pp. 1144–1151, Aug 2008.   (cited on page 24)

74. J. J. Ford, G. Ledwich, and Z. Y. Dong, "Efficient and robust model predictive control for first swing transient stability of power systems using flexible ac transmission systems devices," *IET Generation, Transmission Distribution*, vol. 2, no. 5, pp. 731–742, September 2008. (cited on page 24)

75. Q. Jiang, Y. Wang, and G. Geng, "A parallel reduced-space interior point method with orthogonal collocation for first-swing stability constrained emergency control," *IEEE Transactions on Power Systems*, vol. 29, no. 1, pp. 84–92, Jan 2014. (cited on page 24)

76. B. Sebastian and R. Garg, "Transient stability analysis of multi-machine power system and first swing stability analysis using svc," in *Advances in Electrical Engineering (ICAEE), 2014 International Conference on*, Jan 2014, pp. 1–4. (cited on page 24)

77. P. M. Anderson and A. A. Fouad, *Power system control and stability*. John Wiley & Sons, 2008. (cited on page 24)

78. M. Abbaspour and K. Chapman, "Nonisothermal transient flow in natural gas pipeline," *Journal of Applied Mechanics, Transactions of the ASME*, vol. 75, no. 3, May 2008. (cited on page 28)

79. A. Osiadacz, "Simulation of transient gas flows in networks," *International journal for numerical methods in fluids*, vol. 4, no. 1, pp. 13–24, 1984. (cited on pages 29 and 80)

80. M. Chertkov, S. Backhaus, and V. Lebedev, "Cascading of fluctuations in interdependent energy infrastructures: Gas-grid coupling," *Applied Energy*, vol. 160, pp. 541 – 551, 2015. (cited on pages 29 and 80)

81. A. Thorley and C. Tiley, "Unsteady and transient flow of compressible fluids in pipelinesâĂŤa review of theoretical and some experimental studies," *International Journal of Heat and Fluid Flow*, vol. 8, no. 1, pp. 3 – 15, 1987. (cited on page 29)

82. S. Misra, M. W. Fisher, S. Backhaus, R. Bent, M. Chertkov, and F. Pan, "Optimal compression in natural gas networks: A geometric programming approach," *IEEE Transactions on Control of Network Systems*, vol. 2, no. 1, pp. 47–56, 2015. (cited on pages 29, 31, and 80)

83. E. S. Menon, *Gas pipeline hydraulics*. CRC Press, 2005. (cited on page 30)

84. K. T. Midthun, M. Bjørndal, and A. Tomasgard, "Modeling optimal economic dispatch and system effects in natural gas networks," *The Energy Journal*, pp. 155–180, 2009. (cited on pages 31 and 80)

85. C. Borraz-Sánchez, "Optimization methods for pipeline transportation of natural gas," Ph.D. dissertation, Bergen Univ.(Norway), 2010. (cited on pages 31 and 80)

86. F. Babonneau, Y. Nesterov, and J.-P. Vial, "Design and operations of gas transmission networks," *Operations research*, vol. 60, no. 1, pp. 34–47, 2014. (cited on pages 31 and 80)

87. C. Borraz-Sánchez, R. Bent, S. Backhaus, H. Hijazi, and P. Van Hentenryck, "Convex relaxations for gas expansion planning," *INFORMS Journal on Computing*, vol. 28, no. 4, pp. 645–656, 2016. (cited on pages 31, 80, and 111)

88. C. Coffrin, P. Van Hentenryck, and R. Bent, "Accurate Load and Generation Scheduling for Linearized DC Models with Contingencies," *Proceedings of the 2012 IEEE Power & Energy Society General Meetings (PES)*, 2012. (cited on page 35)

89. C. Coffrin and P. Van Hentenryck, "Transmission system restoration: Co-optimization of repairs, load pickups, and generation dispatch," in *Submitted to PSCC'14, Wroclaw, Poland*, 2014. (cited on pages 35, 36, 40, and 42)

90. C. Coffrin and P. V. Hentenryck, "A linear-programming approximation of ac power flows," *Forthcoming in INFORMS Journal on Computing*, 2013. (cited on pages 36, 37, and 42)

91. R. P. Klump and J. D. Weber, "Real-time data retrieval and new visualization techniques for the energy industry," in *HICSS'02*, 2002, pp. 712–717. (cited on page 36)

92. R. Zimmerman, C. Murillo-Sánchez, and R. Thomas, "Matpower: Steady-state operations, planning, and analysis tools for power systems research and education," *IEEE Transactions on Power Systems*, vol. 26, no. 1, pp. 12 –19, feb. 2011. (cited on pages 36 and 43)

93. K.-H. Tseng, W.-S. Kao, and J.-R. Lin, "Load model effects on distance relay settings," *Power Delivery, IEEE Transactions on*, vol. 18, no. 4, pp. 1140–1146, 2003. (cited on page 37)

94. R. Bent and P. Van Hentenryck, "Randomized adaptive spatial decoupling for large-scale vehicle routing with time windows." in *AAAI'07*, 2007, pp. 173–178. (cited on page 43)

95. D. Pacino and P. Van Hentenryck, "Large neighborhood search and adaptive randomized decompositions for flexible job-shop scheduling," in *IJCAI'11*, 2011, pp. 1997–2002. (cited on page 43)

96. C. Coffrin, P. Van Hentenryck, and R. Bent, "Last-Mile restoration for multiple interdependent infrastructures," in *AAAI'12*, 2012, pp. 455–463. (cited on page 43)

97. C. Coffrin, D. Gordon, and P. Scott, "NESTA, the NICTA energy system test case archive," *CoRR*, vol. abs/1411.0359, 2014. [Online]. Available: http://arxiv.org/abs/1411.0359 (cited on pages 50, 51, and 64)

98. M. Gibbard and D. Vowles, "IEEE PES task force on benchmark systems for stability controls: Simplified 14-generator model of the south east australian power system MudPack-PSS/E report," IEEE PES Power System Dynamic Performance Committee, Tech. Rep., June 2014, accessed 10 Nov 2016: http://eioc.pnnl.gov/benchmark/ieeess/australian_test_system/Simplified_14-Gen_System_Rev4_20140614_IEEEVersion.pdf. (cited on pages 51 and 74)

99. R. Zimmerman, C. Murillo-Sánchez, and R. Thomas, "MATPOWER: Steady-state operations, planning, and analysis tools for power systems research and education," *IEEE Transactions on Power Systems*, vol. 26, no. 1, pp. 12 –19, feb. 2011. (cited on page 64)

100. R. Fourer, D. M. Gay, and B. W. Kernighan, *AMPL: A Modeling Language for Mathematical Programming*. Cengage Learning, 2002. (cited on pages 64 and 94)

101. P. Bonami, L. T. Biegler, A. R. Conn, G. Cornuéjols, I. E. Grossmann, C. D. Laird, J. Lee, A. Lodi, F. Margot, N. Sawaya, and A. Wächter, "An algorithmic framework for convex mixed integer nonlinear programs," *Discrete Optimization*, vol. 5, no. 2, pp. 186 – 204, 2008. (cited on page 64)

102. "A collection of Fortran codes for large scale scientific computation," http://www.hsl.rl.ac.uk/, 2016. (cited on page 64)

103. A. Wächter and L. T. Biegler, "On the implementation of an interior-point filter line-search algorithm for large-scale nonlinear programming," *Mathematical Programming*, vol. 106, no. 1, pp. 25–57, 2006. (cited on pages 64, 82, and 94)

104. S. M. Baek, J. W. Park, and I. A. Hiskens, "Optimal tuning for linear and nonlinear parameters of power system stabilizers in hybrid system modeling," *IEEE Transactions on Industry Applications*, vol. 45, no. 1, pp. 87–97, Jan 2009. (cited on page 65)

105. B. Gang, "Columbia Grid transient stability manual," Columbia Grid, Tech. Rep., April 2016, accessed 2 Aug 2016: https://www.columbiagrid.org/TransientStability-overview.cfm. (cited on page 70)

106. K. S. Shetye, "Validation of power system transient stability results," Master's thesis, University of Illinois at Urbana-Champaign, 2011. (cited on page 70)

107. M. Qadrdan, M. Chaudry, J. Wu, N. Jenkins, and J. Ekanayake, "Impact of a large penetration of wind generation on the gb gas network," *Energy Policy*, vol. 38, no. 10, pp. 5684–5695, 2010. (cited on page 79)

108. P. J. Hibbard and T. Schatzki, "The interdependence of electricity and natural gas: current factors and future prospects," *The Electricity Journal*, vol. 25, no. 4, pp. 6–17, 2012. (cited on page 79)

109. C. Lyons and G. Litra, "Gas-power interdependence: Knock-on effects of the dash to gas," 2013, http://www.scottmadden.com/insight/598/gaspower-interdependence.html. (cited on pages 79 and 80)

110. T. Li, M. Eremia, and M. Shahidehpour, "Interdependency of natural gas network and power system security," *Power Systems, IEEE Transactions on*, vol. 23, no. 4, pp. 1817–1824, 2008. (cited on page 80)

111. R. Schmalensee, "Growing concerns, possible solutions: The interdependency of natural gas and electricity systems," MIT Energy Initiative, Tech. Rep., April 2013, http://energy.mit.edu/publication/growing-concerns-possible-solutions/. (cited on page 80)

112. R. D. Tabors and S. Adamson, "Measurement of energy market inefficiencies in the co-ordination of natural gas &; power," in *47th Hawaii International Conference onSystem Sciences (HICSS)*.   IEEE, 2014, pp. 2335–2343. (cited on page 80)

113. R. Z. Ríos-Mercado and C. Borraz-Sánchez, "Optimization problems in natural gas trans-portation systems: A state-of-the-art review," *Applied Energy*, vol. 147, pp. 536–555, 2015. (cited on page 80)

114. T. Koch, B. Hiller, M. E. Pfetsch, and L. Schewe, *Evaluating gas network capacities*. SIAM, 2015. (cited on page 80)

115. R. Levitan, S. Wilmer, and R. Carlson, "Pipeline to reliability: Unraveling gas and elec-tric interdependencies across the eastern interconnection," *Power and Energy Magazine, IEEE*, vol. 12, no. 6, pp. 78–88, 2014. (cited on pages 80 and 111)

116. M. Chertkov, M. Fisher, S. Backhaus, R. Bent, and S. Misra, "Pressure fluctuations in natural gas networks caused by gas-electric coupling," in *2015 48th Hawaii International Conference on System Sciences (HICSS)*.   IEEE, 2015. (cited on page 80)

117. M. Shahidehpour and Z. Li, "White paper: Long-term electric and natural gas infrastruc-ture requirements," Illinois Institute of Technology, Tech. Rep., 2014.   (cited on page 80)

118. A. R. Thorley and C. H. Tiley, "Unsteady and transient flow of compressible fluids in pipelines - ĂŤa review of theoretical and some experimental studies," *International jour-nal of heat and fluid flow*, vol. 8, no. 1, pp. 3–15, 1987. (cited on pages 80 and 82)

119. A. D. Woldeyohannes and M. A. Majid, "Simulation model for natural gas transmission pipeline network system," *Simulation Modelling Practice and Theory*, vol. 19, no. 1, pp. 196–212, 2011. (cited on page 80)

120. D. Matko, G. Geiger, and W. Gregoritza, "Verification of various pipeline models," *Math-ematics and computers in simulation*, vol. 53, no. 4, pp. 303–308, 2000. (cited on page 80)

121. M. Herty, "Modeling, simulation and optimization of gas networks with compressors," *Networks and Heterogeneous Media*, vol. 2, no. 1, p. 81, 2007. (cited on page 80)

122. J. Zhou and M. Adewumi, "Simulation of transients in natural gas pipelines using hybrid tvd schemes," *International journal for numerical methods in fluids*, vol. 32, no. 4, pp. 407–437, 2000. (cited on page 80)

123. H. Rachford and R. Carter, "Optimizing pipeline control in transient gas flow," *Pipeline Simulation Interest Group*, 2000. (cited on pages 80 and 81)

124. K. Ehrhardt and M. Steinbach, *Nonlinear optimization in gas networks*.   Springer, 2005. (cited on pages 80 and 81)

125. M. Steinbach, "On PDE solution in transient optimization of gas networks," *Journal of computational and applied mathematics*, vol. 203, no. 2, pp. 345–361, 2007. (cited on pages 80 and 81)

126. M. Abbaspour, P. Krishnaswami, and K. Chapman, "Transient optimization in natural gas compressor stations for linepack operation," *Journal of Energy Resources Technology*, vol. 129, no. 4, p. 314, 2007. (cited on page 81)

127. P. Domschke, O. Kolb, and J. Lang, "Adjoint-based error control for the simulation and optimization of gas and water supply networks," *Applied Mathematics and Computation*, vol. 259, pp. 1003–1018, 2015. (cited on page 81)

128. S. Grundel, N. Hornung, B. Klaassen, P. Benner, and T. Clees, "Computing surrogates for gas network simulation using model order reduction," in *Surrogate-Based Modeling and Optimization*. Springer, 2013, pp. 189–212. (cited on pages 81 and 82)

129. Q. Gong, F. Fahroo, and I. M. Ross, "Spectral algorithm for pseudospectral methods in optimal control," *Journal of Guidance, Control, and Dynamics*, vol. 31, no. 3, pp. 460–471, 2008. (cited on page 82)

130. C. Canuto, M. Y. Hussaini, A. Quarteroni, and T. Zang, "Spectral methods," *Fundamentals in Single Domains, Springer*, 2006. (cited on pages 82 and 88)

131. Q. Gong, W. Kang, N. S. Bedrossian, F. Fahroo, P. Sekhavat, and K. Bollino, "Pseudospectral optimal control for military and industrial applications," in *Decision and Control, 2007 46th IEEE Conference on*. IEEE, 2007, pp. 4128–4142. (cited on page 82)

132. J. G. Verwer and J. M. Sanz-Serna, "Convergence of method of lines approximations to partial differential equations," *Computing*, vol. 33, no. 3-4, pp. 297–313, 1984. (cited on page 82)

133. S. Grundel, L. Jansen, N. Hornung, T. Clees, C. Tischendorf, and P. Benner, "Model order reduction of differential algebraic equations arising from the simulation of gas transport networks," in *Progress in Differential-Algebraic Equations*. Springer, 2014, pp. 183–205. (cited on pages 83 and 95)

134. A. Zlotnik, S. Dyachenko, S. Backhaus, and M. Chertkov, "Model reduction and optimization of natural gas pipeline dynamics," in *ASME Dynamic Systems and Control Conference*, Columbus, OH, 2015, p. V003T39A002. (cited on pages 83 and 95)

135. A. Zlotnik, A. M. Rudkevich, E. Goldis, P. A. Ruiz, M. Caramanis, R. Carter, S. Backhaus, R. Tabors, R. Hornby, and D. Baldwin, "Economic optimization of intra-day gas pipeline flow schedules using transient flow models," in *Proceedings of PSIG Meeting, Atlanta, GA*, 2017. (cited on page 84)

136. G. Elnagar, M. Kazemi, and M. Razzaghi, "The pseudospectral legendre method for discretizing optimal control problems," *Automatic Control, IEEE Transactions on*, vol. 40, no. 10, pp. 1793–1796, 1995. (cited on pages 88 and 99)

137. B. Fornberg, *A practical guide to pseudospectral methods*. Cambridge university press, 1998, vol. 1. (cited on page 88)

138. Q. Gong, F. Fahroo, and I. M. Ross, "Spectral algorithm for pseudospectral methods in optimal control," *Journal of Guidance, Control, and Dynamics*, vol. 31, no. 3, pp. 460–471, 2008. (cited on pages 88 and 99)

139. B. Zeng and L. Zhao, "Solving two-stage robust optimization problems using a column-and-constraint generation method," *Operations Research Letters*, vol. 41, no. 5, pp. 457 – 461, 2013. (cited on page 93)

140. A. N. Tikhonov, "On the solution of ill-posed problems and the method of regularization," *Dokl. Akad. Nauk SSSR*, vol. 151, no. 3, pp. 501–504, 1963. (cited on page 93)

141. "AMPL," AMPL Optimization: http://www.ampl.com, 2014. (cited on page 94)

142. M. Pfetsch, A. Fügenschuh, B. Geišler, N. Geišler, R. Gollmer, B. Hiller, J. Humpola, T. Koch, T. Lehmann, A. Martin, A. Morsi, J. Rövekamp, L. Schewe, M. Schmidt, R. Schultz, R. Schwarz, J. Schweiger, C. Stangl, M. Steinbach, S. Vigerske, and B. Willert, "Validation of nominations in gas network optimization: Models, methods, and solutions," *Optimization Methods and Software*, vol. 30, no. 1, pp. 15–53, 2015. (cited on page 99)

143. M. Chaudry, N. Jenkins, M. Qadrdan, and J. Wu, "Combined gas and electricity network expansion planning," *Applied Energy*, vol. 113, pp. 1171–1187, 2014. (cited on page 111)

144. S. L. Thumb, N. Brackett, A. Van Horn, and E. Remedios, "The regional gas infrastructure – is it ready for the power boom? how changes in gas and electric industries affect reliability and competitiveness of gas-fired generation," Electric Power Research Institute, Tech. Rep., 2001. (cited on page 111)